Hexagonal ice

Single crystalline hexagonal ice studied through surface-specific vibrational spectroscopy

María Alejandra Sánchez Zamora

Max-Planck Institut für Polymerforschung

Dissertation
zur Erlangung des Grades eines
"Doctor rerum naturalium (Dr. rer. nat.)"
der Fachbereiche:
08 - Physik, Mathematik und Informatik,
09 - Chemie, Pharmazie und Geowissenschaften,
10 - Biologie,
Universitätsmedizin
der Johannes Gutenberg-Universität

Max-Planck Graduate Center mit der Johannes Gutenberg-Universität Mainz

März 2017

Supervisor:
Co-Supervisor:

Committee Members:

Date of Examination: April 26, 2017 (14:30h)

D77-Dissertation of the Johannes Gutenberg University, Mainz

Statutory Declaration

I hereby declare that I wrote this dissertation submitted without any unauthorized external assistance and used only sources acknowledged in the work. All textual passages which are appropriated verbatim or paraphrased from published and unpublished texts as well as all information obtained from oral sources are duly indicated and listed in accordance with bibliographical rules. In carrying out this research, I complied with the rules of standard scientific practice as formulated in the statutes of the Johannes Gutenberg-University Mainz to insure standard scientific practice. I will write in the first person plural instead of singular (we instead of I) to make the text more readable.

María Alejandra Sánchez Zamora

Hombre

"Soy hombre, he nacido,
tengo piel y esperanza.
Yo exijo, por lo tanto,
que me dejen usarlas.
No soy dios: soy hombre
(como decir un alga).
Pero exijo calor en mis raíces,
almuerzo en mis entrañas.
No pido eternidades
llenas de estrellas blancas.
Pido ternura, cena,
silencio, pan, casa...

Soy hombre, es decir,
animal con palabas.
Y exijo, por lo tanto,
que me dejen usarlas."

(Jorge Debravo)

Abstract

In this thesis, we study the surface of water in its liquid and solid state. We investigate (i) an aqueous system where a model membrane interacts with amphiphilic dendrimers and (ii) single crystalline ice. We present a molecular scale description of both systems. To this end, we use sum frequency generation (SFG) spectroscopy, which provides unique information on the vibrational response of the outermost molecules of materials.

Amphiphilic polyphenylene dendrimers (PPDs) are macromolecules with well defined functional groups at the surface. They can be used as drug carriers in biological systems. We systematically study the interaction between PPDs with different surface termination and a model membrane. We find that PPDs having linear alkyl chains as functional groups are more favourable to bind with the model membranes. They also have better cellular uptake in comparison with branched alkyl groups and PPDs that have only hydrophilic functionalities.

PPDs with different hydrophilic groups (a carboxylic acid instead of a sulfonic acid) have similar surface activity at the model membrane-air interface, as well as similar cell penetrating properties. These findings indicate that the PPD-cell membrane interactions are dominated by the hydrophobic chains. Furthermore, we observe that larger PPDs disorganize the lipid monolayer, while smaller ones organizes it. Cell uptake results show that smaller PPDs have better cell penetration than larger ones, possibly because the larger PPDs disorganize the cell membrane.

We surmise that an ideal pyrene core dendrimer with good cell uptake results has amphiphilic functionalities, with hydrophilic and linear alkyl functional groups.

In the second part of the thesis, we study the quasi-liquid layer (QLL), which is present on ice even below the freezing point, as recognized by Faraday over 150 years ago. This layer is important for surface chemistry and glacier sliding close to subfreezing conditions.

We grow single crystalline ice samples from a crystalline seed that is pulled out slowly from a liquid water melt. Subsequently, they are characterized with cross polarisers, Formvar etching and X-ray diffraction.

Experimentally, by heating the ice sample starting at 235 K, a rather abrupt blue shift of the frequency of the OH stretch modes of hydrogen bonded interfacial water molecules is observed at 257 K. This points to an abrupt weakening of the hydrogen bonding structure at the interface. From a comparison of the experiments with simulations, we conclude that the QLL melts in a discrete manner, from one to two bilayers at 257 K. Furthermore, the SFG spectra indicate that at 269 K the QLL has more characteristics of ice than of liquid water.

Time resolved SFG experiments on single crystalline ice show that the vibrational relaxation dynamics of interfacial ice water molecules is faster than for the liquid water-air interface, similar to what has been reported in the literature for bulk ice and water. We find timescales of around 70 fs vs 200 fs, respectively.

Finally, a study of the proton transfer in ice is described. An experimental approach is suggested to produce single crystalline HCl-doped ice, and to obtain information of the proton transfer in and at the surface of ice with SFG and time domain terahertz spectroscopy.

Zusammenfassung

In dieser Dissertation untersuchen wir die Oberfläche von Wasser, sowohl als Flüssigkeit wie auch als Feststoff. Wir betrachten (1) ein wässriges System, in dem eine Modellmembran mit amphiphilen Dendrimeren interagiert und (2) monokristallines Eis. Für beide Systeme geben wir eine Beschreibung auf molekularer Ebene. Hierzu nutzen wir Summenfrequenzspektroskopie (SFG), welche einzigartige Informationen über die Schwingungseigenschaften der äußeren Moleküle eines Material liefert.

Amphiphile Polyphenylen Dendrimere (PPDs) sind Makromoleküle mit klar definierten funktionellen Gruppen an der Oberflächen, welche als Wirkstofftransporter in biologischen Systemen genutzt werden können. Wir untersuchen systematisch die Wechselwirkung zwischen PPDs mit verschiedenen Endgruppen an der Oberfläche und einer Modellmembran. Wir finden, das PPDs, welche eine lineare Alkylkette als funktionelle Gruppe besitzen, eine höhere Wahrscheinlichkeit haben, an die Modellmembran zu binden und zudem einen bessere zelluläre Aufnahmerate haben im Vergleich zu PPDs, die verzweigten Alkylgruppen oder lediglich hydrophilen Funktionalisierungen besitzen, haben.

PPDs mit verschiedenen hydrophilen Gruppen (etwa Carbonsäure anstelle von Sulfonsäure) besitzen eine ähnliche Oberflächenaktivität an der Grenzfläche zwischen Membran und Luft sowie ähnliche Eigenschaften zur Proteintransduktion in Zellen. Diese Ergebnisse deuten darauf hin, das die PPD-Zellmembran-Interaktion von den hydrophoben Seitenketten bestimmt wird. Zudem beobachten wir das größere PPDs eine Lipidmonoschicht durcheinander bringen, während kleinere sie strukturieren. Ergebnisse zur zellulären Aufnahme zeigen, das kleinere PPDs die Zellmembran besser penetrieren als größere, was möglicherweise auf die Desorganisation der Membran durch größere PPDs zurückzuführen ist. Wir zeigen, das ein idealer Dendrimer mit Pyrenkern für gute Zellaufnahmeeigenschaften amphiphil funktionalisiert ist und einen hydrophilen Anteils sowie eine lineare Alkylgruppe besitzt.

Im zweiten Teil dieser Dissertation untersuchen wir die quasi-flüssige Schicht (quasi-liquid layer, QLL), welche auf Eis selbst unterhalb des Gefrierpunktes vorhanden sind. Diese Schichten wurde bereits von Faraday vor über 150 Jahren beobachtet. Die Eis-Luft-Grenzfläche wird unter Bedingungen nahe am Gefrierpunkt untersucht, wie sie auch in der Oberflächenchemie oder beispielhaft beim Gleiten von Gletschern vorkommen.

Wir züchten monokristalline Eisproben ausgehend von einem Kristallisationskeim, der langsam aus einem Wasserbad gezogen wird. Anschließend wurden diese Proben mittels gekreuzten Polarisatoren, Formvar-Ätzung und Röntenbeugung charakterisiert. Im Experiment beobachten wir eine abrupte Blauverschiebung der Frequenz der OH Streckschwingungsmoden der über Wasserstoffbrücken verbundene Wassermoleküle nahe der Grenzfläche sobald die Probentemperatur den Schmelzpunkt des Bulk-Wassers erreicht. Dies deuted auf eine plötzliche Schwächung der Wasserstoffbrückenbindung an der Grenzfläche hin. Aus den experimentellen und theoretischen SFG-Spektren sowie Simulationen schlussfolgern wir, dass die QLL in diskreten Schritten von einer auf zwei Doppelschichten bei 257 K schmilzt. Des weiteren zeigen SFG-Spektren, dass bei 269 K die QLL eher die Eigenschaften von Eis als von flüssigem Wasser besitzt.

Zeitaufgelöste SFG-Experimente an monokristallinem Eis ergaben, dass die Schwinungsrelaxationsdynamik von Wassermolekülen an einer Eis-Wasser-Grenzfläche schneller als an der Grenzfläche von Wasser zu Luft abläuft. Wir finden einen Zeitraum von 70 fs bzw. 200 fs. Diese Beobachtung deckt sich mit ähnlichen, in der Literatur beschrieben, Ergebnissen für Bulk-Eis und Wasser.

Abschließend beschreibe ich eine Untersuchung des Protonentransfers in Eis. Ein experimenteller Ansatz wird erläutert, um monokristallines, HCl-dotiertes Eis herzustellen und damit Informationen über den Protonentransfer in Eis und an der Eisoberfläche mittels SFG und Terahertz-Time-Domain-Spektroskopie zu erhalten.

Contents

Chapter 1

Introduction

"Snow is falling, deeper – deeper./ Maybe, with that same stride/ in that same tempo, / with that same languor,/ Time's going by? "

Boris Leonidovich Pasternak, Snow Is Falling, 1917

Water covers two-thirds of our planet. However, some of its anomalous characteristics, such as its isobaric heat capacity and isothermal compressibility, are not fully understood, even when more and more sophisticated techniques to study these characteristics are invented constantly. Sometimes, it seems that new technology generates more questions than answers.

Water is one of the simplest molecules in chemistry, yet it is essential to life. Many biological processes take place in water. For example, the DNA's double helix is only distinguished in liquid water. Removing water from the structure results in induced changes in the DNA conformation [1]. Moreover, water allows various molecules to be accommodated at specific binding sites of the DNA [2].

Life on planet Earth depends on the abundance of water in its different phases - ice, liquid, and vapour. Nowadays, the oceans cover 70 % of the globe. Depending on the weather, about 50 % of the northern hemisphere is covered with permafrost, glaciers and ice sheets. Solid water exists in different environments, from glaciers to stratospheric clouds.

Ice plays a crucial role in a variety of phenomena in nature, in particular for geophysical processes such as glacial motion, chemical reactions, thunderstorms and soil metamorphosis [3, 4].

Glaciers and ice sheets record information about past climates, and seasonal snow-pack is closely related to the present weather. Glacial flow models are key for predicting the evolution of the sea level, planet albedo and the vast fresh water reservoirs on land [5]. It has been concluded from field observations that glacial ice flows easily at temperatures as low as -17 °C [6].

Past atmospheric records are found deep in Greenland and Antarctic ice. The atmospheric composition was stored in snow: snowflakes absorb impurities as they move down through the atmosphere, and they continue absorbing components close to the surface. Then, new snowfall compacts the old layers deep in the ground. The age of the ice core can be determined by the traces left by seasonal variations and events such as volcanic eruptions. Therefore, the date and the chemical components of the core reveal the composition of ancient atmospheres [5].

In the atmosphere, ice is involved in thundercloud charging, and acts as a catalytic substrate for chemical reactions [7–10]. For instance, it has been reported that ozone destruction starts with the chemical reaction of chlorine species -HCl, $ClONO_2$, and HOCl- on the surface of ice particles in the polar stratospheric clouds, whereby Cl_2 is produced. Subsequently, the formed chloride undergoes photolysis in the atmosphere, producing "active" chloride. Finally, the "active" species react with the ozone, resulting in ozone decomposition [5, 11].

1.1 Water

Figure 1.1 shows an isolated free water molecule. It consists of three atoms: one oxygen (in red) and two hydrogens (in white). Water can act as a hydrogen-bond donor (at the two hydrogen ends) or as a hydrogen bond acceptor (at the two lone pairs of the oxygen atom). It can form four hydrogen bonds with its neighbouring water molecules.

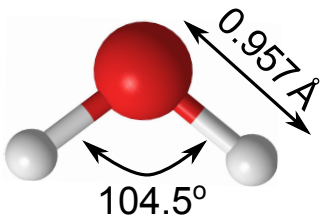

Figure 1.1: The geometry of a free H_2O molecule. The oxygen is partially negatively charged whereas the hydrogen has a partial positive charge.

Many of the anomalous properties of water (e.g. thermal expansion, heat capacity) have been associated to its extensive hydrogen-bonded network. Even when the bonds are constantly broken and reformed, on average the molecules are at least 3 fold coordinated at all times [12]. Furthermore, it has been reported that water consists of two classes of local water structures in a controversial article [13].

Water has an uneven distribution of partial charges which makes it a polar molecule, and because of its polarity it is an excellent solvent for charged or polar molecules such as dendrimers (see chapter 3). On the other hand, uncharged molecules do not dissolve well in water. This is an important property for biological systems, for instance for the shape of the complex cellular membrane, where a major component is phospholipid (an amphiphilic molecule) that generally has two hydrophobic fatty acid tails and a hydrophilic head. Figure 1.2 shows the phospholipid 1,2-dipalmitoyl-*sn*-glycero-3-phosphocholine (DPPC) that is used as model membrane in this thesis.

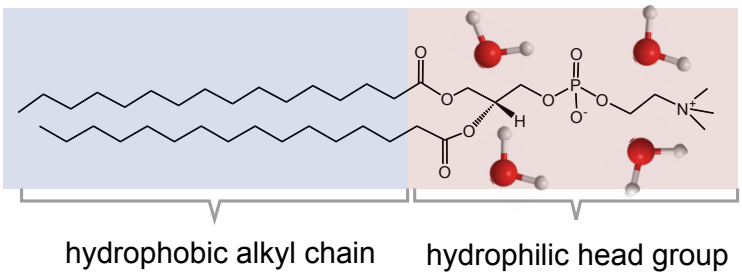

Figure 1.2: Molecular structure of the phospholipid DPPC, showing its amphiphilic nature. The water molecules are interacting only with the hydrophilic head group.

In this work, we investigate the properties of water by analysing its interaction with light. Water absorbs light at specific frequencies. It strongly interacts with ultraviolet light, where the electronic excitations occur. It does not absorb in the visible region, except for a very weak absorption at the red part of the spectrum which makes water look blue. In the mid-infrared region (200 to 4000 cm^{-1}) strong water-light interactions are present because of the vibrational resonances of water, for example OH-stretching and bending modes (Fig. 1.3). At longer wavelengths, the intermolecular

modes are observed, such as the librations (~ 180 cm^{-1}). At even longer wavelengths, the rotational motions (translations) are probed (centered at ~ 66 cm^{-1}) [14].

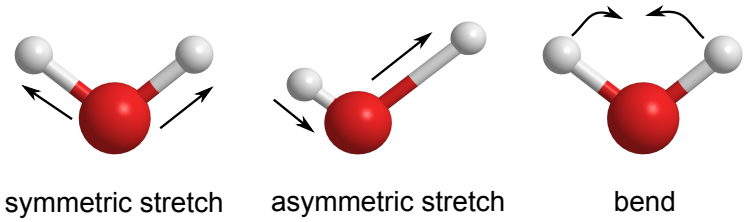

Figure 1.3: Three vibration modes of the molecule H_2O. The absorption of an IR photon may induce a stretch ($\sim$3200 cm^{-1}) or bend ($\sim$1600 cm^{-1}) vibration.

1.2 Ice

The most common type of ice on earth is hexagonal ice ($\boldsymbol{I_h}$). However, it is just one of 13 stable crystalline phases of ice [15]. Figure 1.4 shows the phase diagram of ice as a function of temperature and pressure. The various phases of ice are denoted with Roman numbers. As shown, most of the phases are produced by applying high pressures.

At atmospheric pressures, ice $\boldsymbol{I_h}$ is the dominant thermodynamically stable phase. Its name originates from the hexagonal packing of the water molecules. Cubic ice ($\boldsymbol{I_c}$) is a metastable phase of the hexagonal one, where the atoms are packed in a cubic crystal structure. It is formed at temperatures below 150 K. Upon heating, it has a phase transition to hexagonal ice [16].

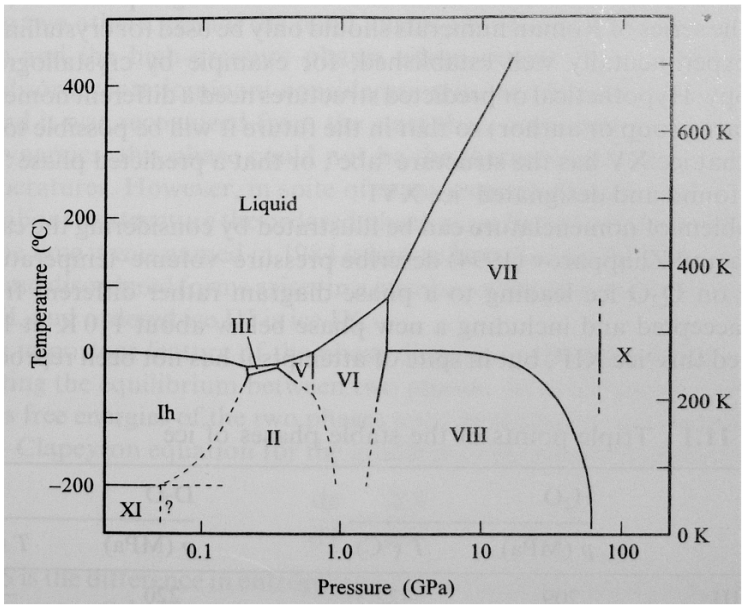

Figure 1.4: Phase diagram of the stable phases of the ice-water system on a logarithmic scale of pressure. The solid lines represent experimental measurements, and the broken lines illustrate extrapolated or inferred phase boundaries. From ref. [17].

This section will explain the generalities of ice I_h such as its crystal structure. Hexagonal ice I_h, is simply referred to as ice for the following chapters of this thesis.

1.2.1 Ice I_h crystal structure

The crystal structure is determined from X-ray diffraction patterns of the solid [18]. Figure 1.5 shows the structure of ice I_h, where the molecules are arranged in a hexagonal symmetry, similar to the wurzite crystalline structure. In the crystal, oxygen molecules are all centered close to a series of planes known as basal faces, those layers are stacked following a sequence of ABAB [19]. Another important characteristic of ice I_h is that it is an open structure. Because of this, frozen water has lower density compared to liquid water.

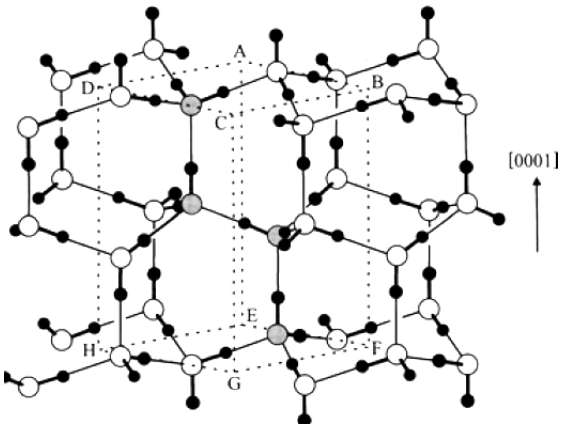

Figure 1.5: The crystal structure of hexagonal ice I_h, the white atoms are oxygen and the black ones are hydrogen. The dashed hexagonal prism with vertices ABCDEFGH is the unit cell and the four oxygen atoms contained in this cell are shown in grey [20].

In ice I_h two hydrogen atoms must be associated with one oxygen atom, but these atoms are positioned in a disorganized arrangement [17]. Bernal and Fowler proposed that in an ideal crystal the following ice rules should be fulfilled [18]:

1. There are two hydrogen atoms adjacent to each oxygen.
2. There are two hydrogen atoms bonded to each oxygen atom at close distance (covalently bonded) and two at larger distance (hydrogen bonded).
3. Only one hydrogen atom lies between each pair of oxygen atoms.

At low temperatures, the water molecules should "freeze" into one of six possible configurations, described in ref [17]. However, this does not happen even at 0 K. The residual entropy of ice I_h has been calculated to be 3.4091 $JK^{-1}mol^{-1}$ [21]. This ice phase is commonly known as proton disordered ice, where on average each hydrogen position is occupied by half a hydrogen atom [22,23]. Moreover, ice I_h has a phase transition around 72 K to **ice XI**, another ice phase also known as ice I_h ordered ice.

In addition to the intrinsic entropy of the ice I_h crystal, there are numerous point defects which allow isolated proton movement from one oxygen to another. As a consequence, there is no long range order in the orientation of the water molecules. These defects violate the third ice crystal rule and are called Bjerrum defects. These imperfections explain the unusual electrical properties

of ice, like large dielectric permittivity and conductivity, which originate from the migration of protons through the lattice [24].

A unit cell is market as ABCDEFGH in Fig 1.5. The space group of the average ice structure is $P6_3/mmc$. The P represents the primitive space lattice. The 6_3 indicates that the principal symmetry c-axis is a hexagonal screw axis (Fig. 1.6a). This means that when an oxygen atom in the crystal translates and rotates at the same time along the c-axis at such rate that when the atoms make a complete revolution when travelling along c, the oxygen atoms will coincide with the atomic position in the crystal after the molecules has travelled c/2 along the c-axis. The first m symbol indicates that there is a mirror plane normal to the c-axis. The remaining m and c stand for mirror and glide planes parallel to the c-axis, respectively (Fig. 1.6b and c). A glide plane means that if a mirror plane image of a specific oxygen atom is formed in the glide plane and then translated a distance of c/2 along the c-axis, this atom will coincide with another oxygen atom.

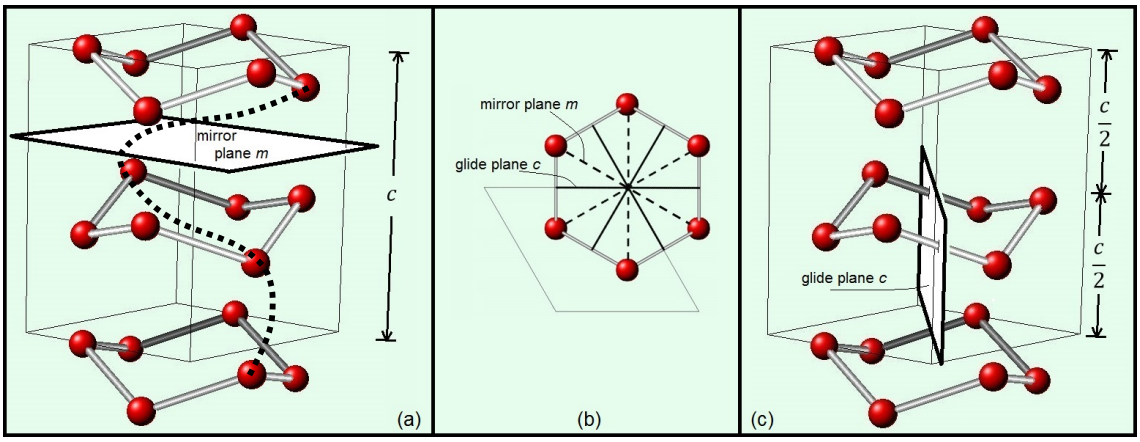

Figure 1.6: The symmetry elements of ice I_h : (a) the screw axis 6_3 and the plane m normal to the c-axis. (b) Mirror planes parallel to the c-axis. (c) Glide axis operation. Scheme modified from [25].

1.2.2 Ice I_h crystallographic faces

Figure 1.7a shows the hexagonal primitive cell (bold lines), described by the lattice parameters $a_1 = a_2 \neq c$ and by the corresponding angles $\alpha = \beta = 90°$ and $\gamma = 120°$. For ice, the lattice parameters at 253 K are a = 4.519 Å and c = 7.357 Å [17]. Three unit cells form the hexagonal prism (dashed lines in Fig. 1.7a), this structure is used to describe the different crystallographic faces.

Figure 1.7b shows the crystallographic hexagonal prism, where the oxygen atoms form a hexagonal plane containing three unit cells which is known as the basal face. The oxygen atoms are also making a smaller hexagon, see the dashed lines in figure 1.7b. This small hexagon is form from the projection of the oxygens in the upper part of the bilayer (the black dots) and lower part (red dots). In 3D space the basal face forms a chair-like structure (Fig. 1.6).

The hexagonal crystal planes and directions are designated by the Miller-Bravais four index. Figure 1.8a shows the hexagonal prism and the four coordinate hexagonal system: 1, 2, 3, 4. The indices of the basal (in red), primary prism (in grey) and secondary prism (in blue) planes can be determined as follows: the secondary prism plane (blue line in Fig. 1.8b) cuts in axes 1, 2, 3 and 4 at positions 1, 1, -1/2 and infinity, respectively. By taking the reciprocals of these numbers (reciprocal space), we obtain the plane $(11\bar{2}0)$, which is one of the six planes that describe the

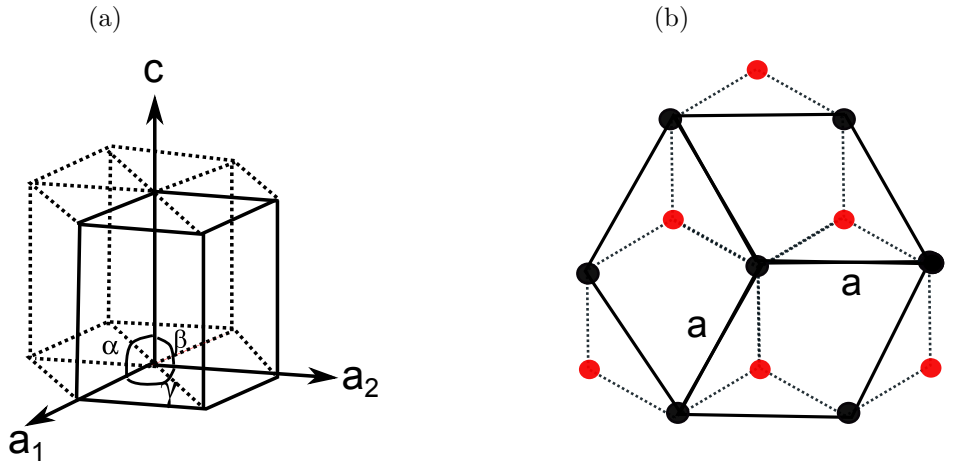

Figure 1.7: (a) Hexagonal unit cell (bold lines) and hexagonal prism (dashed lines) (b) Three unit cells that form a hexagonal prism (solid lines), small hexagons are formed by a projection of the oxygen atoms of the upper part (black circles) and the lower part (red circles) of the bilayer (dashed lines).

secondary prism planes, $\{11\bar{2}0\}$. [1] With a similar procedure, the primary prism plane (grey in Fig. 1.8c) intersect the axes 1, 2, 3 and 4 at 2, infinity, -2 and infinity, respectively. This corresponds to the $(10\bar{1}0)$ plane. Finally, the basal plane (Fig. 1.8d.) is $\{0001\}$, cutting the axis 1,2,3 and 4 at infinity, infinity, infinity and 1, respectively.

Figure 1.9 shows the arrangement of the water molecules in a perfect hexagonal ice crystalline structure. If one observes each main crystalline plane, one can conclude that water molecules in a basal $\{0001\}$ and in primary prism planes $\{01\bar{1}0\}$ have a bilayer structure, whereas the secondary prism face $\{\bar{2}110\}$ has a single layer structure [26]. These facts are very important for explaining the surface melting of each plane, explained further chapter 5.

1.2.3 Ice I_h and its interaction with light

Similar to liquid water, ice I_h also interacts with light, see section 1.1. Ice is transparent from the visible until near infrared, but the absorption rises at 8000 cm^{-1}, and becomes really strong from 4000 cm^{-1} to lower wavenumbers. Ice, when interacting with infrared light, has absorptions around 3200 cm^{-1} due to the OH stretch vibration, the asymmetric OH vibration and the bending overtone (Fig. 1.3). Figure 1.10 shows an IR absorption spectra of ice and of liquid water in the OH stretch mode region. The ice peak is shifted to lower frequencies and it is narrower than that of water because it is a solid with a specific crystalline structure, which exhibits less heterogeneity and stronger hydrogen bonds than liquid water. The bending OH mode (not shown here) is present at 1600 cm^{-1}. A complex band is observed from 550 to 1000 cm^{-1}, which has been assigned to the libration band. At frequencies lower than 403 cm^{-1} the translational modes are observed, where the phonons (lattice vibrations, characteristic of crystalline solids) are present [19, 27].

In this thesis, we focus on the spectral region from 2900 to 3700 cm^{-1} at the interface. Figure 1.11 shows the different environments of the water molecules in a perfect completely frozen primary prism of ice. The molecules with the chemical environment of (6), (5) and (4) represent the four coordinated molecules, that are located in the lower part of the bilayer. At the interface, the

[1] Planes that are equivalent by symmetry can be described by curly brackets {}. Indices in squares bracket [*hkil*] describe the direction in the crystals that is perpendicular to the plane (*hkil*) [19].

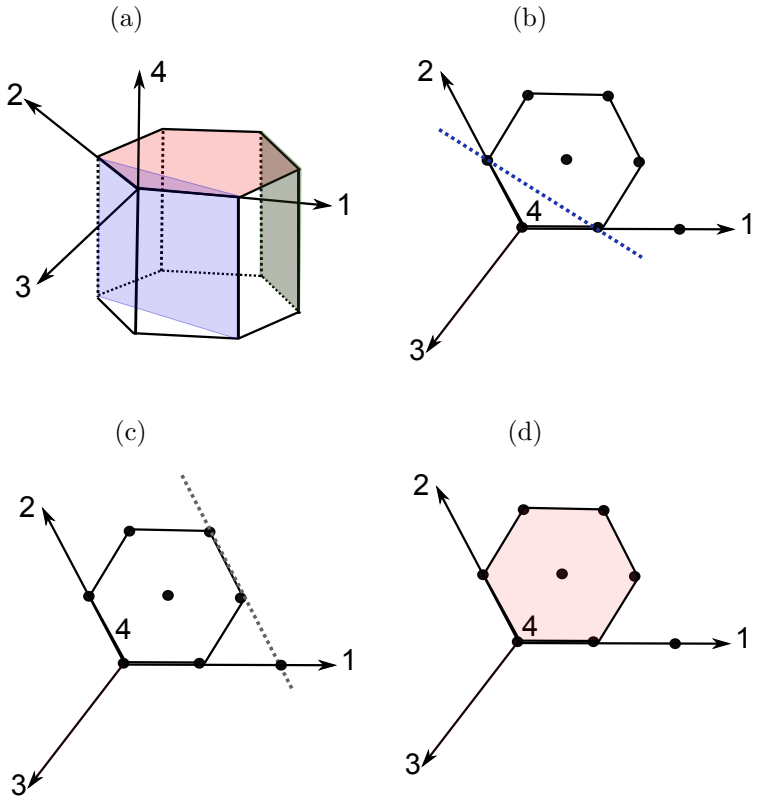

Figure 1.8: (a) Miller-Bravais crystallographic direction with the main crystallographic planes highlighted: (b) secondary prism plane (in blue), (c) primary prism plane (in grey) and (d) the basal plane (in red). The black dots are oxygen molecules in the upper bilayer that form a hexagonal prism (Fig. 1.7).

following ice molecules are observed: the three coordinated donor, donor, acceptor (DDA or d-O, (2)); donor, acceptor, acceptor (acceptor DAA or free OH, (1)); the companion of free OH (donor DAA, (3)) [30–32].

The symmetric and anti-symmetric OH stretch mode (Fig. 1.3) of the fourfold coordinated water molecules are centered at 3100 cm^{-1} and 3500 cm^{-1}, respectively [33]. The peak at 3100 cm^{-1} is generated by intermolecular coupling over several OH stretch chromophores, it has the strongest absorption. The anti-symmetric mode of the three coordinated ddA water molecules vibrates at 3580-3600 cm^{-1}. And finally, the free OH (4) similar to the free OH vibration of liquid water vibrates at 3700 cm^{-1}, and the companion of the free OH (donor dAA, 3) is at 3300 cm^{-1} [33]. Chapter 5 further explains these vibrations.

Over 150 years ago, Faraday recognized that a quasi liquid layer (QLL) is present on ice even below its freezing point. However, the nature of the water contained in the liquid layer and its thickness have remained the subject of intense debate. Most experimental work shows that with increasing temperature the QLL thickness increases continuously [5,34]. In contrast, early simulations reported that the QLL is formed in a bilayer by bilayer manner [35].

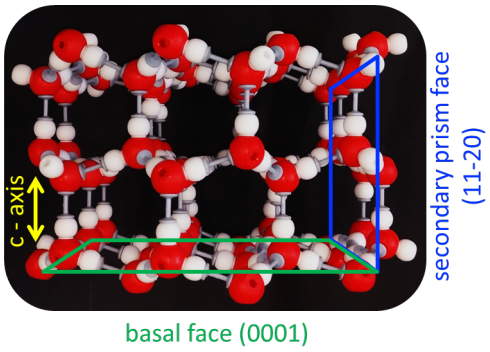

Figure 1.9: Molecular model of water atoms of a perfect ice I_h crystal, the picture was made by Hailong Li and Markus Mezger.

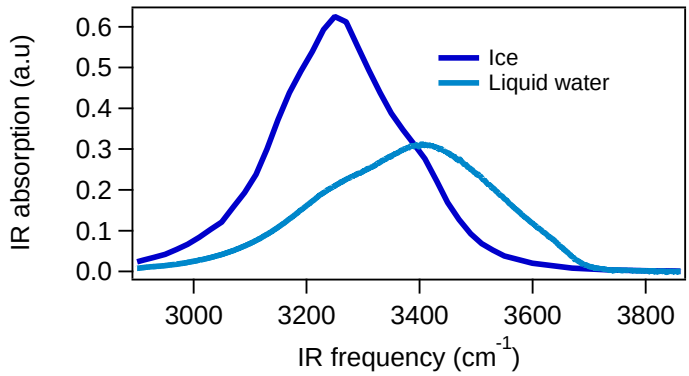

Figure 1.10: Infrared absorption spectrum of ice (in dark blue) [28], and of liquid water (in light blue) [29].

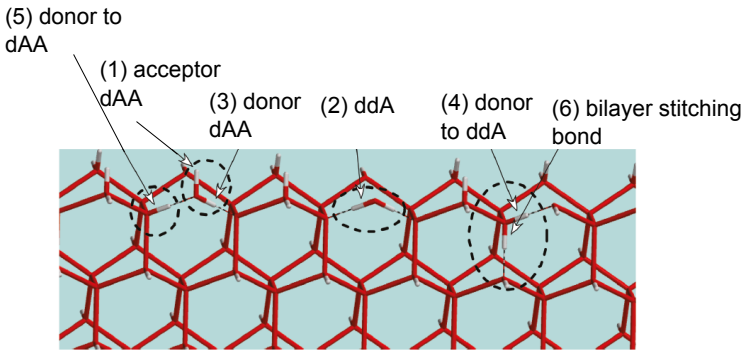

Figure 1.11: Schematic of the hydrogen bond configuration on the surface of the ice I_h crystal. In the top half bilayer: (1) free OH or acceptor dAA; (2) ddA or d-O; (3) H-bonded companion to the free OH or the donor bond of a dAA; (4) OH of water molecule hydrogen bonded to a ddA, (5) OH of the water molecule bonded to a ddA, (6) bilayer stitching OH bonds hydrogen bonded to the next bilayer [32].

In this thesis, we provide evidence of layer by layer growth at the ice air interface by combining experiments with simulations.

1.3 Outline

This thesis mainly focuses on water ice, but also studies the interaction of nanometric dendrimers with a model membrane. In both cases, light is used to study the interfacial region.

In chapter 2, the general theory underlying Sum frequency generation is explained. It also describes the optical set up that is used in this thesis.

In chapter 3 the dendrimer-lipid monolayer interactions are studied. We observed that the hydrophobic dendrimer terminal groups play an important role on the dendrimer-lipid interactions. The results are compared with cell studies performed by colleagues.

Chapter 4 deals with single crystal ice sample preparation, and the different ways to characterize the crystallinity of it. Herein, a highly reproducible method for producing large ice single crystals is developed. The surface melting of different crystallographic planes is explained in chapter 5. The observed surface transition is well reproduced by theoretical calculations. The first experimental studies of the surface dynamics of the ice-QLL-water interface are summarized in chapter 6.

Finally, chapter 7 is an outlook of proton disorder studies on water ice with induced point defects.

Chapter 2

Sum frequency generation

Sum frequency generation vibrational spectroscopy (SFG-VS) can provide information on the molecular composition, interactions, and orientation of molecules at surfaces and interfaces [36]. Sum frequency generation (SFG) is a coherent, second-order nonlinear process in which a visible (VIS) photon (ω_1) and infrared (IR) photon (ω_2) combine into one new photon (ω) at the sum frequency of the two incident photons ($\omega = \omega_1 + \omega_2$). SFG can probe electronic and vibrational modes by tuning the VIS and IR, respectively.

SFG-VIS has the incoming IR photon in resonance with a vibration at the sample surface, while the VIS photon up-converts the resonant signal to a higher energy. Figure 2.1 shows the energy diagrams of IR absorption and SFG-VS. For SFG-VIS to occur, a mode has to be both infrared and Raman active. A mode is infrared active when it has a vibration that has a frequency in the infrared region and has a change in the dipole. For this mode to couple with the light field, the field has to be able to induce a change in the molecular dipole moment. Raman active means that the vibration induce a change in the polarizability of the molecules when exposed to light.

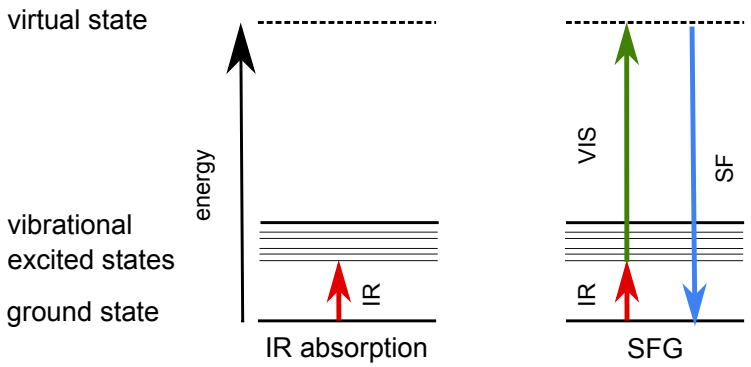

Figure 2.1: Energy diagrams showing transitions involved during infrared absorption (left) and vibrational sum frequency generation (right).

SFG is forbidden in centrosymmetric media, this implies that the SFG signal is only present where the symmetry is broken, for instance at interfaces. For this reason, the SFG signal of an interface between two isotropic media originates mainly from the interfacial dipolar contributions. This characteristic makes SFG a unique spectroscopic tool for molecular surface specific studies.

This chapter describes basic SFG theory, illustrates the optical setup used for static SFG, and shows an example of a SFG study of a polymer-silica interface.

2.1 Theory

This section is based on tutorial reviews by Lambert [37] and Wang [36]. The effects of optical magnetic fields and of multipoles (e.g. quadrupoles, see 2.1.2) and the induced dipoles for neighbouring dipolar fields are neglected. Thus, this section uses the dipole approximation for explaining SFG. Moreover, the tensor notation of the susceptibility (χ) is presented in a reduced description, for the sake of simplicity. For an advanced interpretation, refer to the textbooks by Shen [38] and Boyd [39].

When light interacts with molecules through the oscillation of an electric field $\mathbf{E}$ [1], the molecule's electron cloud will follow this oscillation, inducing an electric polarization $\boldsymbol{\mu}$ proportional to the electric field.

$$\boldsymbol{\mu} = \alpha \mathbf{E} \tag{2.1}$$

where α is the polarizability of the molecular electrons. For a large number of molecules in the condensed phase, the sum of the molecular electric multipoles give rise to a dipole moment per unit volume, the bulk polarization $\mathbf{P}$.

$$\mathbf{P} = \epsilon_o \chi^{(1)} \mathbf{E} \tag{2.2}$$

where $\chi^{(1)}$ is the macroscopic average of the polarizability known as first order (or linear) susceptibility, and ϵ_o is the permittivity of free space. Pulsed lasers can generate an electromagnetic field comparable with the intrinsic field experienced by the electrons in a molecule. As the optical $\mathbf{E}$ field is increased relative to the intrinsic field, the polarization becomes:

$$\mathbf{P} = \epsilon_o(\chi^{(1)}\mathbf{E} + \chi^{(2)}\mathbf{E}^2 + \chi^{(3)}\mathbf{E}^3 + ...) \tag{2.3}$$

where $\chi^{(2)}$ and $\chi^{(3)}$ are the second and third-order non-linear susceptibilities, respectively. These terms are significantly smaller than the linear one, $\chi^{(1)}$.

SFG is a two-photon process originating from the second-order non linear susceptibility $\chi^{(2)}$. It is possible to demonstrate the origin of SFG by using the time dependence of an incident electromagnetic field:

$$\mathbf{E(t)} = \mathbf{E}_1 \cos \omega t \tag{2.4}$$

where ω is the frequency of the incident light. Considering the induced polarization due to second-order effects $\mathbf{P}^{(2)}$, we obtain

$$\mathbf{P}^{(2)} = \epsilon_o \chi^{(2)} (\mathbf{E}_1 \cos \omega t)^2 = \frac{\epsilon_o \chi^{(2)}}{2} \mathbf{E}_1^2 (1 + \cos 2\omega t) \tag{2.5}$$

This equation demonstrates that the induced polarization contains terms that oscillates at twice the frequency (2ω) of the incident electric field $\mathbf{E}$.

If we have two incoming fields, i.e. from two different laser beams, $\mathbf{E}$ can expressed as the sum of the two oscillating incident fields,

$$\mathbf{E} = \mathbf{E}_1 \cos \omega_1 t + \mathbf{E}_2 \cos \omega_2 t \tag{2.6}$$

[1] Bold type indicates a vector quantity.

By substituting 2.6 in the second-order term of the polarization, we obtain the equation with all the contributions of the second-order non-linear susceptibility $\chi^{(2)}$ to the polarization:

$$\begin{aligned}\mathbf{P}^{(2)} &= \epsilon_o \chi^{(2)} [\mathbf{E}_1 \cos\omega_1 t + \mathbf{E}_2 \cos\omega_2 t]^2 \\ &= \frac{1}{2}\epsilon_o \chi^{(2)} [\mathbf{E}_1^2 + \mathbf{E}_2^2 + \mathbf{E}_1^2 \cos 2\omega_1 t \\ &+ \mathbf{E}_2^2 \cos 2\omega_2 t + 2\mathbf{E}_1\mathbf{E}_2 \cos(\omega_1 + \omega_2)t \\ &+ 2\mathbf{E}_1\mathbf{E}_2 \cos(\omega_1 - \omega_2)t]\end{aligned} \tag{2.7}$$

The expression contains two DC fields, two harmonics of the original frequencies (2ω, corresponding to second harmonic generation), the sum frequency ($\omega_1 + \omega_2$, SFG) and the difference-frequency ($\omega_1 - \omega_2$, DFG). For us, $\mathbf{E}_1$ and $\mathbf{E}_2$ correspond to a visible and IR pulsed laser source, $\mathbf{E}_{\mathrm{VIS}}$ and $\mathbf{E}_{\mathrm{IR}}$.

Looking just at the SFG term from (2.7), the simplest description of the SFG is:

$$\begin{aligned}\mathbf{P}^{(2)}_{\mathrm{SF}} &= \epsilon_o \chi^{(2)} \mathbf{E_1} \mathbf{E_2} \cos(\boldsymbol{\omega_1} + \boldsymbol{\omega_2})\mathbf{t} \\ &= \epsilon_o \chi^{(2)} \mathbf{E}_{\mathrm{VIS}} \mathbf{E}_{\mathrm{IR}} \cos(\omega_{\mathrm{VIS}} + \omega_{\mathrm{IR}})\mathbf{t}\end{aligned} \tag{2.8}$$

where $\chi^{(2)}$ is, in the Cartesian coordinates, a third-rank tensor with 27 elements that describes the interaction between two electric field vectors $\mathbf{E}_1$ and $\mathbf{E}_2$ and the generated vector $\mathbf{P}^{(2)}$. The mathematical expression that includes all possible vector components is defined as:

$$\mathbf{P}^{(2)} = \sum_i^{x,y,z} \mathbf{P}^{(2)}_{i,\mathrm{SFG}} = \epsilon_o \sum_i^{x,y,z} \sum_j^{x,y,z} \sum_k^{x,y,z} \chi^{(2)}_{ijk} \mathbf{E}_{\mathrm{j,VIS}} \mathbf{E}_{k,\mathrm{IR}} \tag{2.9}$$

Although $\chi^{(2)}_{ijk}$ has 27 components, the number of unique contributions is less due to symmetry constraints. In an isotropic medium with C_∞ symmetry, only seven elements are non-zero due to symmetry considerations at the interface and only four independent non zero $\chi^{(2)}_{ijk}$ components exist. The SFG signal can potentially generated from: $\chi^{(2)}_{zzz}, \chi^{(2)}_{xxz} \equiv \chi^{(2)}_{yyz}, \chi^{(2)}_{xzx} \equiv \chi^{(2)}_{yzy}, \chi^{(2)}_{zxx} \equiv \chi^{(2)}_{zyy}$.

In order to generate sum frequency, the IR and VIS beams must be temporally and spatially overlapped on the surface/interface. Figure 2.2 illustrates a SFG signal generated from a VIS and IR beam in reflection geometry. This coherent signal is generated at an angle θ_{SFG}, which can be calculated from the conservation of momentum of the three beams, known as the phase-matching condition:

$$n_{\mathrm{SF}} k_{\mathrm{SF}} \sin\theta_{\mathrm{SF}} = n_{\mathrm{VIS}} k_{\mathrm{VIS}} \sin\theta_{\mathrm{VIS}} + n_{\mathrm{IR}} k_{\mathrm{IR}} \sin\theta_{\mathrm{IR}} \tag{2.10}$$

where n is the refractive index of the propagation medium, k is ω/c, where c is the speed of light, and θ is the angle to the surface normal of each beam (Fig. 2.2).

The fields $\mathbf{E}_{\mathrm{VIS}}$ and $\mathbf{E}_{\mathrm{IR}}$ in equation (2.9) are the local fields at the interface and depend on the incident and the reflected field.

The incident fields can be characterized by two distinct directions of the electric field relative to the plane of incidence, referred to as polarizations. A component parallel to the plane of incident (p-polarized) and another perpendicular (s-polarized). Figure 2.3 shows the p- and s-polarized light. The p-polarized electric field has components along both X and Z axes, whereas the s-polarized light is described only along the Y axis.

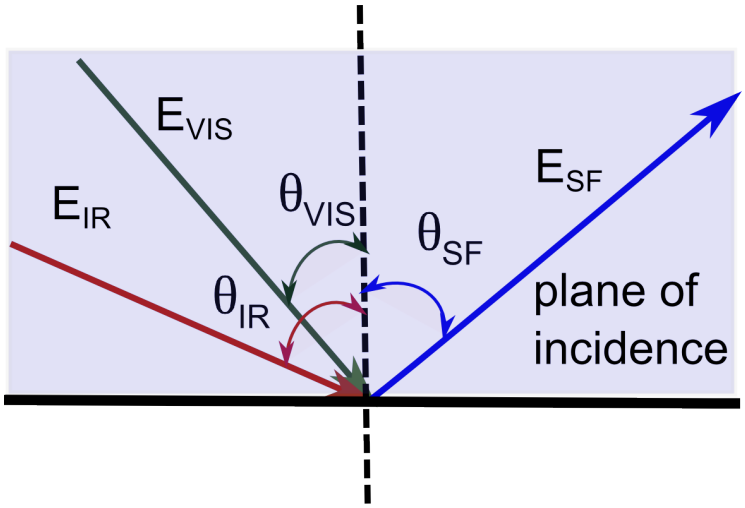

Figure 2.2: SFG reflected signal at the interface.

The electric field can be calculated trigonometrically (Fig. 2.3) in the Cartesian coordinate system. It is defined as:

$$\begin{aligned} \mathbf{E_x^I} &= -E_p^I \cos\theta_I \hat{\mathbf{x}} \\ \mathbf{E_y^I} &= E_s^I \hat{\mathbf{y}} \\ \mathbf{E_z^I} &= E_p^I \sin\theta_I \hat{\mathbf{z}} \end{aligned} \tag{2.11}$$

When light travels from a medium into a second one, both reflection and refraction may occur. The Fresnel amplitude coefficients for reflection and transmission describe the fraction of the light that is reflected or transmitted. These coefficients explain how the electromagnetic field of the light propagates from one uniform medium into another. These coefficients are given by:

$$\begin{aligned} r_p \equiv \frac{E_p^R}{E_p^I} &= \frac{n_T \cos\theta_I - n_I \cos\theta_T}{n_I \cos\theta_T + n_T \cos\theta_I} \\ r_s \equiv \frac{E_s^R}{E_s^I} &= \frac{n_I \cos\theta_I - n_T \cos\theta_T}{n_I \cos\theta_I + n_T \cos\theta_T} \end{aligned} \tag{2.12}$$

where θ_I and θ_T are the incident and the transmission angles relative to the surface normal, and n_I and n_T are the refractive indices of the two media.

The magnitudes of the local electric fields are the sum of the fields of the incident and reflected beams,

$$\begin{aligned} E_x &= E_x^I + E_x^R = -E_p^I \cos\theta_I (1 - r_p) \equiv -K_x E_p^I \\ E_y &= E_y^I + E_y^R = E_s^I (1 + r_s) \equiv K_y E_s^I \\ E_z &= E_z^I + E_z^R = E_p^I \sin\theta_I (1 + r_p) \equiv K_z E_p^I \end{aligned} \tag{2.13}$$

where K is the non-linear SF Fresnel factor.

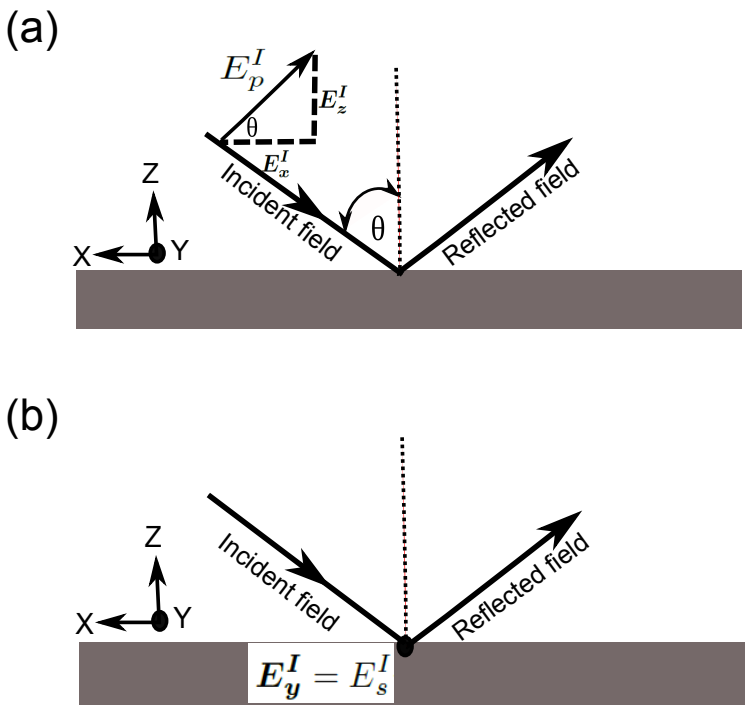

Figure 2.3: (a) p- and (b) s-polarized light at the interface.

The SFG expression, similar to equation (2.9) but omitting the summation operations, can be expressed in terms of the magnitudes of the incident beams:

$$\mathbf{P}^{(2)}_{i,\mathrm{SF}} = \epsilon_0 \chi^{(2)}_{ijk} \hat{\mathbf{j}} K_j E^I_{p/s,\mathrm{VIS}} \hat{\mathbf{k}} K_k E^I_{p/s,\mathrm{IR}} \tag{2.14}$$

Now that we know the SFG polarization generated at the interface, we can describe how this polarization give rise to the emission of radiation at this frequency. The SFG electric field and the radiation are related by the SFG nonlinear Fresnel coefficients, L factors:

$$\mathbf{E}_{\mathbf{i},\mathrm{SF}} = \mathrm{L}_{\mathbf{i}} \mathbf{P}^{(\mathbf{2})}_{\mathrm{i,SF}} \tag{2.15}$$

For the reflection geometry, the L-factors are given by:

$$\begin{aligned} L^R_x &= -\frac{i\omega_{\mathrm{SF}}}{c\epsilon_0} \frac{\cos\theta^T_{\mathrm{SF}}}{n_T \cos\theta^I_{\mathrm{SF}} + n_I \cos\theta^T_{\mathrm{SF}}} \\ L^R_y &= \frac{i\omega_{\mathrm{SF}}}{c\epsilon_0} \frac{1}{n_T \cos\theta^I_{\mathrm{SF}} + n_I \cos\theta^T_{\mathrm{SF}}} \\ L^R_z &= \frac{i\omega_{\mathrm{SF}}}{c\epsilon_0} \frac{(n_T/n_{\mathrm{layer}})^2 \sin\theta^T_{\mathrm{SF}}}{n_T \cos\theta^I_{\mathrm{SF}} + n_I \cos\theta^T_{\mathrm{SF}}} \end{aligned} \tag{2.16}$$

the angles θ^I_{SF} and θ^T_{SF} are the angles of the emitted SFG field in the incident and the transmittance medium, while n_I and n_T are the refractive indices in these media. n_{layer} is the refractive index at the interface, which is difficult to define.

We can now fully describe the SFG signal generated at the interface by combining equations (2.14) and (2.16). The intensity of the p and s polarized SF light detected from the surface is proportional to the sum of the square of the magnitudes of the component of the SF electric field, see equation (2.17):

$$\begin{aligned}
I_{p,SF} \propto & |\mathbf{E}_{x,\mathrm{SF}}|^2 + |\mathbf{E}_{z,\mathrm{SF}}|^2 \\
\propto & |L_x \mathbf{P}^{(2)}_{x,\mathrm{SF}}|^2 + |L_y \boldsymbol{P}^{(2)}_{z,\mathrm{SF}}|^2 \\
\propto & |\epsilon_0 L_x \sum_j^{x,y,z} \sum_k^{x,y,z} \chi^{(2)}_{xjk} K_j E^I_{p,\mathrm{VIS}} K_k E^I_{p,\mathrm{IR}}|^2 \\
& + |\epsilon_0 L_z \sum_j^{x,y,z} \sum_k^{x,y,z} \chi^{(2)}_{zjk} K_j E^I_{p,\mathrm{VIS}} K_k E^I_{p,\mathrm{IR}}|^2 \\
I_{s,SF} \propto & |\mathbf{E}_{y,\mathrm{SF}}|^2 \\
\propto & |L_y \mathbf{P}^{(2)}_{y,\mathrm{SF}}|^2 \\
\propto & |\epsilon_0 L_y \sum_j^{x,y,z} \sum_k^{x,y,z} \chi^{(2)}_{yjk} K_j E^I_{s,\mathrm{VIS}} K_k E^I_{s,\mathrm{IR}}|^2
\end{aligned} \tag{2.17}$$

2.1.1 SFG spectrum: Lorentzian model

In this thesis SFG is used to obtain molecular information at interfaces. To identify the vibrational modes and even quantify them, the data is fitted with a model that describes the response of the materials at the interface. The second order susceptibility $\chi^{(2)}$ is strongly frequency dependent, and therefore defines the shape of the SFG spectrum. When the IR pulse is resonant with a vibration, $\chi^{(2)}_{\mathrm{R}}$ increases and produces a change in the SFG signal that is used to identify the chemical structure of the sample. Vibrations are generally approximated by a complex Lorentzian, which for a resonant vibration is given by:

$$\chi^{(2)}_{\mathrm{R}} \approx \sum_n \frac{A_n}{\omega_{\mathrm{IR}} - \omega_n + i\Gamma_n} \tag{2.18}$$

where A_n, ω_n and Γ_n represent the amplitude, frequency and line width of the transition of the nth resonance.

In addition, a frequency - independent non - resonant susceptibility $\chi^{(2)}_{\mathrm{NR}}$ is present in the SFG spectrum. This contribution is usually associated with electronic transitions. The non resonant background is expressed with an amplitude A_{NR} and a phase $e^{i\phi_{\mathrm{NR}}}$. The SFG field from (2.8) can be expressed as:

$$\begin{aligned}
\mathbf{E}_{\mathrm{SF}} &\propto \chi^{(2)} \mathbf{E}_{\mathrm{VIS}} \mathbf{E}_{\mathrm{IR}} \\
\mathbf{E}_{\mathrm{SF}} &\propto (\chi^{(2)}_{\mathrm{NR}} + \chi^{(2)}_{\mathrm{R}}) \mathbf{E}_{\mathrm{VIS}} \mathbf{E}_{\mathrm{IR}}
\end{aligned} \tag{2.19}$$

Then an SFG spectrum of multiple modes can be described by the sum of the resonant and non resonant components:

$$\chi^{(2)} \approx A_{\mathrm{NR}} e^{i\phi_{\mathrm{NR}}} + \sum_n \frac{A_n}{(\omega_{\mathrm{IR}} - \omega_n + i\Gamma_n)} \tag{2.20}$$

The SFG intensity is proportional to the square of the field, $I_{\mathrm{SF}} \propto |\mathbf{E}_{\mathrm{SF}}|^2$, thus the absolute molecular orientation is lost. However, the sign of A_n contains information about the absolute

orientation of the molecules at the interface because A_n is proportional to the hyperpolarizability $\beta^{(2)}$ of each molecule, which contains information on the dipole orientation. This sign is often known from phase resolved experiments, in which $\chi^{(2)}$ instead of $|\chi^{(2)}|^2$ is measured [40]. In addition, the maximum entropy method (MEM) [41,42] is sometimes useful to retrieve the absolute orientation of the molecules.

2.1.2 Quadrupole contribution to SFG

As described previously, SFG is a two-photon process originating from the second-order non linear susceptibility $\chi^{(2)}$. It is surface specific if $\chi^{(2)}$ is determined only by dipole transitions. If quadrupole transitions are included, then the bulk may have an important contribution to the SFG signal [43–45].

Briefly, the susceptibility has contributions from the dipole (D) and quadrupole (Q) moment: $\chi^{(2)} \cong \chi^{\mathrm{D}} + \chi^{\mathrm{Q}}$, where magnetic multipole terms and higher electric multipole terms are neglected. χ^{D} and χ^{Q} describe the response to a constant field perturbation and to electric field gradients, respectively [44].

The susceptibility $\chi^{(2)}$ can be decomposed into [45]:

$$\chi^{(2)} = \chi^{\mathrm{D}} + \chi^{\mathrm{Q}} = \chi^{\mathrm{ID}} + \chi^{\mathrm{B}} + \chi^{\mathrm{IQB}} + \chi^{\mathrm{IQ}} \tag{2.21}$$

where χ^{ID} is the induced electric dipole contribution and its equal to χ^{D}, χ^{B} includes the bulk properties and it can be obtained experimentally, χ^{IQB} provides a bulk spectrum from the integration of the quadrupole gradient over the interfacial region and χ^{IQ} originates from the local field gradients of three beams within the interface. χ^{ID} and χ^{IQ} reflect the properties of the interface, whereas χ^{IQB} and χ^{B} include the bulk properties.

For most of the studied systems, such as liquid water, the major contribution is often assigned to the interfacial dipole χ^{ID}.

2.1.3 Time-resolved SFG spectroscopy

Conventional SFG contains information of the vibrations and therefore chemical structure of the interface of a system. During the measurement, the system is in equilibrium, which implies that the interactions of light and matter does not lead to a significant change in the population distribution over time. In order to study the relaxation dynamics of the system, first the system needs to be prepared in a non-equilibrium state and then we can probe its recovery. This perturbation is achieved by an intense laser beam [46–49].

In a time-resolved experiment, aimed at elucidating the vibrational dynamics of interfacial molecules, an intense IR-pump excites a fraction of the molecules from the ground state $v = 0$ to the first vibrational state $v = 1$. Firstly, the IR pump pulse prepares the two level system by creating a vibrational coherence between the $v = 0$ and $v = 1$ states, then part of the population is transferred from $v = 0$ to $v = 1$. Figure 2.4 shows a schematic of a TR-SFG experiment, where an intense IR-pump narrow pulse in frequency excites a part of the population to the first vibrational state, and the system recovery is monitored with the conventional SFG-probe signal. The pump pulse is narrow in frequency, therefore we can excite a specific sub-ensemble within the total population that is being probed.

The SFG signal decreases in intensity when a fraction of the molecules are excited from $v = 0$ to $v = 1$. This decrease in the SFG intensity is known as bleach. The excited state absorption ($v = 1 \longrightarrow 2$) is normally not visible in a SFG experiment, because the SFG intensity depends on the square of the population. Moreover, due to anharmonicity of the OH stretching mode, the SFG signal from the $v = 1 \longrightarrow 2$ transition is $\sim$250 cm^{-1} lower than the $v = 1 \longrightarrow 0$ [50].

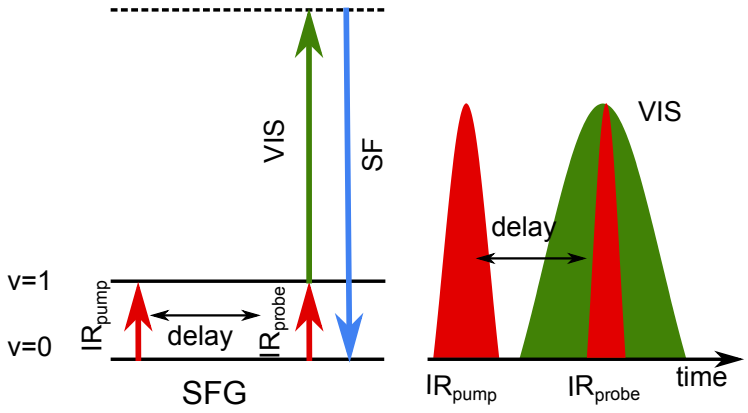

Figure 2.4: Energy levels diagram of a TR-SFG experiment. The intense IR-pump pulse excites the vibrations from the ground state to the first excited vibrational state. The IR-probe and VIS will generate an SFG signal (SFG-probe) that is scanned in time (delay) with respect to the pump pulse. The relaxation dynamics of the system is monitored by the evolution of the SFG signal.

The SFG intensity is proportional to the square of the population difference of the ground state ($N_0(t)$) and the first excited state ($N_1(t)$), where t is the time delay between the SFG-probe and the IR-pump pulse. At time zero the SFG-probe and the IR-pump pulse overlap with each other. Before the system is excited ($t << 0$) the unexcited ground state population is $N_0(t << 0) = N_0$ and the first excited state population is approximately zero ($N_1(t << 0) \approx 0$). When the system is excited with the intense pump, part of the ground state population is transferred to $v = 1$, so that the population of N_0 changes ($\Delta N(t)$), leading to a ground state population of : $N_0(t) = N_0 - \Delta N(t)$ and an excited state of $N_1(t) = \Delta N(t)$. Thus, the corresponding time dependent TR-SFG signal assuming relaxation directly to the ground state is giving by:

$$\begin{aligned} I_{\mathrm{SFG}} &\propto [N_0(t) - N_1(t)]^2 \\ &= (N_0 - 2\Delta N(t))^2 \\ &= (N_0)^2 - 4N_0\Delta N(t) + 4(\Delta N(t))^2 \\ &\approx (N_0)^2 - 4N_0\Delta N(t) \end{aligned} \tag{2.22}$$

For example, if the pump excites 10% of the ground state population the SFG-probe signal at $t = 0$ will be $I_{\mathrm{SFG}} = 1 - 4 \cdot 1 \cdot 0.1 + 4(0.1)^2 = 0.64$.

After the system is excited at t> 0, the excited population relaxes from $v = 1$ to $v = 0$. This relaxation time is an indicator of the vibrational dynamics of the probed systems. This simplified analysis of TR-SFG data is explained further in chapter 6.

2.2 Sum frequency generation setup

Figure 2.5 shows a scheme of the time resolved SFG setup. Briefly, it consists of a laser system, components that generate IR, the SFG generation and the SFG detection. A Ti:sapphire regenerative amplifier (Spitfire Ace, Spectra-Physics) is seeded with an oscillator (Mai-Tai, Spectra Physics) and pumped with a diode-pumped green laser (Empower, Spectra Physics). The amplifier generates laser pulses (5 mJ at 1 kHz) centered at 800 nm with a pulse duration of ∼40 fs. The beam is split in three parts: one part of 1.5 mJ is used to pump a commercial Optical Parametric

Amplifier (TOPAS 1) to generate the IR probe (in blue). Another 1.5 mJ is used to pump a second TOPAS (TOPAS 2) to generate an idler pulse (2200 nm) which is later used to generate the IR pump (in light blue). Part of the 800 nm output (in red) is put through an Etalon to narrow the bandwidth to 20 cm^{-1}.

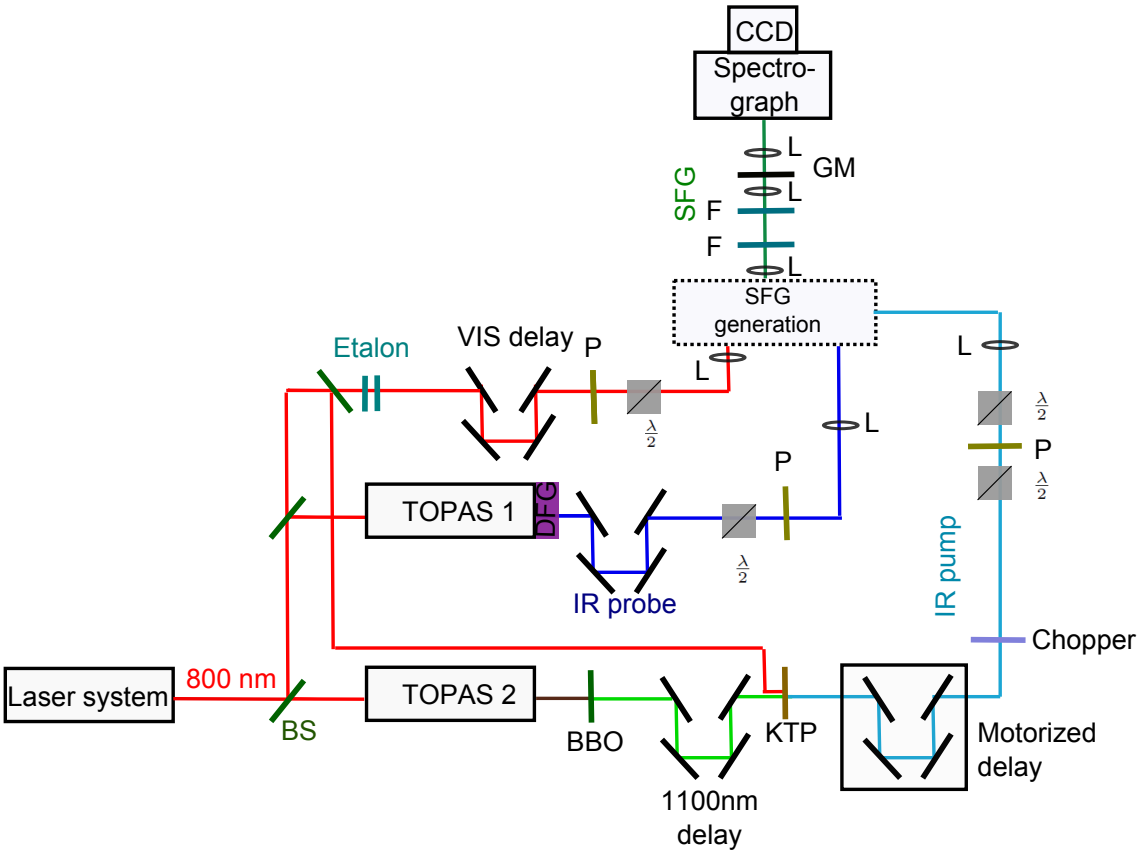

Figure 2.5: Schematic representation of a time-resolved SFG setup. The output from the regenerative amplifier is split in three parts using beam splitters (BS): two parts are used to pump two commercial OPAs (TOPAS) and the rest is kept as 800 nm light. Subsequently, the 800 nm light is split in two parts: one part is mixed with 1100 nm light to generate the IR pump; the other part is passed through an etalon to produce narrow-bandwith VIS probe pulses. The polarization of the three beams (VIS, IR probe and IR pump) is controlled using $\lambda/2$ plates and polarizers (P). The beams are focused onto the sample, and the SFG light (from VIS-probe and IR-probe) is aligned onto the spectrograph. The pumped and unpumped signals are separated by a vibrating galvano mirror, see text for details. L stands for lenses, F for filters and GM for vibrating galvano mirror.

The IR pulses are generated through an optical parametric generation and amplification process (TOPAS, Light Conversion, Lithuania). In the TOPAS, two near infrared pulses (signal S and idler I) are generated. The IR probe is produced by mixing the signal and idler in a silver gallium disulfide crystal ($AgGaS_2$). The difference frequency generation process (DFG, see equation 2.7) results in $\sim 3\ \mu$J pulses, centered around $\sim 3100\ cm^{-1}$ with a full width half maximum (FWHM) of $\sim 300\ cm^{-1}$.

The output of TOPAS 2 is used to generate the IR pump. Firstly, the idler field is frequency doubled in a β-barium borate (BBO ;$7\times7\times3mm^3, \phi = 90\,deg, \theta = 22.2\,deg$) crystal. Subsequently,

the doubled idler ($\sim$ 1100 nm) is mixed with 1 mJ of the 800 nm in a $KTiOPO_4$ crystal (KTP; $10 \times 10 \times 3mm^3, \phi = 0\,deg, \theta = 4.18\,deg$). The OPA process generates IR pulses at $\sim$ 3000 cm^{-1} with FWHM of $\sim$ 100 cm^{-1} and $\sim$ 20 μJ power.

The remaining 1 mJ of the 800 nm pulse is spectrally narrowed by a Fabry Perot etalon (SLS Optics, Ltd) to produce visible upconverting pulses (VIS-probe). The power of the VIS-probe is 20 μJ, with FWHM of 20 cm^{-1}.

Positive lenses are used to focus each beam close to the sample, with focal lengths of 200, 50 or 100 (depending on the experiment) and 200 mm for IR pump, IR probe, VIS probe, respectively at respective angles of 43, 53 and 55 degrees relative to the surface normal (Fig. 2.6).

The IR probe and part of the VIS are used to generate the SFG (in green). The IR pump beam is only used for the time resolved SFG experiments, which reveal vibrational molecular dynamics information, see chapter 6.

The polarization of the beams is controlled by half wave plates ($\lambda/2$) and polarizers (P). The polarizations of the pulses involved in the SFG-probe process are ssp (SFG=s;VI=s;IR=p), and the polarization of the IR-pump is p.

Finally, the SFG light is sent to a spectrometer (Acton, Princeton Instruments) and spatially dispersed via gratings, and focused onto an electron charge couple device (CDD) camera (Newton, Andor). Other optical processes, such as SFG generated from IR pump/ VIS probe, are filtered out using spatial and/or spectral filters (Fig. 2.6).

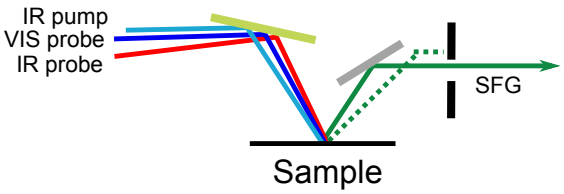

Figure 2.6: Experimental geometry of time-resolved SFG at the sample.

The IR pump pulse is mechanically chopped at 500 Hz. SFG spectra in the presence (pumped) or absence (unpumped) of the intense excitation IR pump pulse are separated by a vibrating galvano mirror (Mirror GM) synchronized to the mechanical chopper at 500 Hz. This mirror, Fig. 2.5, is only moving during time resolved experiments. Moreover, the IR probe is also mechanically chopped to 250 or 164 Hz in some experiments to avoid laser induced surface heating (see chapter 5).

2.3 SFG example: Multiscale effects of interfacial polymer confinement in silica nanocomposites

To exemplify the potential use of SFG, we show here how the method was used to determine the orientation of a polymer at an interface. [2] We compared the interactions of slightly different styrene butadiene polymers (SBR), with a silica surface [51]. Figure 2.7 shows the studied polymers, one with Si-OH modification (F−SBR) at the end and one without it (B−SBR). We investigated the interaction of this polymer with a silica interface in order to understand how silanol functionalization leads to reduced filler aggregation in composites. For this we used SFG to provide information about the molecular vibrations of the molecules at the interface.

Figure 2.8 shows the SFG spectra from the F−SBR/silica interface in red and the B−SBR/silica interface in blue. Spectra from both polymers indicate some degree of molecular order at the silica

[2] "Adapted with permission from ([51]). Copyright (2017) American Chemical Society."

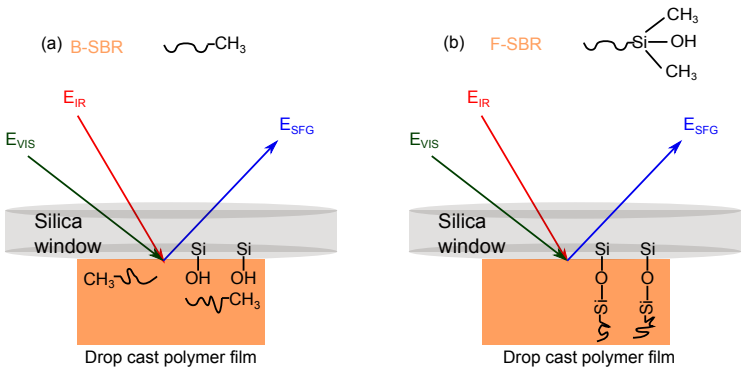

Figure 2.7: Schematic illustration of the SFG measurements of dropcast polymer films on IR-transparent silica window. The two incoming beams are spatially and temporally overlapped at the window-polymer interface and generate a photon with the sum of these frequencies. We studied two samples: (a) a bare SBR (B−SBR) with methyl ending groups and (b) a functionalized SBR (F−SBR) with dimethylsilanol groups.

interface as evidenced by the peaks in the spectra. Control spectra from a THF solution dried on the silica window (without any polymer) showed three and five times less intensity at ∼2950 cm^{-1} compared to B−SBR and F− SBR, respectively. The spectra from the F−SBR silica interface shows clear deviation from the B−SBR silica interface at ∼ 2915 and 2950 cm^{-1}, in addition to a larger overall amplitude.

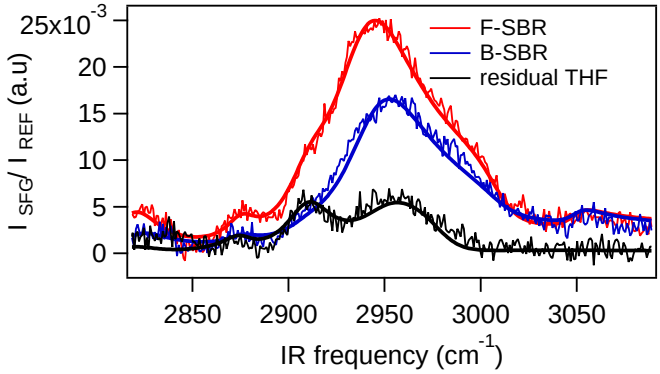

Figure 2.8: Normalized (by a reference spectrum from a gold-coated window) SFG spectra measured from F-SBR (red) and B-SBR (blue) and residual THF without polymer (black). Thick lines are fits to the spectra based on a Lorentzian model (see equation 2.20).

In order to assign peak frequencies and identify the specific moieties contributing to the spectra, we fit the SFG data with a standard model (see equation 2.20). Table 2.1 shows the fitting parameters that were used to obtain the solid lines shown in Fig. 2.8. The first two terms are the nonresonant amplitude (A_{NR}) and its phase ($e^{i\phi NR}$). The sum expression of the equation contains the different vibrations. These resonances have an amplitude A_n at centre frequency in ω_{IR}, with full width half maximum of Γ_n.

From the fitting results and previous work on polymer-glass interfaces for polydimethylsiloxane (PDMS) in contact with silica, we can identify the resonances in the SFG spectra. The PDMS

Table 2.1: Fitting parameters for the C-H stretch region and possible assignments of the bands based on other SFG work [52–54]. Phases are in radians, while frequencies and widths are in cm^{-1}.

Parameter		B-SBR	F-SBR
Nonresonant	Amplitude	0.04	0.04
	Phase (radians)	-0.5	-0.5
C-H_2 symmetric stretch	Amplitude	0.3	0.6
	Frequency	2823	2857
	Width	30	30
C-H_3 symmetric stretch	Amplitude	0.1	0.2
	Frequency	2875	2875
	Width	30	30
Si-CH_3 symmetric stretch amplitude, CH_2 asymmetric stretch, or CH_2 Fermi resonance	Amplitude	0.11	0.42
	Frequency	2875	2875
	Width	20	20
Si-CH_3 asymmetric stretch amplitude, CH_3 asymmetric stretch, or CH_3 Fermi resonance	Amplitude	2.7	3.2
	Frequency	2945	2945
	Width	20	20
CH stretch from C=C	Amplitude	-0.2	-0.6
	Frequency	3010	3010
	Width	20	20
CH stretch from C≡C	Amplitude	0.11	0.12
	Frequency	3050	3050
	Width	20	20

silica interface shows symmetric and asymmetric Si−CH_3 vibrations at roughly 2915 and 2960 cm^{-1} [55]. Similarly, we assign the 2910 cm^{-1} shoulder and 2940 cm^{-1} peak in the F−SBR spectrum to these two Si−CH_3 vibrations (Fig. 2.8, red). In the B−SBR silica sample, the broad signal at 2945 cm^{-1} possibly originates from the CH_3 end group; however, a definitive assignment is not possible. Nevertheless, the identity of the peaks (Si−CH_3) in the F−SBR silica system and the overall larger intensity (compared to B−SBR) show that the polymer Si−OH group in F−SBR is in close proximity to the silica and stabilizes a conformation of the polymer in which the neighbouring Si−CH_3 groups exhibit a noncentrosymmetric organization.

The higher intensity of SFG signal from F−SBR could also indicate that this polymer is more ordered at the silica interface. Possibly due to covalent attachment: Si−OH groups on the SiO_2 could perform a condensation reaction with the Si−OH group from the F−SBR polymer forming R-$(CH_3)_2$-Si-O-Si. X-ray photoelectron spectroscopy experiments give also strong indications for such a condensation reaction for the F−SBR.

In summary, among other characterization techniques, we use SFG to directly show that polymer molecular orientations at the silica surface are strongly constrained for silanol functionalized polymers (F−SBR) compared to nonfunctionalized polymers (B−SBR) because of covalent interaction of silanol with silica.

Chapter 3

Dendrimers and model membrane interactions

Dendrimers are highly branched macromolecules that are synthesized step by step, each step adding an additional layer of branches to the surface of the dendrimer. This synthesis approach provides dendrimers with a well-defined three-dimensional structure [56]. They consist of with a centre (core) and a building block with specifically selected functional groups at the surface. Their size can be controlled by choosing the core size and the number of branching cycles during the synthesis, which defines the dendrimers as first, second, third, etc. generation. The macromolecular solubility and polarity can be tuned by changing the functional groups.

Because their properties can be specifically tailored, dendrimers are known for their applications as nano-carriers for drug delivery; dendrimers can mimic complex natural systems and enzymes [57–65]. Therefore, these macromolecules are of great interest in medicine with applications in drug and gene delivery [66–68]. It has been shown that dendrimers can interact with, and even penetrate, cell membranes. Those interactions are affected by the surface functionalities of the macromolecule. For example, dendrimers with amphiphilic surfaces have shown positive cell uptake and minimum cellular toxicity [69].

Both electrostatic and hydrophobic interactions are important for biological applications [66]. Firstly, it has been concluded that positively charged dendrimers interact with negatively charged bacteria membranes [70]. Secondly, a long carbon hydrophobic functional group on Poly(amidoamine) (PAMAM) dendrimers improves the efficacy of the macromolecules as siRNA delivery and gene silencing agents [71, 72].

Which specific chemical characteristics of the dendrimer functional groups determine whether the dendrimer is good at penetrating cell membranes is largely unknown; most of the literature has focused on trial-and-error methods to optimize membrane penetration. In this chapter, we present a systematic study of different dendrimers aimed at understanding and designing the ideal dendrimer structure for efficient cell uptake. For that, we systematically study differently functionalized dendrimers at different generations. By combining cell uptake assays with surface-specific molecular spectroscopy, we report how small changes of the dendrimer functionalities (different aliphatic and acid groups) or sizes influence the dendrimer cell uptake.

We choose a polyphenylene dendrimer (PPD) [73], see Fig. 3.1, with pyrene as core [74], and a cyclopentadienone as building block with different surface functionalities. The end groups at the surface are either fully negatively charged (with sulfonic acid) or amphiphilically patterned (with an acid and an alkyl group) [75]. In neutral pH solutions, such as water or buffer, the sulfonic acid functional groups on the dendrimer are all negatively charged. These hydrophilic acid groups serve to solubilize the dendrimers in aqueous solution, which is a prerequisite for biological studies.

For the surface-specific vibrational spectroscopy experiments, we use, as a model system for biological membranes, a lipid monolayer. Specifically, we choose DPPC (1,2 dipalmitoyl-sn-glycero-3-phosphocholine, Fig. 3.1). This compound is a zwitterionic lipid that is frequently used as a biomimetic membrane [76].

We investigate how the different dendrimers affect the model membranes at the water-lipid/air interface by studying the changes of the model membrane/air interface upon dendrimer injection. To this end, we use Sum Frequency Generation (SFG) vibrational spectroscopy, see chapter 2. SFG provides the vibrational spectrum of essentially the outermost monolayer of lipids and nearby water at the model membrane interface. We investigate here the OH stretch vibration of the water molecules underneath the lipid monolayer and the CH vibrations of the lipid.

Previous studies using SFG to investigate dendrimer–model membrane interactions [77,78] have shown that, when charged molecules reach the zwitterionic lipid DPPC molecules at a lipid/water interface, the water signal is affected [79] as the water molecules are aligned due to the electrostatic field at the interface. Thus, water vibrations can be used to report back on the presence of dendrimers at the interface. Furthermore, CH vibrations contain information of the molecular orientation and conformation of the lipids in the monolayer [77, 80].

3.1 Sample preparation

The lipids 1,2-dipalmitoyl-*sn*-glycero-3-phosphocholine (DPPC) and 1,2-dipalmitoyl-d62-sn-glycero-3-phosphocholine (DPPC-d62) are obtained from Avanti Polar Lipids Inc (Alabaster, AL, 99% purity). The lipid was diluted in chloroform $\sim$ 1 mg/ml without further purification. Demineralized millipore water was used with a final resistivity of 18 MΩ.

All dendrimers were synthesized by Katharina Bücher and Brenton A.G. Hammer in the department of Klaus Müllen as previously reported [81]. Figure 3.1 shows the molecular structure of an amphiphilic PPD and the lipid DDPC. Table 3.1 lists the hydrophobic and hydrophilic groups of the studied molecules as well as the abbreviations used here. The samples were characterized by Brenton A.G. Hammer with Nuclear Magnetic Resonance using the residual proton of the solvent or the carbon signal of the deuterated solvent as an internal standard. MALDI-TOF mass spectra were measured using a Bruker Reflex II, which was calibrated against poly(ethylene glycol) (3000 g/mol). Samples for MALDI-TOF MS were prepared by mixing the analyte with the matrix (dithranol) in THF in a ratio of 1:50. In some cases, cationization by mixing the matrix with potassium trifluoroacetate or silver trifluoroacetate was performed.

The SFG spectra were collected in SSP polarization (s-SFG, s-VIS, p-IR) and normalized to a non-resonant signal from z-cut quartz. Measurements were performed in a 7 x 7 cm PTFE coated aluminium through (volume of 20 ml). The dendrimers were dissolved in deionized water. Droplets of the lipid solution were added to a water-air interface with a microsyringe, until a surface tension of 26 mN/m was reached. After the lipid monolayer was equilibrated ($\sim$ 20 min) the dendrimer solution was injected into the aqueous subphase. The dendrimer solution was added through a hole in the side of the trough to avoid perturbation of the lipid monolayer. The mixture was stirred for 10 min. Subsequently SFG spectra were recorded. The surface tension was measured before and after dendrimer injection.

3.2 Cell uptake studies

The cellular uptake of PPDs with different hydrophobic groups was studied by flow cytometry using a human lung carcinoma cell line (A549 cells). These experiments were carried out by incubating the cells with 1 μM solutions (in dimethyl sulfoxide) of the dendrimers for 24 hrs. The

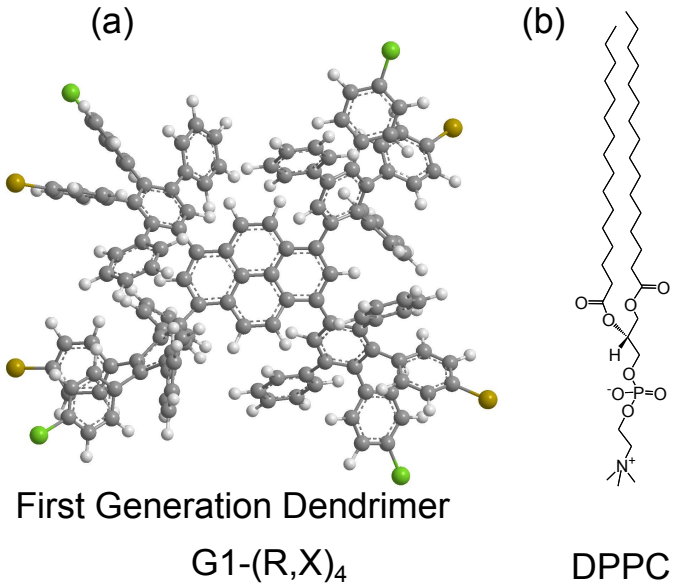

Figure 3.1: Molecular structure of: (a) a first generation pyrene-center polyphenylene dendrimer (PPDs) and (b) 1,2-dipalmitoyl-*sn*-glycero-3-phosphocholine (DPPC) lipid (right). The dendrimers are patterned with different terminal hydrophilic (green) and hydrophobic functional groups (yellow).

Table 3.1: Studied molecules; the first generation (G1) of PPDs has four hydrophobic and hydrophilic groups whereas the second generation (G2) has eight of each of them.

Hydrophobic group (in yellow)	Hydrophilic group (in green)	First generation	Second generation
No hydrophobic group	Sulfonic acid (with twice the amount compared to the other PPDs)	G1-SO_3^-	G2-SO_3^-
isopropyl	Sulfonic acid	G1-iPr,SO_3^-	G2-iPr, SO_3^-
phenyl-isopropyl	Benzenesulfonic acid	G1-Ph-iPr, Ph-SO_3^-	G2-Ph-iPr,Ph-SO_3^-
n-propyl	Sulfonic acid	G1-nPr,SO_3^-	
n-propyl	Carboxylic acid	G1-nPr,COO^-	
phenyl-n-propyl	Benzenesulfonic acid	G1-Ph-nPr,Ph-SO_3^-	G2-Ph-nPr,Ph-SO_3^-
phenyl-n-hexyl	Benzenesulfonic acid	G1-Ph-nHex,Ph-SO_3^-	

amount of PPDs taken up into cells was quantified by the fluorescence of pyrene, which had been incorporated as the core in PPDs and has a very strong blue emission at 450 nm.

The cellular uptake of PPDs with different hydrophilic groups was quantified with a fluorometric assay. The uptake efficiency was quantified by measuring fluorescence from PPDs in the cell lysates and comparing with the original fluorescence of PPDs before applying it to cells. These cell uptake experiments were performed by Weina Liu, Stephan Fischer and Yuzhou Wu in the group of Tanja Weil.

Figure 3.2 shows the results of flow cytometry analysis of A549 cells exposed to dendrimers with different surface functionalities. We have found that the PPDs with linear hydrophobic chains showed enhanced cellular uptake in comparison to the PPDs with branched hydrophobic chains. Furthermore, the second generation dendrimers (Fig. 3.2b) have lower cellular uptake than the first generation ones. As shown in Figure 3.2c, changing the hydrophilic group from -SO_3^- to -COO^- does not affect the cell uptake.

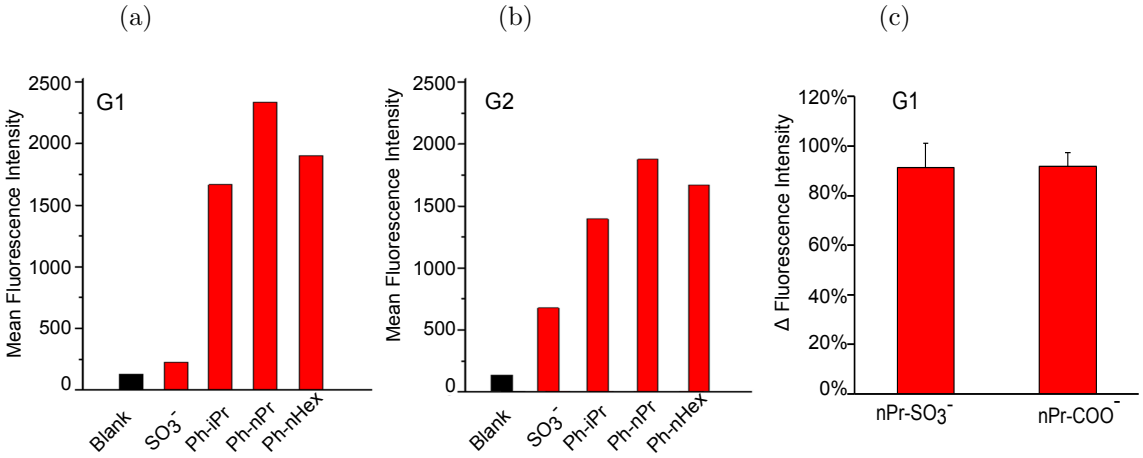

Figure 3.2: Cellular uptake results of (a) first, (b) second generation PPDs with different hydrophobic groups (c) PPDs with different hydrophilic groups.

3.3 Vibrational sum frequency generation spectroscopy results

To obtain molecular-level understanding of the differences in cell uptake, we study the hydrophilic and hydrophobic interactions between the dendrimers and a lipid monolayer at the water-air interface as a membrane model.

We study the effect of the charged dendrimers by injecting them into the aqueous subphase underneath the lipid monolayer. The surface pressure of the DPPC monolayer of 26 mN/m decreases roughly by 2 mN/m for a bulk concentration of 0.5 μM of G1-nPr,COO^- solution. The other dendrimer macromolecules also decrease the surface tension of the monolayer. As was previously reported [77], a lower surface pressure implies that the dendrimer molecules pull the DPPC molecules to the bulk, or that the dendrimer macromolecules are near the interfacial layer. However, in ref [77], X-ray spectroscopy showed that the lipid layer remained intact, ruling out the scenario were DPPC goes into the bulk phase.

The interaction of the dendrimers with the model membrane is then investigated through changes in the vibrational spectrum of both the water and the lipids: if the dendrimers interact with the (model) membrane, the water OH band is expected to increase, because of the concomitant

increase in charge at the interface. Furthermore, the lipid CH modes may also change. The CH_2 and CH_3 signals can increase or decrease due to dendrimer/lipids hydrophobic interactions (insertion of hydrophobic groups of the dendrimer into the lipid layer) and/or rearrangement of the lipids as a result of the presence of the dendrimer.

Figure 3.3 shows the SFG spectrum of a lipid monolayer (in red). In agreement with literature, the spectrum shows the OH vibration of the water molecules at ∼3200 cm^{-1} and sharp peaks due to CH stretching vibrations, between ∼2840 and 2970 cm^{-1}. The water OH stretch mode consists of a broad band for which the centered frequency depends on the hydrogen bond strength [82]. Moreover, with the help of the fitting (see below) in the CH stretch region, five vibrational modes can be observed: the peaks centered at ∼2850, 2875, 2893, 2940, and 2975 cm^{-1} have been assigned to CH_2 symmetric stretching mode, the CH_3 symmetric stretching mode, the CH_2 asymmetric mode, CH_3 Fermi resonance (between CH_2 bending overtone mode and the CH_3 symmetric stretch mode) and the CH_3 asymmetric stretching mode, respectively.

Upon dendrimer injection below the DPPC monolayer, the SFG intensity of the water band increases, as shown in Figure 3.3 for different G1-nPr,COO^- concentrations. This shows that the dendrimers go to the lipid interface. In addition to changes in the water signal, the CH stretching modes also undergo some changes upon dendrimer injection.

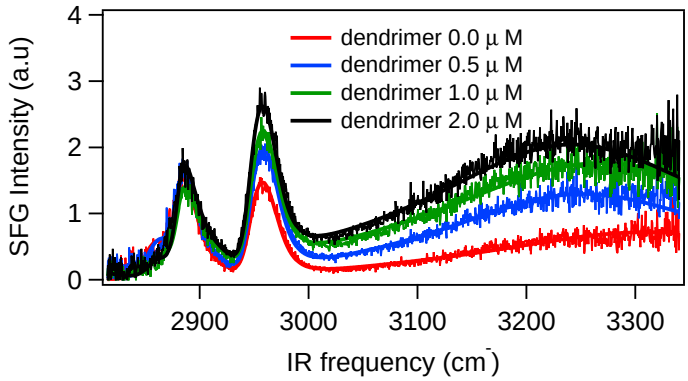

Figure 3.3: DPPC/air interface sum frequency generation spectra for different approximate bulk concentrations of G1-nPr,COO^-. The fitted data (see text) is shown as solid lines.

A control experiment to study the effect of the molecules at the water/air interface shows that dendrimers do not go to the interface if no lipid is present. Figure 3.4a shows the water-air interface OH stretching bond before and after adding G2-Ph-nPr,Ph-SO_3^-. The figure shows that the water band is not affected by the PPD. This implies that G2-P-nPr,Ph-SO_3^- is not surface active; similar results are obtained with the other studied PPDs.

Changes in the CH stretch region can originate from two sources: the dendrimer has ample CH groups, so the vibrational intensity can originate from the dendrimer itself; alternatively, the changes can originate from conformational changes of the lipid layer. To exclude that changes of the CH region are from dendrimer vibrations, we performed experiments with a deuterated lipid. Figure 3.4b shows the SFG spectra of the deuterated-DPPC/air interface before and after dendrimer injection. The spectra show, besides the OH stretch a weak CH signal at ∼2965 cm^{-1} originating from the CH_2 antisymmetric stretch vibration [83]. The water signal is enhanced when dendrimers are injected, but new CH vibrations were not detected. Thus, we conclude that dendrimers are not detected at the lipid-air interface, which is explained by their high symmetry; molecules with inversion symmetry are SFG-inactive.

To quantify changes in the vibrational response of the DPPC monolayer due to interactions with

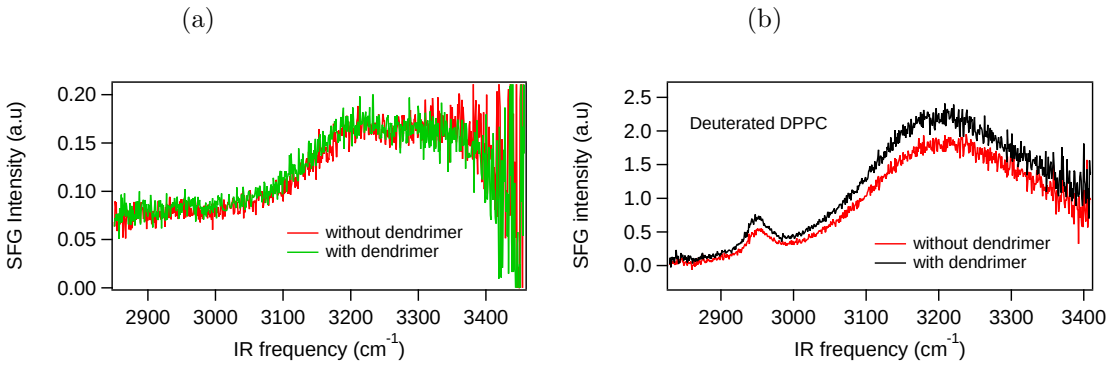

Figure 3.4: (a) SFG spectra of the water-air interface with and without G2-Ph-nPr,Ph-SO_3^- PPDs, showing that the dendrimers are not surface active at the water/air interface. (b) SFG spectra of a deuterated-DPPC/air interface before and after injection of G1-Ph-nPr,Ph-SO_3^- solution. The change in the water signal indicates the interaction of the dendrimer with the lipid monolayer.

the dendrimers, the SFG spectra were fitted using a well -established method, see chapter 2. For each measurement, initially the DPPC spectrum was fitted (solid lines in figure 3.3). According to literature, all bands have negative sign (A_n) except the water band, and the asymmetric CH_2 and CH_3 stretch vibrations [40, 84]. Upon dendrimer injection, the nonresonant parameters, position of the CH bands and bandwidth, are fixed. All amplitudes and parameters of the OH band are set free. The bandwidth of the OH band is typically 300±50 cm^{-1}.

The changes of the amplitude of the OH band inferred from the fits of the SFG spectra of the G1-nPr,COO^- dendrimer interacting with the lipid monolayer (Fig. 3.3) are presented in Fig. 3.5 (in blue). This figure shows the ratio of the amplitude and the width of the SFG response of the OH stretch vibration inferred from the fit as a function of the dendrimer concentration. The water intensity is a direct measure of the number of oriented water molecules at the interface, which, in turn, is determined by the dipole field created by the lipids. To a first approximation, the amplitude of the OH band is proportional to the dipole field at the interface, which is proportional to the dendrimer density. As such, the OH signal is a direct and quantitative reporter of the dendrimer adsorption at the lipid interface.

The water intensity increases upon addition of dendrimers. Clearly, the interaction of the dendrimers with the lipids is quite strong. No changes of the water band were observed when only buffer solution (0.25 and 0.5 ml) was added.

To study the effect of the linear hydrophobic functional groups and different hydrophilic groups, we performed similar experiments with a variety of dendrimers (Table. 3.1). Figure 3.5 shows the OH band amplitude vs dendrimer concentration for first generation dendrimer with different linear alkyl hydrophobic groups (n-propyl and Ph-n-hexyl) and terminated acidic groups (-SO_3^-, and -COO^-). The SFG amplitude of the water band amplitude at 2.0 μM dendrimer concentration seems to be similar for PPDs with different linear alkyl and acid ending groups.

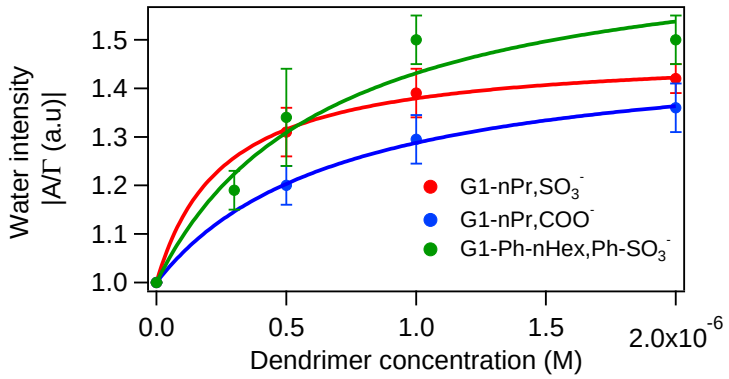

Figure 3.5: Amplitude of the water band as function of different dendrimer concentrations at the lipid/air interface for PPDs with different hydrophobic (n-propyl or Ph-n-hexyl) and hydrophilic (-SO_3^- or -COO^-) functional groups.

The change in SFG amplitude contains information about the lipid-dendrimer interactions. These interactions can be seen as an equilibrium between dendrimers adsorbed to the lipid binding site and dendrimers that are free in solution [85]. This can be described using a Langmuir model with identical, non-interacting interaction sites : DPPC+dendrimer↔DPPC-dendrimer.

The SFG amplitude (A_{SFG}) is proportional to the number of molecules, see equation (3.1):

$$A_{\mathrm{SFG}} \propto \chi^{(2)} = N\langle\beta\rangle/\epsilon_0 \tag{3.1}$$

where $\chi^{(2)}$ is the second order nonlinear susceptibility, N the density of molecules on the surface, β the molecular hyperpolarizability and ϵ_0 the vacuum permittivity.

Thus, mathematically, an isotherm that follows a Langmuir model for the normalized SFG amplitude [86], can be expressed as:

$$A_{\mathrm{SFG}} = \left(\frac{K_B \cdot c}{1 + K_B \cdot c}\right) A_{\mathrm{SFG,max}} + 1 \tag{3.2}$$

where $A_{\mathrm{SFG,max}}$ is the SFG amplitude probed at the interface when the surface is saturated with PPDs, c is the concentration of macromolecules. K_B is the binding constant that describes the equilibrium between the molecules interacting with the lipid monolayer and those that are free in solution.

The results of the fitting are presented as solid lines in figure 3.5. As observed, the model describes the data reasonably well.

From the Langmuir model, important thermodynamic parameters can be extracted. Table 3.2 summarizes the K_B values extracted from the fitting. In general, K_B values between 10^5 and 10^7 are illustrative of the high affinity of the dendrimers for the lipids, as has been previously reported for protein-ligand interactions [87].

This analysis shows that the K_B is not significantly different for the dendrimers with various hydrophilic functional groups (Table 3.2). The surface activity is thus independent of the dendrimer hydrophilic ending groups. This finding is in agreement with cellular uptake results (Fig. 3.2). The K_B is also similar for PPDs that have n-propyl or phenyl-n-hexyl hydrophobic groups.

To further investigate the role of different hydrophobic groups, we have studied a whole variety of dendrimers (Table. 3.1). We added dendrimer solution to the subphase till the SFG signal did not significantly change any more. We focus below on the qualitative difference between the PPDs.

Table 3.2: Thermodynamic parameters of macromolecules-lipid monolayer interaction obtained from fitting the data of figure 3.5, with a Langmuir model.

Dendrimer macromolecule	$K_B(M^{-1})$
G1-nPr,SO_3^-	$3.9(\pm 2.9) \cdot 10^6$
G1-nPr,COO^-	$1.4(\pm 1.0) \cdot 10^6$
G1-Ph-nHex,Ph-SO_3^-	$1.2(\pm 0.7) \cdot 10^6$

Figure 3.6a shows the ratio of amplitude and width response in the SFG spectrum of the water band as function of increasing concentration for first generation dendrimers with different hydrophobic groups. The data was normalized to the lipid signal without dendrimers. The OH band shows the least change upon injection of the G1-SO_3^- dendrimer, which does not have any alkyl groups. This dendrimer, even though it has eight negative charges, stays in the bulk rather than at the interface. We therefore conclude that, purely electrostatic interactions are insufficient to drive dendrimers to the interface.

The amplitude of the water OH stretch mode shows some increase when the dendrimers have an isopropyl as the non-polar group (green data points). When the hydrophobic functional group is a linear alkyl chain, like n-propyl or n-hexyl, the change in amplitude upon dendrimer injection is clearly the highest. The water band increases in intensity in the following order: non alkyl functionality < isopropyl < phenyl- n- hexyl = phenyl- n-propyl = n-propyl. Interestingly, this trend is in agreement with the cell penetrating experiments, see section 3.2.

These qualitative observations indicate that the interactions of the dendrimers with the lipid monolayer are primarily driven by hydrophobic interactions. The electrostatic changes of the charged dendrimers at the interface allow us to measure the hydrophobic interaction, however, they do not contribute significantly to the interaction strength of the dendrimers with the lipid.

In a previous study, some of our colleagues had concluded that a second generation dendrimer interaction with a lipid monolayer was dominated by electrostatic interactions [77]. The variation of the hydrophobic groups in the current work, however, clearly shows that hydrophobic interactions control the dendrimer/model membrane interfaces. Of course, we cannot exclude that the electrostatic interactions will also affect the dendrimer/lipid interface and cell uptake, but it clearly plays a minor role.

To study the effect of more charges (eight instead of four) and the size of the dendrimer on the interaction of the dendrimers with the model membrane, we performed similar experiments on second generation dendrimers. Figure 3.6b shows the inferred water intensity as a function of concentration for two types of second generation macromolecules. Again, the PPD with a linear alkyl group is more surface active than the branched one.

From varying the alkyl and hydrophilic groups we concluded that the hydrophobic interactions dominate. If the hydrophobic interactions indeed dominate a likely mode for interaction for the dendrimer alkyl chains is to insert into the lipid monolayer. If that is the case, the order of the DPPC molecules at the interface is expected to change. The ratio of the CH_2 and CH_3 symmetric stretch amplitudes can be used to measure empirically the order of the lipid chains. SFG is forbidden in centrosymmetric media, and therefore a fully ordered all-trans chain of methylene groups has no contribution from the CH_2 groups. In contrast, such an ordered system should have a large CH_3 signal from the end group of the monolayer as these must be well-aligned as a result of the ordering. On the other hand, for a disordered monolayer, gauche defects appear that break the symmetry in the methylene alkyl chain, causing an increase in the intensity of the CH_2 signal and decrease of the CH_3 signal [37]. As such, the ratio of CH_2 / CH_3 signals from the lipid provides a direct measure of the degree of disorder in the alkyl chain of the lipid [80].

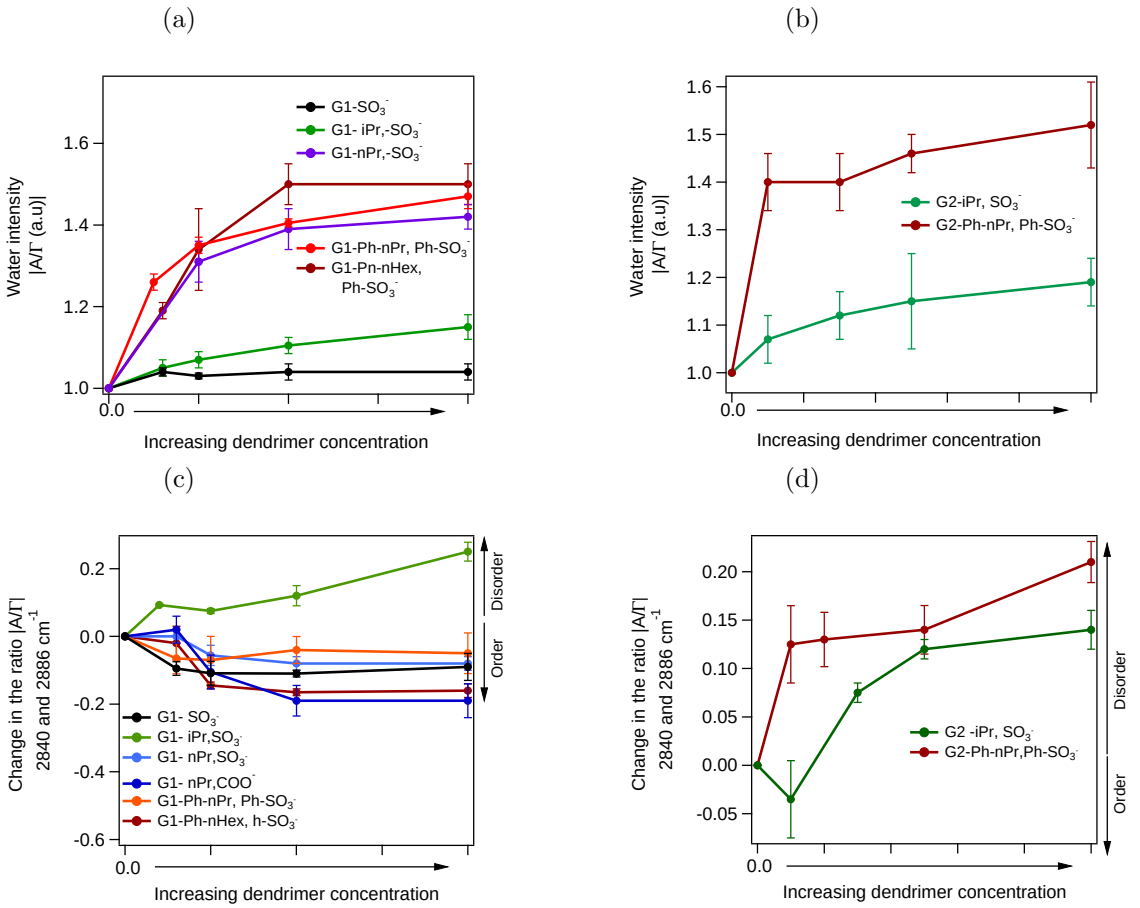

Figure 3.6: Water band amplitude, divided by the linewidth of the resonance (see text) for increasing dendrimer concentration. For the (a) first and (b) second generation PPDs. The data were normalized to the amplitude of the water signal beneath the lipid monolayer in absence of dendrimers. The solid lines are guides to the eye. Change in the ratio of the amplitude of the CH_2 symmetric stretch and the CH_3 symmetric stretch response of the lipid alkyl chain within the monolayer interacting with first (c) and second (d) generation dendrimers. Negative values indicate that the presence of the dendrimer induced disorder in the alkyl chain of lipids constituting the model membrane, whereas positive values indicate order.

Figure 3.6c and d show the change in the CH_2 / CH_3 ratio upon addition of the dendrimer to the lipid monolayer as function of increasing dendrimer concentration. A negative value for the change in the CH_2 / CH_3 ratio indicates an increase in order in the lipid alkyl chains; if the change is positive, the monolayer becomes more disordered.

The results for the first generation dendrimers are plotted in figure 3.6c. The graph shows that for the first generation dendrimers, upon interaction with the linear alkyl chains terminal groups of the dendrimers order the alkyl chains of the lipids. On the contrary second generation PPDs (Fig. 3.6c) the lipid monolayer disorganizes. Apparently, a different effect dominates in this case. A possible explanation could be domain formation. Second generation dendrimers may form high density lipid patches at locations where the dendrimers bind, so the surroundings have less lipids, which are more disorganized. One typically observes a decrease in the lipid order when small ordered domains are formed; SFG will mainly probe the more disordered lipids.

First generation dendrimers are $\sim$ 2.8 nm in diameter whereas the second generation ones are $\sim$ 4.2 nm. [69]. This size difference may explain why second generation dendrimers disorganize the monolayer in the model membrane. Larger dendrimers may create holes in the lipid monolayer. For example, it has been reported that fifth generation poly(amidoamine) dendrimers create holes in lipid bilayers, whereas third generation ones do not [88].

Moreover, second generation dendrimers have less cellular uptake than first generation ones (Fig 3.2). This lower cellular uptake difference may be explained by the high density lipid patches. This may prevent the dendrimers to enter the cell as efficient as their first generation type.

In summary, the results have shown that the hydrophobic interactions dominate the interaction between dendrimers and the model membrane, and influence the cell uptake of the macromolecules (Fig. 3.6). To investigate the role of the negative charge we compare sulfonate and carboxylate groups. The results of both SFG and cell uptake are similar for those acids, which supports the hypothesis that the interactions are dominated by the hydrophobic chains (Fig. 3.5).

3.4 Conclusions

In this study, we have investigated the ability of dendrimers to penetrate cells, with cell studies and SFG experiments to probe the interaction of dendrimers with model lipid membranes.

Aliphatic chains on the surface of the dendrimers have a direct influence on the surface activity of the studied dendrimers at the lipid/air interface and on cell penetrating results. When linear alkyl chains are present at the end group of the dendrimers, the amount of dendrimers at the interface is higher than when branched alkyl chains functionalize the macromolecule. Hydrophobic interactions between membranes and dendrimers are necessary to enhance cell penetration and surface activity.

Dendrimers with different anions (-SO_3^- or -COO^-) behave similarly at the lipid/air interface and exhibit similar cell penetrating characteristics.

Cell uptake results show that first generation molecules have better penetration than the second generation ones. Interestingly, SFG experiments show that the lipid layer gets disordered upon interaction with second generation PPDs while first generation PPDs in general increase the order.

When the PPDs penetrate a cell, they first have to bind to the cell membrane to then pass through it. The binding of the dendrimer with the membrane seems to be a good predicator of the cellular activity. It seems that this binding to the membrane is the rate limiting step in the total process.

In conclusion, we found that an ideal pyrene core dendrimer with good cell uptake results is a first generation PPD, which has amphiphilic functionalities, with an hydrophobic part and a linear alkyl group.

Chapter 4

Single crystalline ice

This chapter explains how to reproducibly obtain single crystalline ice samples. The reliability of this process is a prerequisite for optical studies on ice surfaces, where molecular knowledge and reproducibility of the optical spectra is needed, see chapter 5. Moreover, this section explains how to crystallographically orient and characterize the ice samples.

Figure 4.1 shows the crystallographic structure of hexagonal ice, with the hexagonal prism composed of three unit cells, see chapter 1. The optical, or c-axis, coincides with the hexagonal prism axis. The a-axis is perpendicular to the c-axis and is perpendicular to the secondary prism face.

The experimental results of this chapter were obtained in collaboration with Marc-Jan van Zadel. Together we developed equipment for making single crystalline ice. The X-ray analysis, summarized in the appendix, was performed by Markus Mezger.

4.1 Crystal fabrication

Usually, water freezes non-uniformly, leading to grains with different crystallographic orientations. The size and orientation of the grains depend on the nucleation sites, temperature, pressure and growth velocity. It is very difficult to control the crystallographic orientations and grain sizes by simply freezing water in a freezer.

General techniques for growing single crystalline ice used in our laboratory are: "lake", modified Bridgman, and the seed extraction from a melt methods, described in the following sections:

"Lake"

We refer to this method as "lake", because it resembles the single crystal ice growth on the surface of lakes, where the ice grows in one dimension at the water-air interface on a clear and cold night [89]. The simplest growth method that produces thin and small (1x1x0.3 cm) single crystals is to freeze water inside a wide beaker. A temperature gradient in the water phase with the highest temperature at the bottom ensures that ice growth will start at the water-air interface. The sample must be removed from the beaker before the lateral growth allows the crystal to touch the walls of the container, otherwise polycrystalline ice will be produced. Of course, more sophisticated techniques have been reported based on this method. For example, Turner et al. [90] have made single crystals in a modified calorimeter where the lower and upper parts had the highest and the lowest temperature, respectively. Khusnatdinov has also produced single crystalline ice by intensive evaporation of water in vacuum in only 10-15 min [91].

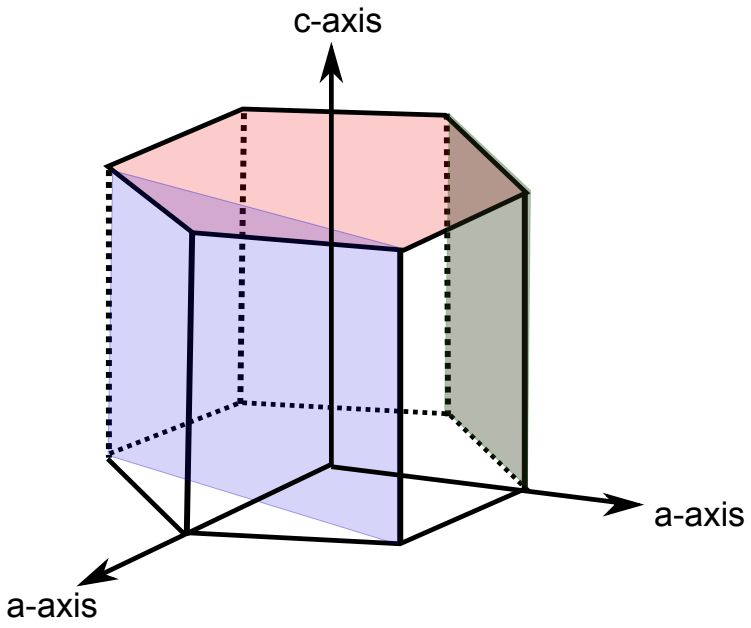

Figure 4.1: Cartoon of the crystallographic ice structure with the principal crystallographic axis. The figure also shows the basal {0001} (in red), primary prism $\{10\bar{1}0\}$ (in grey) and secondary prism plane $\{11\bar{2}0\}$(in blue).

Modified Bridgman method

In general, this method uses a glass growth tube (crucible, Fig. 4.2) filled with liquid water that is lowered into a column of coolant. As the tube is lowered down, ice is formed. Initially, polycrystalline ice is formed in the nucleation tip, and the ice then grows as a single crystal through a twisted capillary inside the main tube. Our Bridgman-Stockbarger apparatus, based on [92–95], consists of two concentric cylindrical baths (inner and outer bath), and a shelf with a hole, as shown in figure 4.2. A 70% glycol/water (volume/volume) mixture is used to cool down the baths to 270 K. The upper region of the inner bath has a coiled heating element that generates a temperature gradient in this bath. The inner bath is at 276, 273 and 270 K in the upper, shelf and bottom parts, respectively. The new ice is formed at the shelf region.

Figure 4.2(b) shows the growth tube crucible that is used during growth. It has four main parts: a tip, a V shape, a neck and the main tube of about 42 cm in length. The crucible is filled with degassed water that freezes in a controllable manner during the growth process, described as follows.

Ice crystallization inside the crucible is initiated by freezing water in the tip in a methanol/dry ice (95 K) bath. After that, the crucible is placed in the Bridgman-Stockbarger apparatus with the tip just below the shelf (Fig. 4.2). The system equilibrates, and after half an hour the stepper motor starts lowering the crucible into the bath, forming new ice at ~ 150 μm/hour.

The ice that grows from the tip is not a single crystal. Many ice domains reach the wall before the neck and stop growing. A single crystal face is selected by the neck and forms single crystal ice throughout the main crucible tube. The ice continues growing in the tube for two weeks as the crucible is slowly lowered. Finally, the crucible containing the newly formed ice is removed from the apparatus and the ice is extracted. The ice crystals formed in this way tend to have the

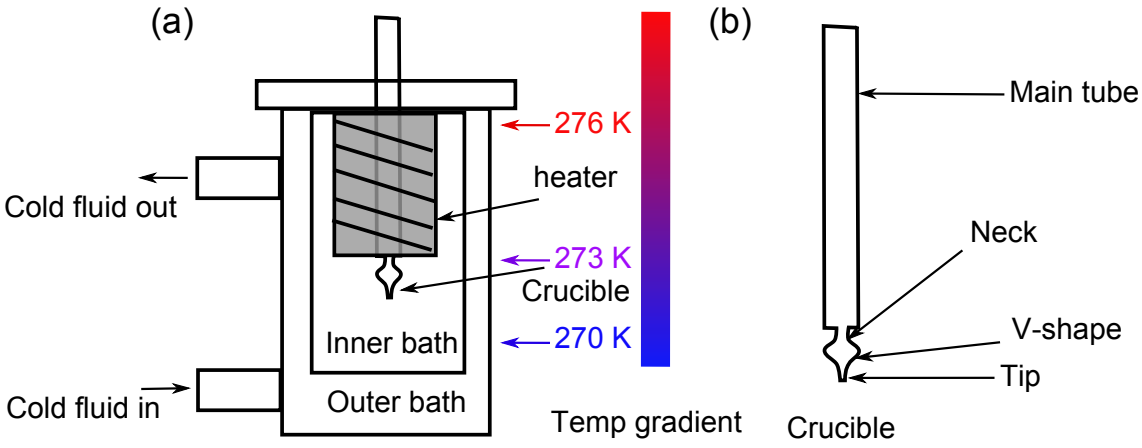

Figure 4.2: (a) Cross section of the modified Bridgman-Stockbarger apparatus. (b) Crucible with its main parts.

secondary prism approximately perpendicular to the growth direction [96].

After growth, the ice samples are 2.54 cm in diameter and 5 cm in length. The first 2 of the 5 cm were almost always single crystals, however, the rest of the sample usually had other crystalline domains or defects. Ideally, the ice should grow from the center of the crucible, resulting in a sample with a positive meniscus, Fig. 4.3a. However, we observed an almost always negative meniscus, Fig. 4.3b. The reason for this is that other ice domains may be produced from nucleation from the walls of the main crucible tube. The ice growth then from the centre of the crucible and the glass-water interface. Unfortunately, we were not able to control the competition between these two nucleation parts, which lead to different domains or defects in the ice.

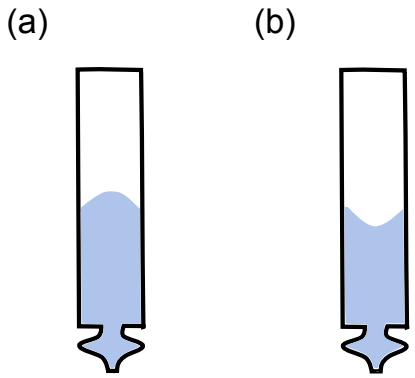

Figure 4.3: Ice growth (a) from the centre of the crucible and (b) from ice/glass are nucleation plus the centre of the crucible. The ice is represented in blue.

The modified Bridgman process needs precise temperature control, achieved by a Proportional/Integral/Differential (PID) mechanism, from a LakeShore 335 electronic temperature controller. Furthermore, vibrations affect the delicate growth process, thus the system is placed on a floating optical table. As impurities on the glass components give rise to polycrystalline samples, they are eliminated by thoroughly cleaning the glass components with a mixture of concentrated sulphuric acid and Nochromix, followed by abundant deionized water.

Seed extraction from the melt technique

This method consists of extracting a single crystalline seed from a melt [97, 98]. Figure 4.4 shows the principal elements of this method: the cold surface, the crystalline seed, the melt and the new ice sample. The initial seed can be obtained from the Modified Bridgman or from the "lake" method.

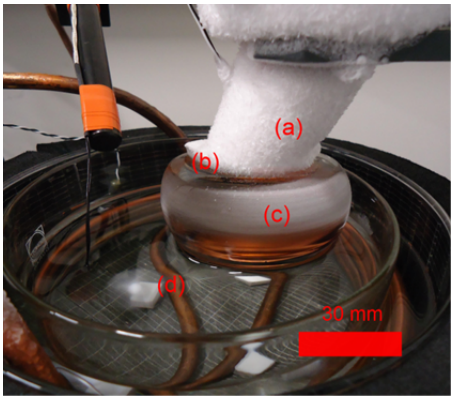

Figure 4.4: (a) Copper pin, (b) crystalline seed, (c) new ice sample, (d) supercold melt.

The seed has a crystalline orientation that is copied by the new sample during the growth process. Thus, it is important to check and correct the crystallographic orientation of the seed. This checking facilitates the sample orientation afterwards. We orient the seed so that the growth direction is parallel to the c-axis [0001] because the basal plane has lower surface energy than other faces at the air-ice interface, favouring growth in this direction. Ketcham and Hobbs produced single crystals from a polycrystalline seed and observed that the basal oriented grains had preferential growth [99].

Prior to the growth, the seed is frozen onto a copper pin, kept at 248 K, and attached to a Peltier element with liquid back-cooling. As soon as the seed and the copper pin are well connected, the surface of the seed is melted with a heat gun and the resultant water drops are blown away with N_2. With the surface of the seed still being liquid, the copper pin with the seed is quickly lowered to make contact between the seed and a constantly stirred liquid water melt, kept at 272.85 K. The seed is initially allowed to grow in the melt for half an hour. After confirming that the seed is growing in the melt, the seed is slowly raised at 5 mm/hour to allow the boule to grow in diameter and in length. Typically, after one day of growth, we obtain a 30 mm long cylindrical single crystal boule 60-90 mm in diameter. If the process takes place overnight, with the help of a peristaltic pump that adds more liquid water to the melt, the samples have typically a diameter of 60-90 mm and length of 100 mm. The finished crystal is stored in a freezer at 253 K. After the first single crystal sample is produced, a slice from it is used as the seed for the following growth.

As mention before, the melt is constantly stirred at 650 rpm. This action prevents bubble formation at the water-ice interface, which can become supersaturated with dissolved air. Also, agitation does not allow temperature gradients and thus prevents the formation of new small crystals on the surface of the melt. The melt temperature (272.85 K) is controlled by a mixture of glycol/water with a Thermo PC 200 chiller. It is important to avoid ice needles in the solution. If this occurs, it is necessary to increase the chiller temperature. The beaker that contains the melt is occasionally cleaned with a mixture of Nochromix and concentrated acid, and on a regular basis with kripton detergent, and rinsed multiple times with deionized water.

This method produces large single crystalline ice crystals and is very reproducible. All the ice

samples measured in this thesis are fabricated with this method.

4.2 Ice characterization and orientation

After growth, the single crystallinity of the ice sample is verified by cross polarizers. After confirming a successful ice growth, the ice sample is cut into slides with a Proxon bandsaw in a freezer at 253 K and oriented with crossed polarizers and Formvar etching as described below. The ultimate crystal orientation verification is performed with X-ray analysis (see 4.4.1).

A test slice of ice is used to determine the orientation of the whole crystal. This piece is subsequently discarded, and a fresh piece is used for optical measurements.

4.2.1 Cross polarizers

The velocity of polarized light in an isotropic material is the same in all directions. However, if the material is anisotropic, like ice [100], the light is generally broken into waves with different velocities called ordinary and extraordinary. Such crystals are called birefringent (Fig. 4.5(a)). The ordinary wave travels with the same velocity in all directions. However, the speed of the extraordinary wave varies throughout the crystal. The waves meet in two points, where the ordinary wave and the extraordinary have the same velocity. Figure 4.5(b) shows the waves; the points where they meet form the optical axis, which for ice coincides with the c-axis (Fig. 4.1). The birefringence of ice is small, with an extraordinary index of refraction $n_e = 1.3105$ and the ordinary $n_o = 1.3091$ [17].

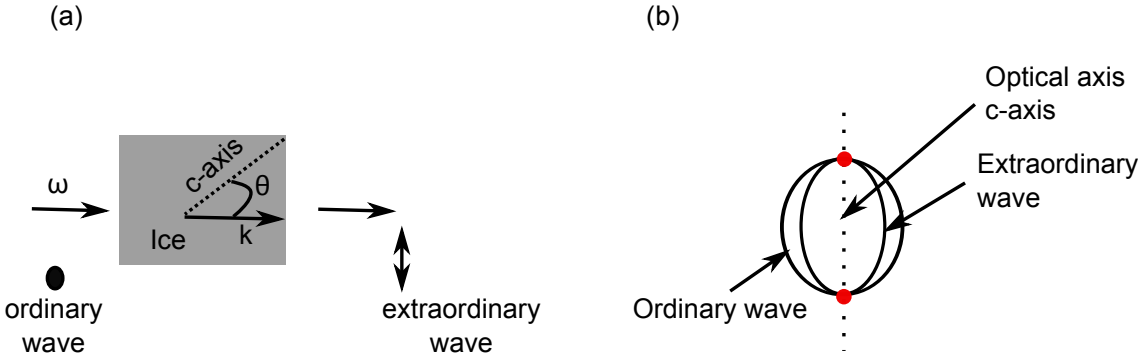

Figure 4.5: (a) Propagation of light through a birefringent material, such as ice. ω is the frequency, in this case visible light. θ is the angle between the propagation of light and the optical axis vectors. The extraordinary and ordinary waves are orthogonal to each other. (b) The spherical vector surface for a birefringent material. Ordinary and extraordinary waves in ice, where the extraordinary wave travels slower throughout the ice than the ordinary one. The dotted line represents the optical axis, also known as c-axis. At the red points the waves have the same velocity. Based on ref [17].

Because of these optical characteristics, it is possible to determine the crystallographic c-axis of the ice sample if it is illuminated with polarised light. Figure 4.6a shows a universal stage [100] in which the ice sample is placed between two cross polarizers called analyzer and polarizer. This stage is illuminated from below with unpolarized light. When there is no ice in the universal stage, light from the first polarizer is completely extinguished by the second one (analyzer), since the polarizers are placed orthogonal to each other. When ice is placed between in the crossed polarizers, due to its birefringent nature, the electric vector of the light that interacts with the sample is divided into ordinary and extraordinary waves. After passing trough the ice, the two waves will be out of phase, so the polarization of the outgoing light is changed. This causes the

sample to appear bright. The outgoing light is extinguished (and the ice appears dark) for three orientations of the sample: when the optical axis of ice is aligned with either the polarizer or analyzer or when the c-axis is parallel to the line of sight.

The home built universal stage (Fig. 4.6b) has four partially independent rotations. A1 rotates the sample in the horizontal plane, A5 moves the whole stage, rotating both the ice and analyzer in the horizontal plane, A2 rocks the sample in the east-west plane and A4 in the north-south plane. Detailed explanation can be found in sec. 4.4.2.

When the crystal is polycrystalline, different domains will look dark at various A1 angles. They will be immediately observed. For example, the ice in figure 4.6c shows at least three domains, these domains resemble the head of a rabbit, the body and the rest of the sample.

Figure 4.6d presents a single crystalline slide of a secondary prism face of ice, the darkness of this crystals is the same in the whole sample. By rotating A1 and observing when the sample appears dark, one can determine the two orientations of the sample where the light is extinguished. However, in either of these directions the optical axis is co-linear to either the polarizer or the analyzer, we distinguish these two cases by rotating the A2 and A4 angles. For further explanation see 4.4.2.

When looking at the basal plane, the optical axis is parallel to the line of sight. In this case there will be no extraordinary light, and the crystal will always remain dark no matter how it is rotated by the A1 angle of the universal stage.

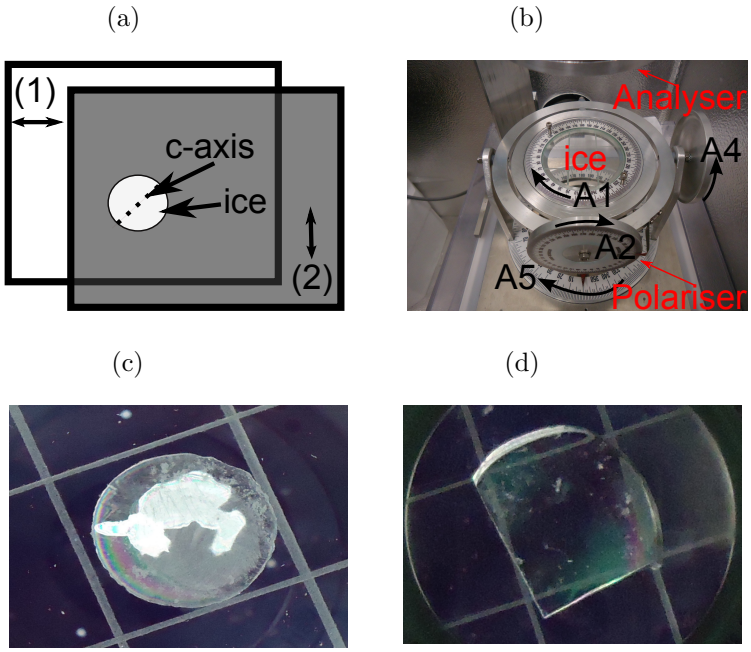

Figure 4.6: (a) Scheme of a universal stage where a polarizer (1) is placed orthogonal to an analyzer (2), the ice sample is in-between them. (b) Universal stage with the four independent rotations, (c) Polycrystalline ice with at least three domains, (d) single crystalline ice with the c-axis parallel to the sample (prism plane), in the picture the flat cuts in the left and bottom allow us to keep track of the c-axis. The ice slices are 2.5 cm in diameter.

Reading the rotation angles on the Risgby stage may produce significantly uncertainties. The correct reading of the angles of the four rotations is highly depend on the eyes of the experimentalist. One must be able to distinguish specific angles of extinction, which is extremely subjective. It is absolutely necessary for the observer to be directly centred over the crystalline domain of the

ice samples. Keeping the sample in the centre and following the lines of the glass in the stage (Fig. 4.6b) makes the task easier. Moreover, the measured angles can differ from the true ones due to the large differences between the refractive indices of air and ice. Finally, information of the a-axis (Fig. 4.1) cannot be obtained by the universal stage. Knowledge of this axis is necessary for an accurate crystal orientation [101]. For this reason, we mainly use the universal stage to check if our new ice samples are indeed single crystalline, and to roughly estimate if we have a basal or prismatic surface oriented sample. We mostly use the Formvar etching (see subsection 4.2.2) for determining the orientation of the ice crystals.

4.2.2 Formvar etching

Surface etching is a useful method for determining crystal orientations in metallic and non-metallic materials [102]. Pits with crystallographic information from the ice surface are obtained by a thermal and anisotropic etching, known as Formvar etching. An ice substrate is covered with a 2% solution of polyvinyl formal (Formvar) dissolved in ethylene dichloride. After the solvent is evaporated, a polymer film is formed on the ice [96, 103]. The etch pits are formed due to evaporation through very small randomly distributed holes, caused by the inhomogeneous coverage of the Formvar polymer [17, 104].

To obtain the etch pits, we first cut a thin slice of ice $\sim$ 10-20 mm thick and mount it to a glass microscope slide. The ice is mounted by warming the glass underneath with one's fingers until a thin layer of liquid water is observed between the ice and the slide. After the liquid water is solidified, the ice sample is flattened with a custom modified microtome (Swift and Anderson Rotary Microtome). Then the sample is placed in the microscope and a layer of Formvar is applied with a cotton tip on the surface. The pits typically start to appear in the ice surface after 25 minutes, when the solvent is evaporated. For better results, the freezer can be left open after the application of the chemical, to increase airflow and accelerate evaporation of the ethylene dichloride.

Figure 4.7a shows different pits [104]. The shape of each pit depends on the lattice structure of the hexagonal crystal. Thus from the pit shape it is possible to determine the orientation of both a-axis and c-axis (Fig 4.1) [105]. The etch pits of basal, primary and secondary faces are illustrated in figure 4.7(b),(c) and (d), respectively. Those pits follow the shape of the hexagonal crystalline ice structure. Pits of a perfect basal plane look like hexagons, the ones for the primary prism resemble a flat table and for the secondary prism place a house roof. The photographs were taken with a microscope (Olympus BX40, a magnification of 10X and a camera Nikon Digital Sight DS-U2) at 253 K.

Sometimes, the surface of ice, after the growing process, does not have the desired orientation for our studies (i.e. basal, primary or secondary prism planes). Then the ice sample has to be tilted and rocked at specific angles before cutting it cut with the bandsaw. The etch pit shape provides information on those specific angles. The experimental procedure about how to tilt and rock the sample is described in the following paragraphs.

Figure 4.8a represents the crystallographic hexagonal structure of ice where the c-axis is tilted by $\sim 20^\circ$ and the a-axis is rocked by $\sim 5^\circ$ (Fig. 4.1). Similar to the spherical coordinate system, the angle between the surface normal (green line) and the c-axis (black dotted line) is θ, in here named as tilting angle. The tilting angle varies between 0° and 90°. Following this geometrical representation, θ is 0° for the basal plane and 90° for the prismatic planes.

The axis in the plane of the basal face which the sample tilts about when changing theta is shown in black (Fig. 4.8a). Perpendicular to this, and also in the basal plane, is the axis shown in red; this red axis and the a-axis (in blue) form φ, referred as the rock angle. Figure 4.8(b), a top view from $\{0001\}$ plane, explains the rock angle further.

The plane perpendicular to the a-axis is a secondary prism face, $[\bar{2}110]$. As shown in figure

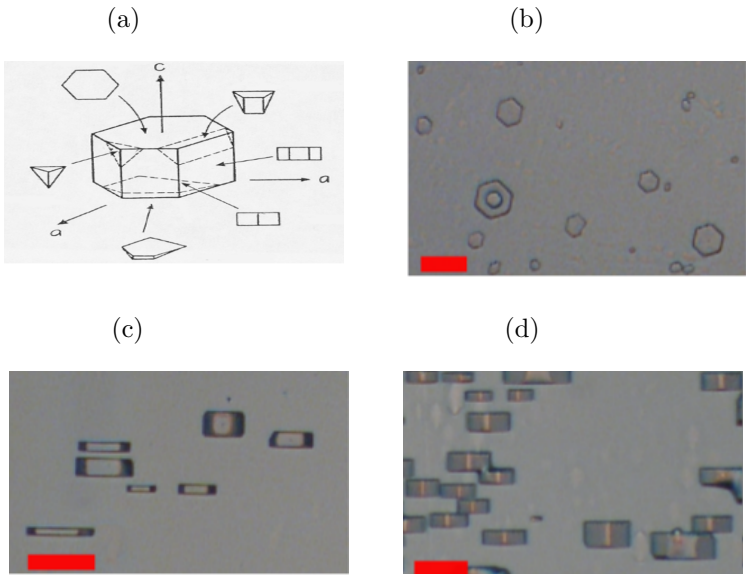

Figure 4.7: (a) Different pit shapes that are created with Formvar etching, from ref [17]. (b) Basal plane, hexagon shape (c) primary prism plane, flat table shape, (d) secondary prism face, house roof shape. The red bars represent 50 μm.

4.8(b), the plane $\pm 30°$ from the secondary prism face is a primary prism face, $[1\bar{1}00]$ [96].

Experimentally, we firstly obtain a basal face by tilting θ to zero. Secondly, after the c-axis is perpendicular to the surface, we obtain the prismatic planes; for that we rock φ or φ+30° to zero for secondary or primary faces, respectively. Subsequently, we tilt θ 90°, in order to expose the prism plane.

Of course, X-ray methods have more accuracy than thermal etching ones. However, the Formvar technique is simpler and easer to used to determine the crystal orientation. Furthermore, when we compare both methods (see appendix), the data show only small errors in the lattice orientation.

4.3 Sample preparation for SFG measurements

Once we have crystallographically oriented ice, we can use it for SFG experiments (see chapter 2). The sample is cut into a circular shape when looking at the isotropic basal plane. For prismatic planes the sample is cut into the shape shown in figure 4.8(b), since in this case the sample is optically anisotropic and the specific orientation must be known. For cutting the sample, a circular cutter is used. Secondly, the ice is mounted in the aluminium sample cell at 276 K. To place it in the centre, a Teflon guide device can be used. The sample cell with the ice is kept in the freezer at 253 K for 20 min to assure that the ice is frozen strongly in the cell.

Figure 4.9 shows the latest version of our aluminium sample cell. The bottom is made of brass with groves, which allows the cell to moves smoothly on a cold copper surface. Previous sample cells versions were smaller and made of stainless steel. We use now aluminium as it a lighter material with an order of magnitude higher thermal conductivity.

The aluminium cell can be mechanically attached to a custom made microtome holder, where the ice surface is smoothed. This attachment places the cell parallel to the microtome knife. We use a new blade heated to 270 K (diamond coated from C.L Sturkey) for each sample, the thickness of our samples is 3.5 mm. Finally, the sample cell is closed with a CaF_2 window to avoid ice

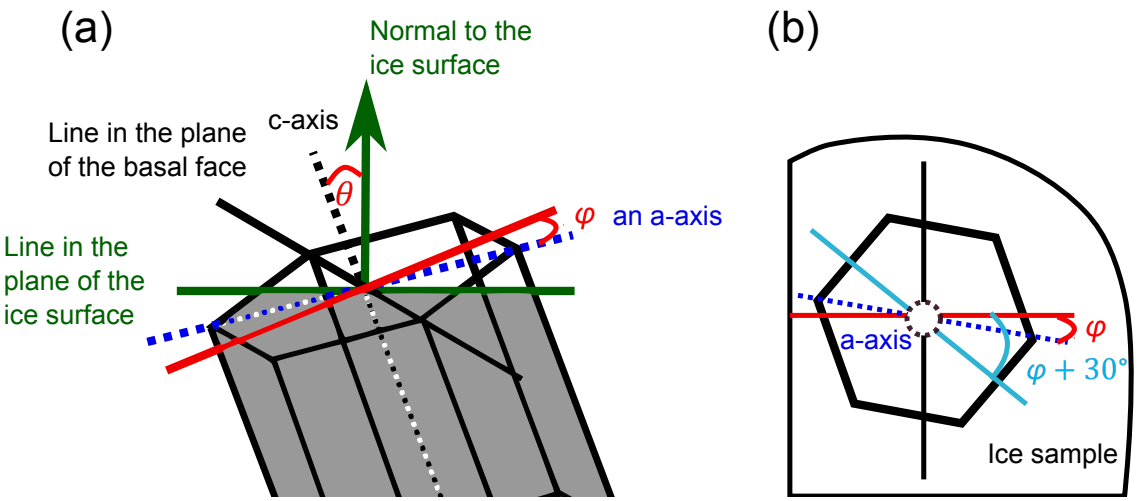

Figure 4.8: (a) An inverted replica of a Formvar etching pit, the white part of the hexagon is a cartoon of a positive pit generated on the ice surface and the grey part is the sample bulk and a (b) basal oriented {0001} ice sample seen from above, the hexagon represents an exaggerated Formvar pit. The dot in the middle shows the c-axis perpendicular to the ice sample plane, see text for details. Based on refs. [96, 105, 106].

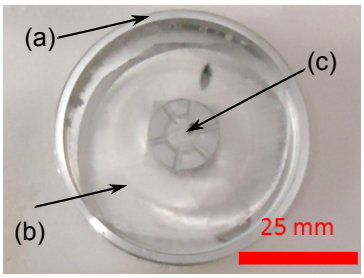

Figure 4.9: Ice on the aluminium sample cell (a) Sample cell, (b) crystalline ice slide, (c) cold aluminium pin.

evaporation and left to anneal overnight at 253 K [107]. The striations left by the microtome blade are slowly smoothed by thermal etching.

During the sum frequency generation (SFG) measurements, the sample is kept at low temperatures; a copper plate was cooled down to 218 K with a Peltier element. The heat generated by the Peltier is transferred into silanol oil (Dow Syltherm XLT) cycling through two chillers (Lauda Pro-Line RP845 and Danfoss LCHC 008 with custom evaporator coil) set at 255 K. Additionally, the sample is constantly moving to avoid the ice melting due to the infrared light. Humidity is reduced by constantly flushing with dry nitrogen gas, to avoid water condensation on the CaF_2 window and optics.

Furthermore, it is know that hydrocarbons alter the physical-chemical characteristics of the ice. For example, premelting is enhanced by contamination [108]. Thus, we clean all the components with acetone, ethanol and abundant water for each new ice sample. Occasionally, we clean the Teflon components with piranha solution (a mixture of H_2SO_4 and H_2O_2).

4.4 Appendix

4.4.1 X-ray characterization

The structure and orientation of single crystal ice samples were studied by x-ray diffraction. The measurements in this section were done by Prof. Markus Mezger.

X-rays from a Cu Kα (wavelength 1.54 Å) rotating anode source (Rigaku MicroMax 007 X-ray generator) with curved multilayer optics (Osmic Confocal Max-Flux) are collimated by a set of two 4-jaw apertures. Measurements were conducted on a self-constructed 6-circle diffractometer using the standard angle convention [109]. Ice crystals were mounted inside a sealed sample cell on a copper disc and cooled to ∼253 K. Full access to the sample surface by the incident and scattered X-ray beam is provided by a transparent Kapton dome (foil thickness 25 μm). X-rays are detected at a sample-detector distance of 57 cm by a microstrip solid-state detector (Dectris Mythen).

To determine the surface orientation of an ice sample previously oriented by the Formvar etch technique (Fig. 4.7), the positions of multiple Bragg reflections were recorded [26, 110]. Misscuts and crystal orientations determined by X-ray diffraction with respect to the alignment using the Formvar etch technique are summarized in Table 4.1.

Table 4.1: Discrepancies in orientation of selected ice samples (Fig. 4.7) oriented by Formvar etching

sample	$\Delta\omega$	$\Delta\chi$	$\Delta\varphi$
basal	1.0°	0.9°	5.0°
primary prism	3.9°	2.9°	4.6°
secondary prism	5.6°	0.2°	0.4°

The angles ω, χ and φ are illustrated in figure 4.10a, the figure shows the diffractometer (Fig. 4.10b and c)used to measure the ice samples (inside the yellow chamber, Fig. 4.10d) . The Δ is the difference between the values estimated by Formvar etching and those measured by X-ray. An ideally oriented sample should have a $\Delta = 0$, the table shows that the error is less than 6 °.

4.4.2 Universal Stage

This subsection explains how to determine if the c-axis of ice is oriented either in the north-south or east-west plane when looking at the crystal from the prismatic plane.

The analyzer and the polarizer should be orthogonal two each other. The polarizer is oriented to transmit the light that is transmitted in a north-south direction and the analyzer in an east-west direction.

The four axis of rotation of the Universal stage are, Fig.4.6:

- A1= Inner vertical axis.
- A2= North-south axis.
- A4= East-west axis.
- A5= Outer vertical axis.

Under two crossed polarizers, by rotating A1, the brightness of the prismatic faces changes from bright to dark at four angles (two directions), as the projection of the c-axis on the horizontal plane can be either parallel with the polarizer or the analyzer. The A2 and A4 angles help us distinguish if the c-axis is either on the N-S or E-W plane. Formvar etching also distinguishes the position of the c-axis. For example, the surface shown in figure 4.7(c) has its optical axis in the

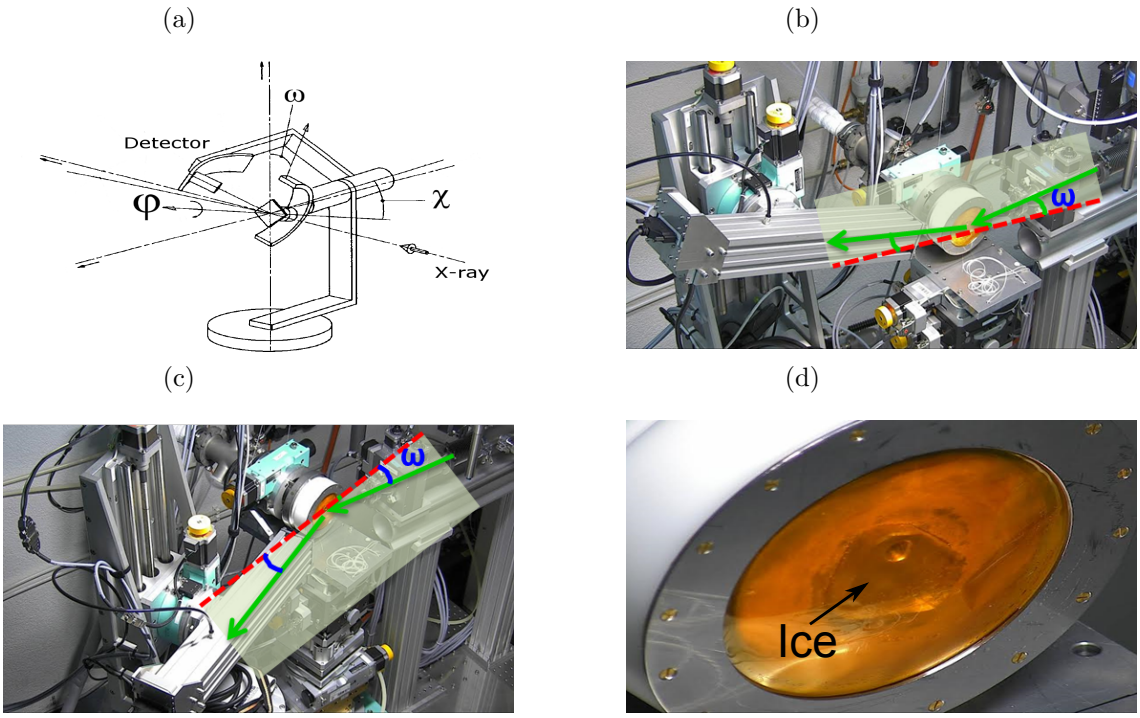

Figure 4.10: (a) A schematic drawing of the circle diffractometer with all angles are in the first quadrant, adapted from [109]. For the X-ray experiments, the detector can be moved in the vertical (b) or horizontal (c) plane. The ice sample (d) is inside a sealed sample cell.

N-S direction. However, it is not possible to measure the same sample that was etched due to hydrocarbon contamination, thus is advisable to double check the c-axis orientation of the slice for subsequent SFG measurement with the universal stage.

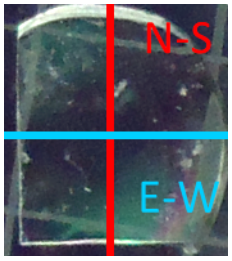

Figure 4.11: C-axis orientation for a prismatic ice surface.

The following routine is used only to determine if the c-axis is in the N-S or E-W direction [100]:

1. Set the rotations to zero.
2. Place the sample with an specific shape (Fig. 4.11) on the centre of the apparatus.
3. With A1 rotate the sample and find the four angles where the ice goes from bright to dark, know as angles of extinction.

4. Choose one of those A1 angles.

5. Test the extinction by rotating A2. If the sample departs from extension, return A2 to zero. Rotate A1 90° to the other extinction position, and rotate A2 again to see if the sample remains dark. If in this position the ice stays dark, the east-west plane contains the optical axis. The opposite happens when the optical axis is in the north-south plane.

Occasionally, the ice is extinguished for both A1 angles when rotating A2 (step 5). The following additional steps are then necessary:

1. With the sample at one of the two extinctions angles, rotate A4 by an arbitrary amount.

2. Then move A2. If the grain remains dark, the c-axis lies in the N-S plane; if extinction is lost, the axis is in the E-W plane.

3. Rotate A1 90° and repeat steps 1 and 2.

One can choose how to crystallographically orient the ice, but then one must remember to place the slice with the same orientation in the sample cell.

Moreover, the measured angles differ from the true ones, mainly to the differences between the refractive indices of air and ice. Figure 4.12 shows the corrected angles for prismatic surfaces of ice, for basal substrates see ref [100].

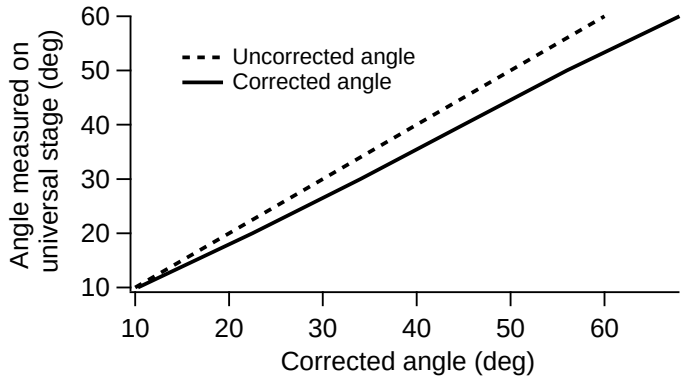

Figure 4.12: Corrected angles for universal stage measurements of prismatic faces of ice. Based on ref. [93].

Chapter 5

Surface melting of crystalline ice

"*Ice is melting because of our consumerist, nationalist and short-sighted society.*"

Sánchez, 2017

As early as 1859, Faraday proposed the existence of a liquid-like layer at ice surfaces [111, 112]. This surface-induced ice melting represents one of the most prominent examples of an interface-induced premelting phase transition [5,113]. During the last decades, the so-called quasi-liquid layer (QLL) at the ice-air interface, wetting the crystalline bulk phase, has been studied by theory [114], computer simulations [35, 115, 116] and various experimental techniques [117–125]. Despite the general agreement on the presence of a QLL below the bulk freezing point, the temperature-dependent thickness of the QLL has remained controversial. The experimentally reported onset temperature for QLL formation varies between 200 K and 271 K. Moreover, most experimental work shows that with increasing temperature, the QLL thickness gradually and continuously increases from the onset temperature up to the bulk melting point, with reported thicknesses varying from 2 nm to over 45 nm at 271 K [5,119–121,123,124,126]. In contrast, early simulations showed that the QLL is formed in a more quantized, bilayer-by-bilayer manner [35].

In this chapter, we provide evidence of layer-by-layer growth of the QLL at the ice-air interface by combining experiments with simulations. We employ surface-specific vibrational sum-frequency generation (SFG) spectroscopy, explained previously in chapter 2. Our experimental data are corroborated by spectral calculations based on molecular dynamics (MD) simulations, see section 5.7.1 [26].

SFG spectroscopy (see chapter 2) has been used for unveiling the molecular conformation of the ice/air interface. Shen and coworkers [127, 128] focused on the frequency region of the non-hydrogen bonded OH stretch mode (3600-3800 cm^{-1}) in the temperature range from 173 K to 271 K. By probing these OH groups, sticking into the air, they concluded that surface disordering appears at temperatures as low as 200 K. The Shultz group studied the hydrogen bonded OH stretch frequency region (3200-3600 cm^{-1}) of various basal and prism faces of the ice/air interface at temperatures around 100 K [31, 32, 129, 130].

To study surface melting, we focus here on the hydrogen bonded part of the spectrum at temperatures between 235 and 273 K where, according to most reports [126], surface melting takes place. As the frequency of the OH stretch vibration depends on the hydrogen bond strength with neighbouring molecules [131, 132], the SFG spectrum contains information on the intermolecular interactions between water molecules at the surface. This allows us to determine the hydrogen bond strength at the interface and to obtain information about the QLL.

5.1 Ice sample

We explore the surface melting of the basal and secondary prism planes of hexagonal ice, see chapter 1. The secondary prism face of ice is s-oriented, meaning that it is oriented with the c-axis perpendicular to the plane formed by the incident laser light and the surface normal. [32, 103].

The single crystalline samples are prepared following the seed extraction from the melt technique and oriented with the universal stage and Formvar etching, see chapter 4. Figure 5.1 shows the stainless steel sample cell and the copper plate that we used for the experiments of this chapter. This cell was cooled down to 223 K with a Peltier element. The heat generated by the Peltier was transferred into a water/polyglycol mixture cycling through an open bath chiller set at 255 K. After reaching the desired temperature, the sample was kept for at least 30 min before starting a measurement to achieve thermal equilibrium. The cell was constantly moved in a circular motion on the copper plate by a motorized pivot-crank mechanism at a speed of ∼2.8 cm per second.

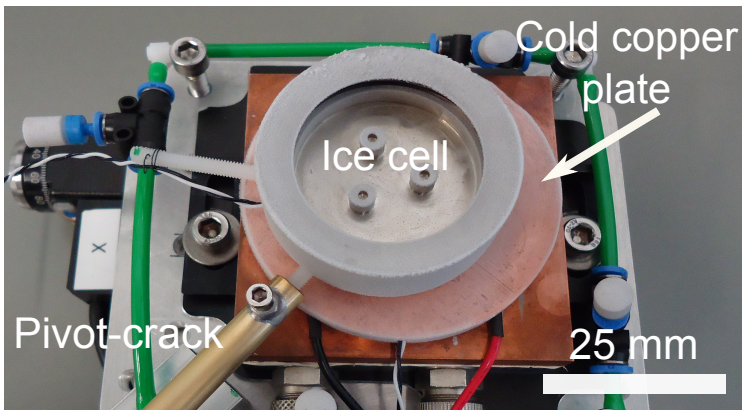

Figure 5.1: Stainless ice sample cell on a cold copper plate.

5.2 SFG of ice-air interface

One of the biggest challenges is to avoid the ice sample melting. The ice can melt due to the absorption of the infrared probe light when we probe in the hydrogen bonded region. In this case, a dramatic decrease of the signal intensity is observed when the sample is illuminated. To avoid melting, the sample was moved continuously, and for the bonded OH region the repetition rate of the infrared pulse was reduced to 250 Hz, so that every laser shot appears on a fresh spot. As the absorption is less at higher infrared frequency, a repetition rate of 1 kHz could be used for the SFG measurement in the free OH stretch frequency range (3700 cm^{-1}). Figure 5.2 shows that following this procedure, the SFG spectrum at 235 K in the hydrogen bonded region is stable over at least 6 hours: the spectrum after six hours of continuous irradiation is identical to the initial spectrum. Moreover, a repetition rate of 250 and 164 Hz gave identical results. The stability of the signal shown in figure 5.2 proves that the sample is not damaged by the laser. Moreover, the spectra in figure 5.2 show no CH stretch vibration; the CH stretch modes of hydrocarbon contamination are normally observed in the frequency range between 2800 cm^{-1} and 3000 cm^{-1}. The absence of a signal in this frequency range indicates that the sample has no contamination or, at least contamination below the detection limit.

The energy of the IR pulses around 3000 $cm^{-1}$and 3600 cm^{-1} at the sample was 3 μJ and 1.5 μJ, respectively. The visible probe pulse energy was 20 μJ. The ice spectra were collected

under SSP polarization (s-SFG, s-visible, p-IR) and normalized to a non-resonant signal from a gold coated (∼100 nm thick film) silicon wafer. The 380 μm thick gold coated silicon wafer (0.25 cm^2) was placed on top of the ice surface outside the ice area probed with SFG.

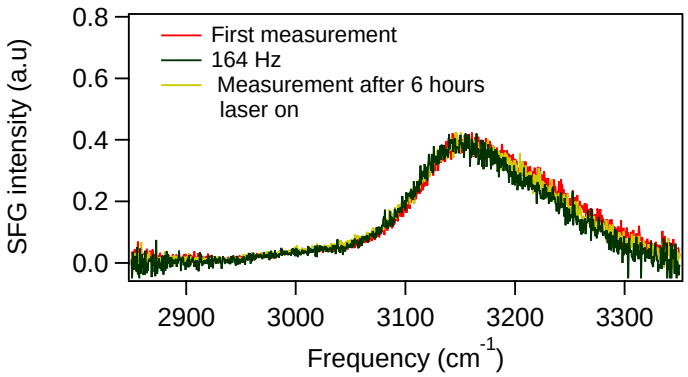

Figure 5.2: Laser influence on an ice sample. SFG spectra in the hydrogen bonded OH stretch region of the basal face at 235 K at different irradiation conditions. The SFG signal is stable in time and has similar intensity and spectral shape at 164 Hz.

5.3 Symmetric stretch hydrogen bonded region

Figure 5.3 displays the SFG spectra from the ice surface at different temperatures. An intense peak slightly below 3200 cm^{-1} is observed, which agrees with previous SFG measurements [127]. As the temperature increases from 235 to 264 K, the SFG intensity decreases by a factor of 5. Wei et al. [127] have previously reported a similar, albeit much weaker, intensity decrease by a factor 3 with increasing temperature from 173 to 272 K. In contrast, a strong temperature dependence has been reported by the Shultz group they observed an intensity decrease by approx. a factor of 6 in the temperature range from 113 to 178 K [31]. The decrease in the ice SFG intensity with increasing temperature has previously been interpreted as a decrease in the (bulk-allowed) SFG quadrupole contribution [32,133,134] and a loss in the tetrahedral hydrogen bond structure leading to a decrease in the intermolecular coupling [135, 136].

Besides the intensity variation *I(ω)*, figure 5.3a also shows an apparent shift of the hydrogen bonded OH stretch band to higher frequency ω with increasing temperature. To quantify the frequency shift as function of temperature, the numerically determined first moment of the spectral distribution $\int \omega I_\omega d\omega / \int I_\omega d\omega$ of the hydrogen bonded OH peak has been plotted in figure 5.3b. Surprisingly, the first moment of the spectral distribution exhibits not a gradual shift with increasing temperature, but rather a steep increase from ∼3185 to ∼3210 cm^{-1} around 257 K. A sigmoidal fit gives the transition temperature of 256.9 ± 0.3 K. As a higher frequency of the OH stretch mode of water indicates a weakening of the hydrogen bond strength [131,132], the sigmoidal shape may be interpreted as an abrupt weakening of the hydrogen bonds in the top layers of the ice sample.

Interestingly, the spectra from 235 to 269 K can be very well described by a linear combination of the two spectra at 235 and 269 K, respectively. The relative amplitudes of the 235 and 269 K spectra at the intermediate temperatures inferred from the fits (red curves in 5.3a) are plotted in figure. 5.3c. Only the amplitude of the 235 and 269 K spectral contribution are free parameters. The contribution of the 235 K spectrum decreases linearly with increasing temperature, whereas

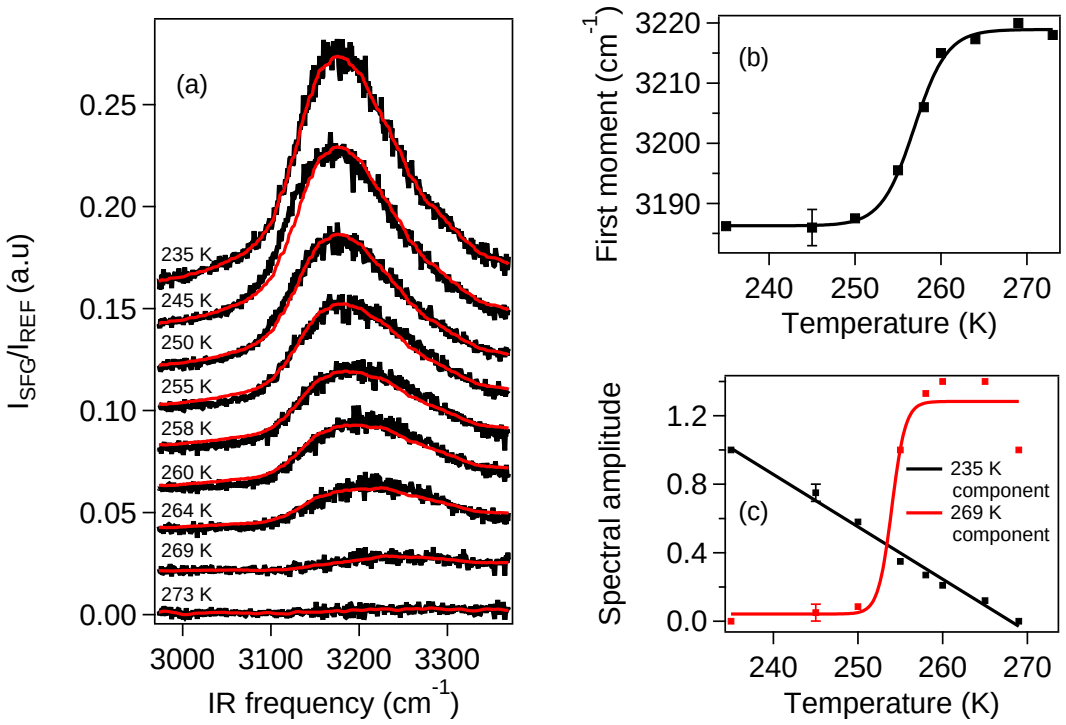

Figure 5.3: Ice/quasi-liquid/air interface of the basal face studied with Sum Frequency Generation (SFG). (a) SFG Spectra under SSP polarization (S, SFG; S, visible; P, IR) between temperatures of 235 and 273 K for the basal face of ice. The black lines are the experimental results; the red ones are results of the two component fit (see text for details). The data is offset for clarity. (b) First moment of the spectral intensities shown at different temperatures for the basal over up to four different experiments. The lines are sigmoidal fits through the data points. (c) Contribution of the 235 and 269 K spectra to the SFG spectra at intermediate temperatures, for the basal face. Typical error bars based on reproducibility from experiment to experiment are given in the graph.

the contribution of the 269 K spectrum has a stepwise increase from zero to a finite value around 254 K.

Figure 5.4 shows the SFG results of the ice/quasi-liquid/air interface of the secondary prim face. The intensity decreases as the temperature increases, as is observed for the basal plane (Fig. 5.4a). We also observe a shift to higher frequency with increasing temperature (Fig. 5.4b), albeit this observed shift is smaller than that for the basal face (Fig. 5.3b). A sigmoidal fit through the spectral first moment results in a transition temperature at 258.6 $\pm$ 0.1 K. A possible explanation for the smaller step may be that, for the secondary prism face, single layers of ice melt, as the layer-layer interaction does not give rise to bilayer behaviour for this crystal cut. Moreover, after fitting the data with a linear combination of the spectrum at 235 K and the one at 269 K, the contribution of the 235 K spectrum linearly decreases with increasing temperature, whereas the contribution from the 269 K spectrum increases with increasing temperature in a nonlinear manner. The slope of the spectral amplitude vs temperature changes at 255 K (Fig. 5.4c).

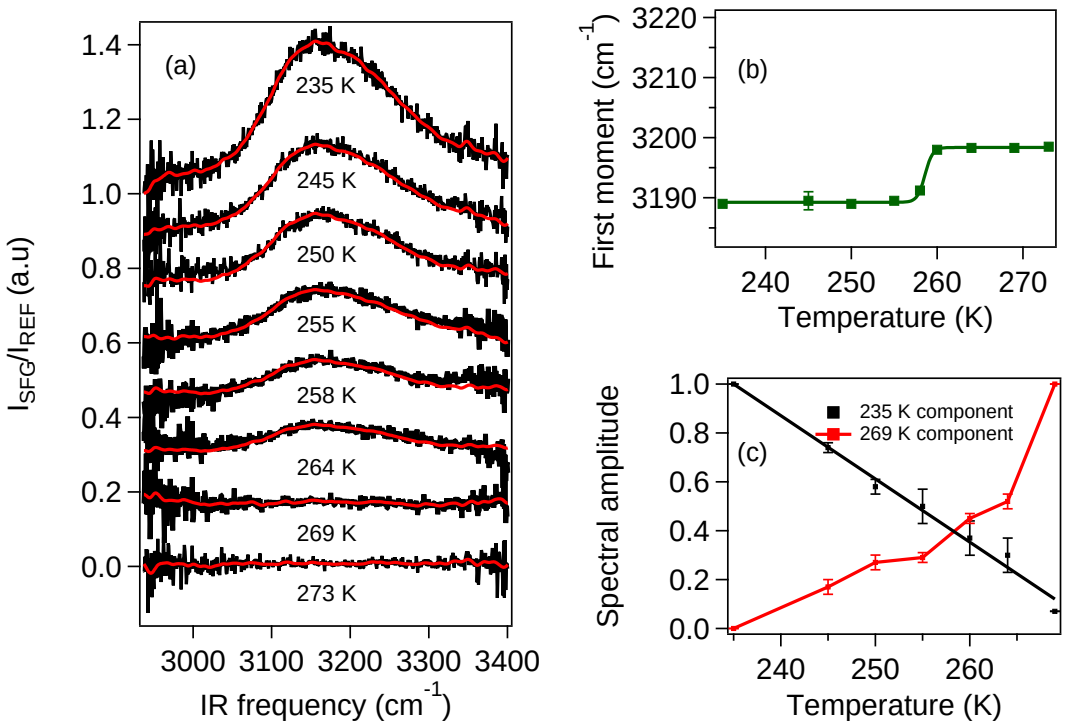

Figure 5.4: Ice/quasi-liquid/air interface of the secondary prism planes studied with Sum Frequency Generation (SFG). (a) SFG Spectra under SSP polarization (S, SFG; S, visible; P, IR) between temperatures of 235 and 273 K for the prismatic face of ice. The black lines are the experimental results; the red ones are results of the two component fit. The data is offset for clarity. (b) First moment of the spectral intensities shown at different temperatures for the secondary prism face averaged over up to four different experiments. The lines are sigmoidal fits through the data points. (c) Contribution of the 235 and 269 K spectra to the SFG spectra at intermediate temperatures, for the secondary prism face.

5.4 Antisymmetric OH stretching and dangling OH modes

Besides the symmetrical hydrogen bonded OH stretch region, other vibrational modes also contain important information about the nature of the surface, for example, the vibrational response of the antisymmetric stretch OH bonds (ASB OH) of the three-fold coordinated DDA and the four-fold coordinated water molecules, see chapter 1, in addition to the dangling OH bond. The band centred at ~ 3500 cm^{-1} has been assigned to the antisymmetric stretch OH mode of the DDAA [33]. The band at $\sim$ 3580-3600 cm^{-1} is the antisymmetric stretch OH of the DDA water molecules [137]. The vibrational frequency of the dangling OH is rather high, around 3700 cm^{-1}, as the OH group does not form a hydrogen bond. Figure 5.5 shows the SFG spectra in the frequency range from 3350 to 3760 cm^{-1} for various temperatures. The peak amplitudes can be obtained by calculating the peak areas between 3420-3550 cm^{-1} and 3650-3760 cm^{-1}, for the ASB OH and the dangling OH, respectively. To obtain the area under the ASB OH signal the tail of the signal at 3150 cm^{-1} has to be subtracted. For this, we fit a straight line to the data between 3350 and 3600 cm^{-1}, but excluded the range from 3420 to 3550 cm^{-1}.

As apparent from the data in figure 5.5 and reported previously for the air-liquid water interface [138], the ASB OH amplitude decreases as the temperature increases. The area under the

3700 cm^{-1} band is similar for both ice/QLL/air interface at 273 K and liquid water/air interface at ∼298 K. The amplitude of the 3700 cm^{-1} mode shows only a weak, continuous temperature dependence, indicating that the outermost surface structure does not change dramatically, in agreement with previous results by Shen et al. [128]. The secondary prism face shows the same trend.

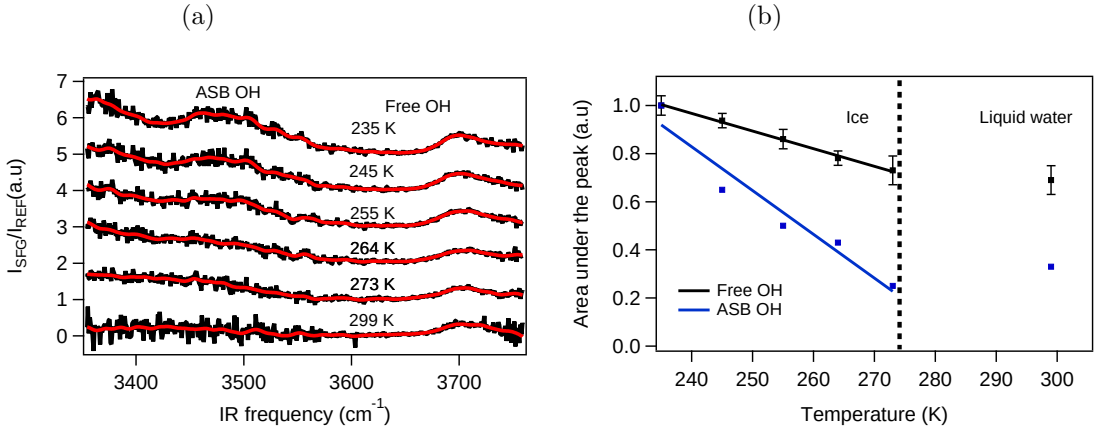

Figure 5.5: Asymmetric stretch bonded OH (ASB-OH) and dangling OH (free-OH) regions of ice and liquid water (299 K). (a) SFG spectra as function of temperature, data is offset for clarity. The lines are to guide the eye. (b) Normalized area of the ASB-OH (in blue) and the free-OH (in black) bands. Data is offset for clarity.

5.5 Surface melting of ice

Both experimentally measured and calculated (sec. 5.7.1) spectra show an abrupt blue shift when heating to 257 K, indicating a weaker hydrogen bond environment, consistent with a transition to a state with more liquid-like character. The theoretical presented in sec.5.7.1 results explain the experimentally observed sudden change in the SFG spectra, and thus the interfacial water organization around 257 K, in terms of a transition from one to two molten bilayers, sec. 5.7.1. Because of the discreteness of the ice lattice, it is reasonable that the variation of the QLL with increasing temperature occurs in a discrete manner, i.e. in a bilayer-by-bilayer fashion. "Patches" of molten bilayers in large crystalline samples would be thermodynamically unfavourable, as there would be an energetic penalty from the liquid/solid line tension.

Interestingly, such a transition seems to have been observed as well by photoelectron spectroscopy experiments; the inferred thickness seemed to suddenly change between 248 and 258 K, but was not investigated in more detail [108]. Layer by layer melting has previously been observed for other systems [139, 140]. In particular, for crystals with directional bonds, tendencies for layering are pronounced [141]. For most of these systems, blocked surface melting, i.e. a finite thickness of the QLL up to the bulk melting point, has been observed [139]. In contrast, for ice with its tetrahedral H-bonded structure, we observe a sharp transition from one to two layers, i.e. an indication for stepwise melting, whereas for temperatures close the melting point, a divergent increase of the QLL thickness has been reported [108, 120–122]. Therefore, water seems to be one of the few cases showing stepwise melting at low temperature and diverging melting at higher temperature.

From our experimental SFG data alone, we cannot strictly exclude that the observed transition represents the onset of surface melting, i.e. solid ice below 257 K and a QLL with constant or increasing thickness above 257 K, instead transitioning from one QLL to two QLLs. Indeed, using

gracing incidence X-ray diffraction, Lied et al. found onset temperatures for bulk melting of 259.5 K for the basal and 260.5 K for nonbasal surfaces. While the transition temperatures are slightly lower in our experiments, we find the same trend, i.e. a lower transition temperature, for the basal compared to the prism face [121, 124]. However, this alternative interpretation is not only at odds with the simulations presented above, it is also in seeming contradiction with the experimental observation that the response from the dangling OH groups varies modestly and continuously over our temperature window. It is unlikely that the dangling OH groups of solid ice and those of water in the QLL have the same exact vibrational frequency. Moreover, one would expect not only a frequency shift, but also an intensity change, as the fast reorientational motion that is possible for the free dangling OH groups [142] in the QLL is expected to significantly affect the vibrational response. Indeed, previous SFG studies have witnessed a change in the order parameter of the dangling OH at 200 K, which is a measure of the disorder of the surface. Below 200 K the order parameter is constant, while above 200 K it decreases with increasing temperature [128]. The picture that thus emerges is that the first bilayer melts at temperatures as low as 200 K, and that surface melting proceeds from 257 K onwards. While our results indicate that a single additional bilayer melts at this temperature, we cannot exclude a continuously increasing thickness of the QLL above this temperature.

The spectral changes associated with the transition provide information about the change in the local environment of the water molecules. Comparing the spectral response at 235 K and that at 269 K (Fig. 5.3), the former has a strong contribution from ice and likely a (small) contribution from the very thin QLL present already at 235 K. The high temperature spectrum has a larger contribution of the QLL as this spectrum originates from a state with at least two molten bilayers, and contains a smaller contribution from the ice, as the ice signal decreases in amplitude with increasing temperature. The analysis of the temperature dependent spectra reveals that the contribution of the 235 K spectrum goes down with increasing temperature as the tetrahedral hydrogen bond structure in ice gets more disordered. As the number of water layers abruptly increases at 257 K, so does the central frequency of the spectral response (Fig. 5.3a). The shift to higher frequency of the 269 K spectrum compared to the 235 K spectrum indicates a weakening of the hydrogen bonds for the QLL compared to ice. For the free OH groups, the small gradual decrease observed both in the experimental and the calculated SFG spectra could indicate a small decrease in ordered free OH groups with increasing temperature and/or an increased rotational mobility of these groups.

As shown in figure 5.3b stepwise change in the SFG spectrum observed for the basal face is also observed for the secondary prism face, albeit with a smaller, less pronounced frequency change in the experimental spectra. Also, the transition in the contribution of the 269 K spectrum after fitting the data with a linear combination of the spectra at low and high temperatures is less pronounced (Fig. 5.4). A possible explanation for the smaller step may be that, for the secondary prism face, single layers of ice melt, as the layer-layer interaction does not give rise to bilayer behaviour for this crystal cut.

While it is clear that, as the temperature increases, the SFG response shifts to higher frequency, a key question is about the nature of the QLL: is it spectroscopically discernible from liquid water? To answer this question, we compare in figure 5.6 the SFG spectra from supercooled water and ice, both recorded at 269 K. The supercooled water spectrum looks similar to water spectra above zero degrees, indicating little difference between the surfaces of supercooled water and water at ambient temperatures, in contrast to bulk measurements for more strongly supercooled water [13].

For the ice surface at 269 K we expect to probe both the ice-QLL and QLL-water interfaces. The response differs substantially from that of the supercooled water-air interface. The two spectra look very similar around 3200 cm^{-1} (the small difference at low frequency can at least in part be attributed to a higher relative contribution of NR signal at 269 K than at 243 K), but between 3300 and 3500 cm^{-1} the normalized intensity in the ice spectrum is much lower than that of

the normalized intensity of the supercooled water. The ice spectrum at 269 K resembles more the ice spectrum at 243 K than the supercooled water spectrum. This comparison could suggests that at 269 K the ice-QLL interface still significantly contributes to the observed SFG spectrum and/or that the QLL has a different nature than supercooled water in the sense that it has stronger hydrogen bonds, possibly due to templating from the underlying crystalline ice order.

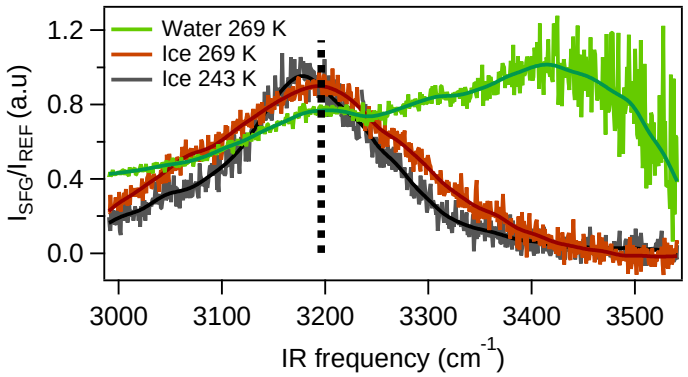

Figure 5.6: Normalized SFG spectra of supercooled liquid water (green) and ice, both at 269 K (red), and ice at 243 K (grey). The lines are to guide the eye. The supercooled water and ice spectra at 269 K are acquired for 60 and 140 minutes, respectively. The ice spectra were measured by Jenée D. Cyran.

5.6 Summary

Both in SFG experiments and in MD simulations, a stepwise blue shift in the spectra of the ice-air interface around 257 K has been observed. This feature that indicates weakening of the hydrogen bonds marks the transition to a state in which the surface layers entail a more liquid character. The relatively small temperature variation of the dangling OH in the temperature range from 235 to 273 K suggests that the outermost layer is not changing its nature over this temperature range. Therefore, we conclude that already at 235 K a quasi-liquid layer is present on ice. This quasi-liquid water layer suddenly increases its thickness around 257 K in a discrete bilayer-by-bilayer manner. A comparison of the SFG response of ice at 270 K with that of supercooled water at the same temperature indicates that the QLL is more similar to ice than to supercooled liquid water: the QLL seems to have stronger hydrogen bonds than liquid water. This information is crucial for understanding both the surface chemistry of ice under near-freezing conditions [143–145] and the melting mechanism of the ice surface which has important geophysical implications on the macroscopic scale of our planet, for instance in the case of glacier sliding [6].

5.7 Appendix

5.7.1 Molecular dynamics

To connect the experimental results to a molecular level picture, Tanja Kling, Mara N. Jochum and Davide Donadio performed MD simulations using the TIP4P/Ice model, showing the melting bulk point at 272.2 K [146]. Figure 5.7 shows the density profiles for different temperatures for the basal and secondary prism faces. The double peaks for basal face and a single peak for prism face manifest the bilayer structure for the basal face and the single layer structure for

the secondary prism face, respectively. The observed density profiles resemble those reported in previous works [35, 116]. At 230 K, the density profile for the slab cleaved along the basal plane displays a double peak structure for all bilayers, except the outermost bilayer, indicating that the outermost layer is already disordered at this temperature. Increasing the temperature from 230 K to 270 K, the double peak fine-structure in the second layer suddenly disappears between 260 and 270 K. Density profiles indicate that the basal plane melts in a bilayer-by-bilayer fashion, in agreement with the findings of Kroes [35].The density profiles of the slab exposing the secondary prism face show that melting occurs gradually, as the difference between density peaks and valleys in the surface layers decreases progressively.

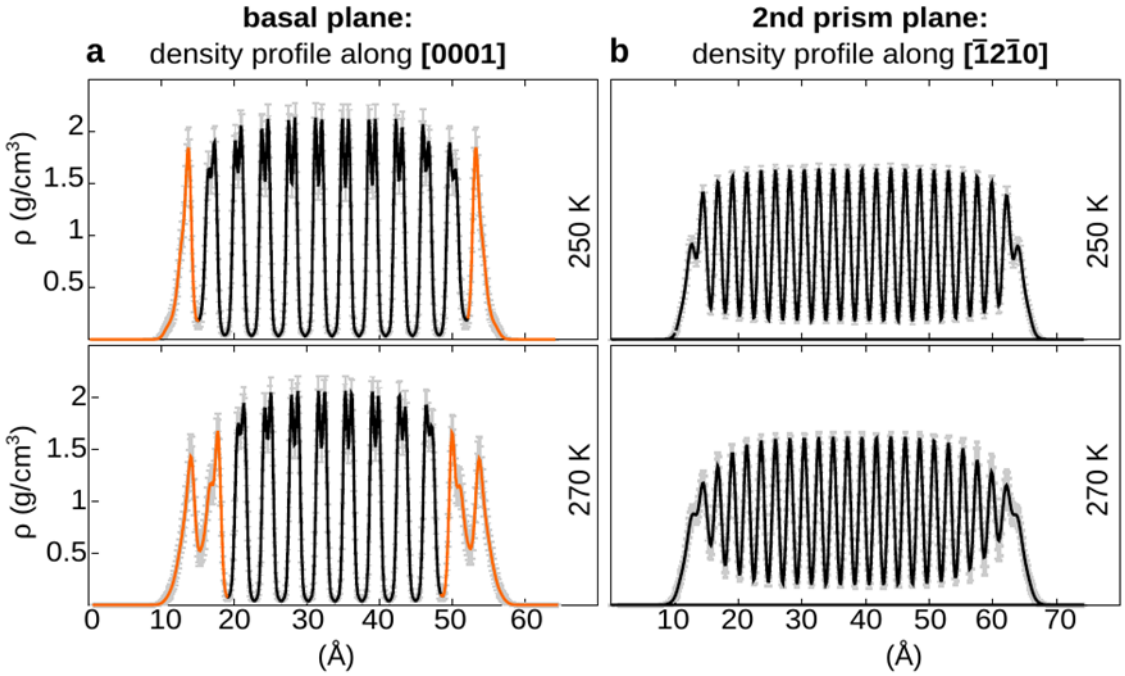

Figure 5.7: Density profiles obtained with the TIP4P/ice model for (a) the basal and (b) secondary prism plane of hexagonal ice, illustrating the bilayer and monolayer structure, respectively. For the basal plane at 250 K only the outer bilayer has lost its characteristic density profile, while at 270 K the outer two bilayers are molten as indicated by the orange colour. The density profile for the secondary prism face, with equal distance between the layers, changes gradually, as indicated by a gradual transition of the envelope from a rectangular to an elliptical shape.

Subsequently, Tatsuya Ishiyama and Akihiro Morita calculated SFG spectra to connect the molecular level changes to the spectrum. The present simulation of SFG spectra was carried out with the classical CRK model of water [147]. Figure 5.8 shows the calculated ssp-polarized SFG intensity spectra of the basal face of ice as a function of temperature in the hydrogen bonded and the dangling OH region of the spectrum. Similar to the experiments, with increasing temperature, the peak intensity decreases and the peak maximum appears to shift toward higher frequencies. As evident from figure 5.8b, a sigmoidal fit through the peak maximum of hydrogen bonded OH stretch mode as function of temperature results in an inflection point at 252 $\pm$ 1 K. This temperature is slightly lower than the temperature observed in the density profiles as described above. However, these simulations were performed using the polarizable and flexible-body CRK water model instead of the T1P4P/ice. Also in agreement with the experiments, the dangling OH band at about 3700

cm^{-1} shows a moderate reduction with increasing temperature (Fig. 5.8c).

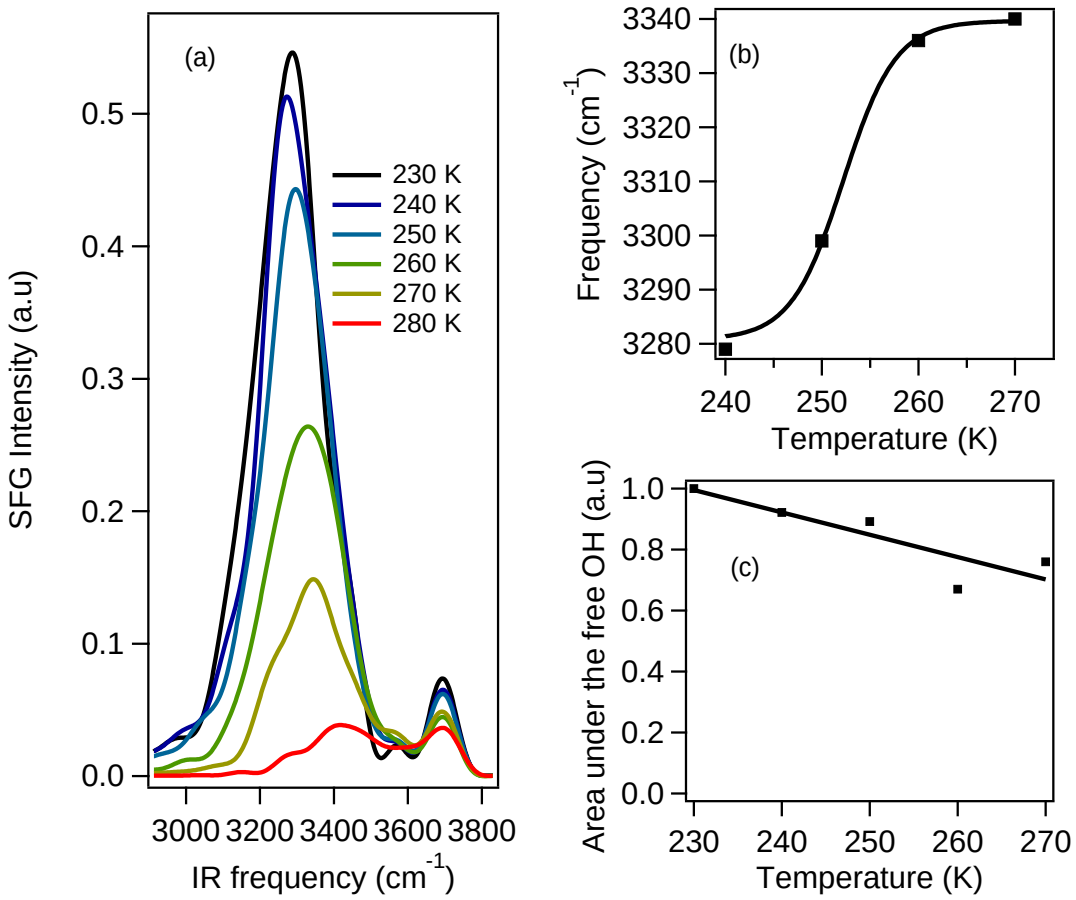

Figure 5.8: Calculated SFG spectra (a) Calculated ssp polarized SFG spectra of the basal face of ice at different temperatures. (b) Frequency at the maximum SFG intensity of the hydrogen bonded peak as function of temperature (squares) with a sigmoidal fit. (c) Spectral area under the free OH peak ($\sim$ 3700cm^{-1}) vs. temperature.

5.7.2 Surface melting general theory

The molecules at the surfaces are less coordinated than those within the interior of the crystals, thus surfaces usually exhibit lower thermal stability than bulk. Indeed, free surfaces of solids can be heterogeneous nucleation sites of melts, allowing the crystal surface to melt at temperatures below the bulk melting point (T_B) [140]. Before the bulk melting point, a disordered surface region is formed on the crystal interface, i.e. a QLL [148], and as the temperature approaches T_B the thickness of this QLL usually increases. Moreover, the surface melting is crystal face dependent [149]. For instance, open (110) surfaces of face centred cubic crystals exhibit complete surface premelting, close-packed (111) faces do not melt below T_B, and (100) surfaces of face centred cubic crystals, which is an intermediate packing density between (110) and (111), exhibit incomplete melting, i.e. the thickness of the surface liquid layer remains finite as the system

approaches T_B [140].

Premelting is a general name for this phenomenon which can occur at three interfaces: (1) at the solid and gaseous atmosphere or its vapour, (2) at the solid and another solid or liquid, and (3) at the grain-boundary between crystals of the same material [5].

A qualitative explanation of the physical origin of surface melting, is that melting is favoured by defects. The interface can be seen as a big defect from the perfect 3-D crystal lattice. The Lindemann criterion states that the melting starts when the root-mean-square displacement $\sqrt{\langle \Delta^2 \rangle}$ reaches about 15% of the inter particle distance [150]. Also, other kinds of defects can initiate the surface melting, such as dislocations and grain boundaries (GBs) of polycrystalline ice. It has been reported that aluminium surfaces start melting at the GBs followed by dislocations [125, 151, 152].

The thermodynamics of surface melting can be described with a phenomenological continuum model [140,153]. This model is not applicable for very thin QLL. The free energy difference between a dry and a wetted solid is:

$$\Delta F(d) = \rho Q_m d(1 - \frac{T}{T_B}) + \Delta\gamma(d) \tag{5.1}$$

where ρ is the density of the QLL, Q_m the latent heat of melting, T_B the equilibrium melting point of bulk solids, and $\Delta\gamma(d)$ represents the interaction between the solid-liquid and liquid-vapour interfaces as function of the thickness QLL d.

For short-range forces, such as covalent or metallic, the thickness of the layer diverges logarithmically as T approaches T_B, and $\Delta\gamma(d)$ can be expressed as [140]:

$$\Delta\gamma(d) = \Delta\gamma_\infty(1 - e^{(\frac{-d}{\zeta})}) \tag{5.2}$$

where $\Delta\gamma_\infty$ is equivalent to $\gamma_{lv} + \gamma_{sl} - \gamma_{sv}$ (surface tension of the lv liquid- vapour, sl solid-liquid and sv solid-vapour interfaces). ζ is the length on the order of the intermolecular spacing, assumed to be much smaller than d.

For long-range forces, such as Van der Waals interactions in ice, the QLL thickness has a power law temperature dependence, where $\Delta\gamma(d)$ can be explained as:

$$\Delta\gamma(d) = \Delta\gamma_\infty(1 - \zeta^2/d^2) \tag{5.3}$$

As mentioned previously, depending on the crystalline face, due to the molecular packing, the surface may melt differently. Several theories have been developed to explain this experimental observation. The lattice theory, introduced by Trayanov and Tosatti [154], is based on the minimization of the free energy with respect to the density of the atoms. The density and crystalline profiles show an abrupt jump at the interface between the solid and the QLL. Moreover, the phonon theory is another possible explanation where the interface becomes thermally unstable before the bulk [155]. Chernov and Mikheev [156] explained the surface melting of copper and He/H_2 with a layering transitions at low temperatures.

Nowadays, molecular dynamics simulations are extensively used because they take into account the specific characteristic of each crystal. One of the characteristics is, for example, the interaction between the molecules within the crystal.

Chapter 6

Vibrational relaxation dynamics of the ice-air interface

"*But still try, for who knows what is possible...* ''

Faraday, 1870

Water molecules in liquid are constantly in motion, showing fluctuations and reorganization on time scales from femtoseconds to picoseconds [157]. Time resolved vibrational spectroscopy is a useful technique for elucidating the properties and dynamics of water in this sub-picosecond regime.

Ultrafast vibrational spectroscopy has previously been used to analyse the energy relaxation of molecular vibrations in liquid water samples, for example by measuring the OH or OD life-time and the relaxation of isotopic diluted liquid water samples [158]. Moreover, this spectroscopy also has also been used to study the life-time of the OH stretch mode as function of temperature [159–161].

At the interface, the water network has a different structure than that of the bulk: at the water-air interface the molecules are not fully coordinated. Thus, one might expect different vibrational dynamics. Interfacial water dynamics have been studied with time resolved SFG experiments [46, 162–167]. The vibrational relaxation time of the water OH stretch region at the interface increases when the frequency of the excitation pulse is increased from 3100 to 3500 cm^{-1}. This different relaxation times show the heterogeneity of water at the surface [167].

The OH stretch region is very sensitive to the molecular environment. It contains, for example, information on the hydrogen bonding. The study of the solid state water (i.e. ice), where the molecules are organized in a lattice structure, is important for unravelling the properties of the water hydrogen bonds in general [133, 168]. Moreover, the ice surface is a catalytic surface for important atmospheric chemical reactions [143, 169]. For example, the photolysis of ethylbenzene and xylene is catalysed by ice and not by liquid water [170].

Measurements of vibrational dynamics of the ice interface using nonlinear spectroscopy, have not yet been reported, not because of the lack of interest, but because of the experimental challenges. Published experimental vibrational dynamics studies of ice focus on the bulk rather than the surface where most of the chemical reactions take place. Seifert et al. [171] studied the OH stretch band of crystalline HDO with transient hole-burning spectroscopy. The authors observed inhomogeneous broadening, which was attributed to proton disorder. Bakker's group have extensively studied the OH and OD stretch vibrations with two colour IR pump-probe spectroscopy, analysing the temperature and isotopic dependence of the vibrational life-time [160,172–175]. They suggest a relaxation path of the OD stretch mode through a bend-liberation combination mode for HDO crystalline samples. Moreover, Hamm's group have studied hexagonal ice with 2 and 3

dimensional infrared spectroscopy [176–178]. They observed a fast energy dissipation [177].

In this chapter, the molecular dynamics of ice-air interfaces are studied with time resolved SFG experiments (tr-SFG). Ice dynamics are compared with those of liquid water. The ice time resolved experiments were performed in collaboration with Jenée D. Cyran. The data were partially analysed by a code written by Ruth A. Livingstone. The tr-SFG experiments of the water-air interface were performed by Cho-Shuen Hsieh.

6.1 Ice sample

We study the vibrational dynamics of the basal plane of hexagonal ice at 230 K, see chapter 1. Single crystalline circular ice samples (33 mm in diameter) are used during the tr-SFG experiments, see chapter 4.

During the tr-SFG experiments, which typically takes 12 hours, the ice sample is constantly irradiated with an IR pump pulse of 20 μJ and IR probe pulse of 3 μJ. We avoid laser induced sample melting by moving the ice at 10 cm per second using a combination of motorized gears and a pivot-crank mechanism. The cooling copper stage and the moving mechanism are shown in figure 6.1.

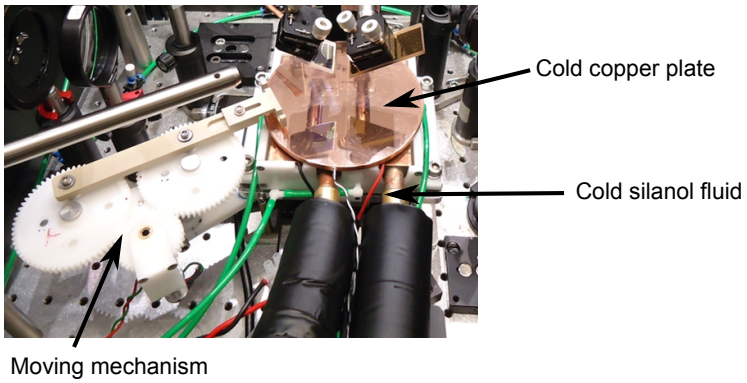

Figure 6.1: Cooling ice stage with a custom made moving mechanism.

6.2 Ice-air time resolved SFG experiments

In time resolved experiments, an intense IR-pump excites a fraction of the molecules from the ground state $v = 0$ to the first vibrational state $v = 1$ (see chapter 2). Zero time delay between the IR pump and the SFG-probe is determined with the third-order IR+IR+VIS (IIV) SFG signal, and is defined as the maximum of the IIV intensity. Figure 6.2 shows an SFG spectra of the intense excitation pulse (in red, FWHM 140 cm^{-1} at 3105 cm^{-1}) and of ice (in blue) in absence ("unpumped") of the intense excitation pulse.

Figure 6.3 shows the ice SFG spectrum in the absence ("unpumped") and in the presence ("pumped") of the intense excitation IR pump pulse. Figure 6.3a displays the SFG spectra at a zero time delay (t=0) between the IR-pump and the SFG-probe and figure 6.3b at a long time delay (t=15 ps). In both figures the intensity of the "pumped" SFG spectrum is lower than the "unpumped" one. The red curve in the bottom panel is the "pumped" SFG spectrum divided by the "unpumped" one.

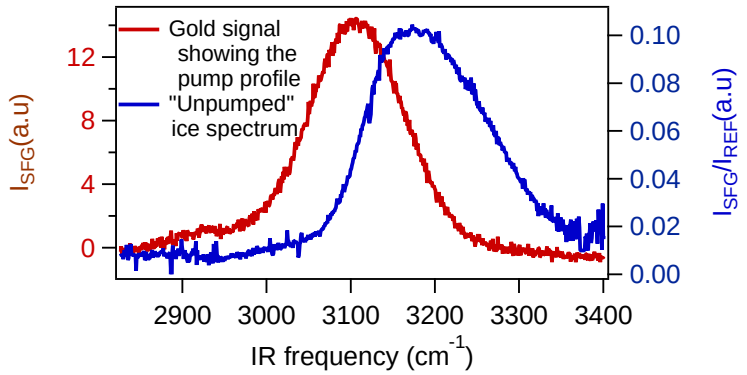

Figure 6.2: SFG spectrum of basal face (0001) of ice in absence ("unpumped") of the intense excitation pulse (in blue) at 230 K, and the gold SFG spectrum showing the spectral profile of the intense excitation IR pulse centered at 3105 cm^{-1}(in red).

At zero time delay, the "pumped/unpumped" SFG signal has an intensity smaller than 1 (Fig. 6.3a and c). This intensity reflects the perturbation in the equilibrium population due to the IR pump, and is commonly referred to as bleach. Later in time, as the molecules relax back, the SFG signal should return to the original ground state spectrum. However, an increase in the local temperature, due to the energy conversion of the IR pump pulse to heat, causes the system to relax to a state similar, but not equal to the ground state, see explanation in the next section. This heat causes the decrease in intensity of the "pumped/unpumped" SFG signal at long time delays (Fig. 6.3b and d).

In other systems, such as liquid water, the pump induced heat, at long time delay, causes the SFG signal to shift to higher frequencies because of the weakened hydrogen bonds. However, as we learned in chapter 5, when the ice sample is heated, the SFG signal decreases in intensity until a surface phase transition at $\sim$ 257 K, where the spectra suddenly shift to higher frequencies. The first spectral moment of the normalized pumped ($I_{SFG,pumped}/I_{REF}$) and unpumped ($I_{SFG,unpumped}/I_{REF}$) spectra of figure 6.3b, show spectra peaking at 3186 cm^{-1} and 3189 cm^{-1}, respectively. Thus the first spectral moment is similar, in agreement with the results of chapter 5.

From the difference in area under the SFG ice peaks, one can approximate the pump induced increase in temperature of the system at long time delays. The ratio of the areas under the SFG unpumped vs pumped spectra from the time resolved ice data (Fig. 6.3b) is 0.76. From figure 5.3c, it can be concluded that this corresponds to a pump-induced temperature increase by $\sim$10 K at long time delays.

6.3 Vibrational dynamics of the hydrogen bonded OH stretch band of Ice vs Water

Fig 6.4 shows the ratio of the pumped and unpumped SFG spectra for water (red) and ice (black) vs the time delay between the IR pump and the SFG probe. As previously mentioned, initially the system is in equilibrium, corresponding to negative time delays. Then the IR pulse creates a depletion of the probe SFG signal at time zero. Finally, the system relaxes to a state similar to the ground state. From the data it is clear that the recovery of the SFG signal after the excitation is faster for ice than for water.

To quantify the dynamics, the data are fitted to a four level energy model; the fits are shown

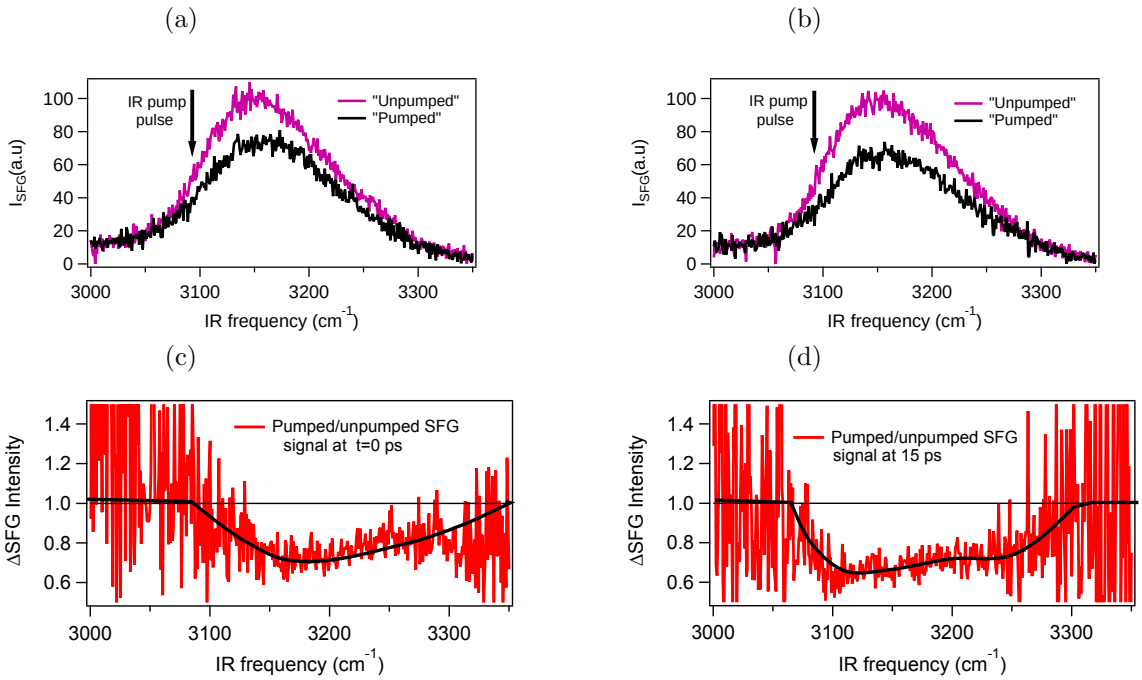

Figure 6.3: SFG spectra recorded from the basal face (0001) of ice in presence ("pumped") and absence ("unpumped") of the intense excitation pulse at (a) zero time delay (t=0) between the IR pump and the SFG probe and (b) at long time delays (t=15 ps). In pink and black are the "unpumped" and "pumped" SFG signals. (c) and (d) are the SFG intensity (ratio of "pumped" SFG "unpumped" SFG) at zero time delay and at 15 ps. The black solid lines are guides to the eye. The SFG signals are collected for 5 min and are the average of four spectra.

as solid lines in figure 6.4. Figure 6.5 shows the four level energy scheme that is used to fit the time resolved data. In this model the vibrational relaxation from $v = 1$ occurs through an intermediate state v^*. This intermediate state is a combination of the ground state of the OH stretch vibration and other modes that accept energy from the $v = 1$ state [158]. For liquid H_2O, the $v = 1$ population decays to v^* through intermolecular relaxation of the H-O-H bending mode overtone (3300 cm^{-1}) and the O-H hydrogen stretch mode [48, 179, 180]. This explanation also applies to frozen H_2O, because the H-O-H bending mode of ice is a broad band centered at 1660 cm^{-1} [181, 182]. From v^* the system relaxes to a new ground state ($v_0^{'} = 0$) at elevated temperatures. This state has different optical properties from the original ground state.

Figure 6.5 also shows the susceptibilities of the ground (χ_0), the intermediate (χ_v^*) and the new ground state ($\chi_v^{'}$). δ_0 is the absorption cross-section of the $v = 0$ to $v = 1$ transition. T_1 is the vibrational relaxation time from the excess of energy transition from $v = 1$ to v^*, and τ_{eq} the relaxation time from v^* to $v_0^{'}$.

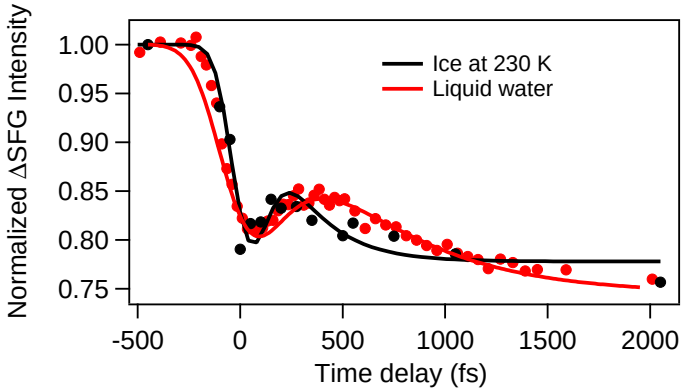

Figure 6.4: Normalized IR-pump/SFG-probe signal of the hydrogen-bonded OH region at the water-air interface pumped at 3350 cm^{-1}(in red) measured by Cho-Shuen Hsieh, and the ice-air interface pumped at 3105 cm^{-1}(in black). The solid lines are the result of the four level energy model, see text for details.

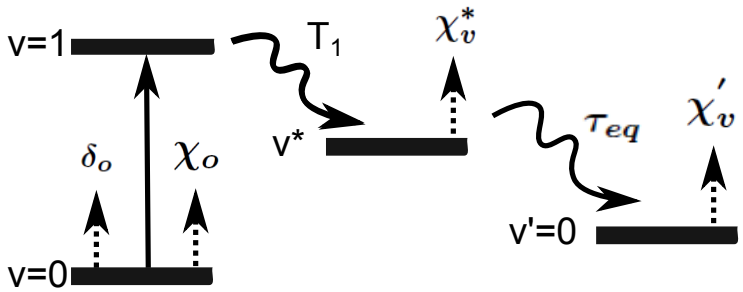

Figure 6.5: A four level energy description for the intermolecular vibrational relaxation where the ground state ($v = 0$) is partially depleted by the pump (solid arrow), then the relaxation (wavy arrows) from the excited state ($v = 1$) occurs through an intermediate state before reaching the new ground state ($v_0' = 0$), see text for details.

The population of each level can be calculated by solving the coupled differential equations:

$$\begin{aligned}
\frac{\partial N_0}{\partial t} &= -\delta_0 I(t)[N_0 - N_1] \\
\frac{\partial N_1}{\partial t} &= \delta_0 I(t)[N_0 - N_1] - \frac{N_1}{T_1} \\
\frac{\partial N_{v*}}{\partial t} &= \frac{N_1}{T_1} - \frac{N_{v*}}{\tau_{eq}} \\
\frac{\partial N_{v'}}{\partial t} &= \frac{N_{v*}}{\tau_{eq}}
\end{aligned} \tag{6.1}$$

where $\frac{\partial N_x}{\partial t}$ is the rate of population change in level Nx with respect to time, δ_0 the absorption cross-section for the $0 \rightarrow 1$ transition and $I(t)$ is the Gaussian pump pulse with a certain pulse duration. $I(t)$ is related to the instrument response which is approximated as a Gaussian, FWHM (154 fs) of the temporal IIV signal [183].

The populations of each level (6.1) are used to calculated the expected change in the SFG signal [184]:

$$\Delta I^N_{SFG(t)} = \frac{\chi_0[N_0(t) - N_1(t)] + \chi_{v*}N_{v*}(t) + \chi_{v'}N_{v'}(t)]^2}{\chi_0[N_0(t << 0)]^2} \tag{6.2}$$

$N_0(t << 0)$ is the population of the ground state before the pump pulse. If we assume that χ_0 and χ^*_v are identical [185], then we can express the equation as:

$$\Delta I^N_{SFG(t)} = \frac{[N_0(t) - N_1(t) + N_{v*}(t) + O_{v'}N_{v'}(t)]^2}{[N_0(t << 0)]^2} \tag{6.3}$$

where $O_{v'}$ is related to the susceptibility of the new ground state [186].

We fit the time traces (solid lines in Fig. 6.4) using the equations (6.3) and (6.1). The values of $O_{v'}$ and τ_{eq} are free parameters obtained from the fit. The description works well, allowing us to extract information of the vibrational dynamics of the hydrogen bonded OH stretch of the ice at 230 K at the liquid water interface. The vibrational relaxation time T_1 is inferred to be 200 fs and 70 fs for water and ice, respectively. These values are similar to the vibrational relaxation times of bulk and interfacial liquid water [167, 187], and bulk ice [160, 177].

The equilibration time τ_{eq} is inferred to be 478 ± 59 and 215 ± 40 fs for liquid water and ice, respectively. This shows that the equilibration time is also shorter for ice than for liquid water. This implies that the water molecules at the ice-air interface are strongly coupled to each other, dissipating the excess energy faster.

6.4 Summary and Outlook

In summary, the relaxation time T_1 of the O-H bonded OH stretch mode of the water molecules at the ice-air interface is shorter than at liquid water air interface. In the future, we can study the structural heterogeneity and delocalization of intermolecular interactions of ice by analysing the frequency dependence of the vibrational relaxation of the stretch bonded OH region. We can achieve this by probing the vibrational dynamics over extended frequency ranges, and compare the results with liquid water [48].

Also, we can learn more about the intermolecular coupling of the molecules by measuring an isotopically diluted ice sample [174, 175, 177]. Isotope diluted ice will switch off the intermolecular coupling between the water molecules. Then the excitation probes only the local environment. Moreover, isotope diluted ice will also tell us more about the v^* state and the other modes that are involved in the relaxation such as the bending overtone, and the asymmetric OH stretching mode of the H_2O (DDAA) and the H_2O (DDA) molecules, see chapter 1.

Chapter 7

Conclusions and Outlook

7.1 Conclusions

Liquid water is a major component in our bodies and of the Earth's surface. Thus, it is not a surprise that a lot of investigations have been devoted to this topic, as a result of our intrinsic curiosity. Frozen water, or ice, also has a special place in human history, and has been of scientific interest since the 1830s. However, our interest has existed even in earlier times when ice was used for food preservation, which was reflected in large scale commercial ice trade that started in 1806. Moreover, even before our existence, ice has shaped the continental crust.

In this thesis, we studied (i) an aqueous system where a model membrane interacts with amphiphilic dendrimers and (ii) single crystalline ice. We provided a molecular scale description of the model membrane-dendrimer and ice-air interfaces. To this end we used sum frequency generation spectroscopy, which gives unique information on the vibrational response of the outermost molecules of the materials.

In vibrational Sum Frequency Generation (SFG) an infrared and a visible pulse overlap in time and space, and generate the sum frequency signal. The infrared photon is in resonance with a vibration at the sample surface, and the visible photon up-converts the resonant signal to a higher energy. SFG is forbidden in centrosymmetric media, which implies that the SFG signal is only present where the symmetry is broken, for instance at interfaces. In this thesis we focused on the region between 2800 and 3750 cm^{-1}, which includes the CH and OH stretch vibrations of the interfaces.

We exemplify the potential uses of SFG by showing that this method could determine the orientation of a polymer at an interface. We did this by studying the interaction of two polymers with a silica interface. Our aim was to understand how silanol functionalization reduces filler aggregation in composites. One of the polymers had silanol ends whereas the other one did not. We observed that covalently attached polymers are more ordered at the silica interface, presumably because of the Si-OH groups of the polymer.

Dendrimer-model membrane interactions

We studied dendrimers, which are highly branched macromolecules that were synthesized step by step by our co-workers. In this work, we focused on polyphenylene dendrimers (PPDs), which were amphiphilic molecules. We wanted to understand how they entered a cell through its membrane (Fig 7.1). We made a systematic study of different PPDs with various hydrophobic and hydrophilic groups. The aim was to understand and design the ideal dendrimer structure for efficient cell uptake. Our colleagues performed cell uptake measurements and we compared them with the

surface activity at the model membrane-air interface.

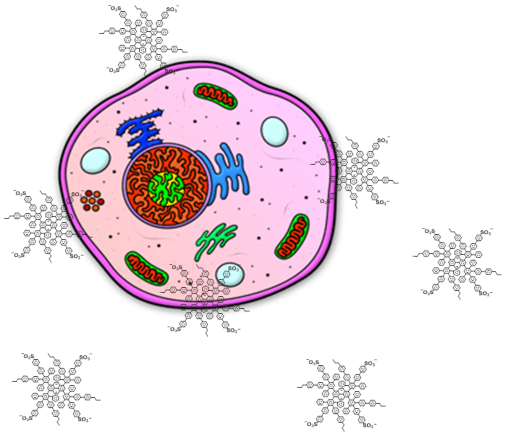

Figure 7.1: Cartoon of cell penetrating PPDs and membrane interactions.

We observed that dendrimers with a linear hydrophobic chain (i.e. n-propyl or n-hexyl) at their surface exhibited better cell uptake than the ones with a branched chain (i.e. isopropyl). Moreover, when the dendrimers only had hydrophilic groups at the surface (i.e. sulfonate acid), the cell uptake was significantly reduced. Therefore, the following question arises: why do amphiphilic PPDs modified with linear chain alkyl groups exhibit better cell uptake than the other studied macromolecules?

To answer this question, we analysed how the dendrimers interact with a model membrane, a DPPC lipid monolayer, using SFG. The surface activity of the PPDs followed this order: non alkyl functionality < isopropyl < phenyl-n-hexyl = phenyl- n-propyl = n-propyl. This was in agreement with the cell uptake results.

PPDs with different hydrophilic groups (a carboxylic acid instead of a sulfonic acid) had similar surface activity at the model membrane-air interface, as well as similar cell penetrating properties. These findings supported the hypothesis that the PPD-cell membrane interactions were dominated by the hydrophobic chains.

When the PPDs penetrate a cell, they first have to bind to the cell membrane to then pass through it. The binding of the dendrimer with the membrane seems to be a good predicator of the cellular activity. It seems that this binding to the membrane is the rate limiting step in the total process.

Single crystalline ice

On ice surfaces it is known that a quasi-liquid-layer (QLL) is present even below its freezing point. Molecular information about the ice surface and the influence of the QLL is important for understanding the surface chemistry of ice near freezing conditions, and the melting mechanism of the ice surface. This has important geophysical implications on the macroscopic scale of our planet such as glacier sliding, and atmospheric chemistry in the free troposphere and the planetary boundary layer.

We were interested in the formation of the QLL. We wanted to know: (1) at which temperature and (2) how the QLL was formed, (3) the nature of the QLL, and (4) the molecular relaxation dynamics of the ice interface. To answer those questions we used a well defined surface and an experimental technique that could give us information about the ice interface. For that we used single crystalline ice and SFG, in combination with simulations.

In this thesis, we produced cylindrical single crystalline ice of 60 mm diameter and 30 mm length. Single crystals were grown from a melt using the seed extraction from the melt method, where a single crystalline seed was slowly withdrawn from the melt. The crystallinity of the ice samples was confirmed by using crossed polarizers in a Universal Stage. Subsequently, a sample with a desired surface orientation (i.e. basal or secondary prism) was cut with a band saw. The sample surface orientation was checked mainly by Formvar etching, but also by X-Ray diffraction.

Experimentally, by heating the ice sample starting at 235 K, a rather abrupt blue shift of the frequency of the OH stretch modes of hydrogen bonded interfacial water molecules was observed at 257 K. This points to an abrupt weakening of the hydrogen bonding structure at the interface. From a comparison of the experiments with simulations (performed by our colleagues), we concluded that the QLL melts in a discrete manner, from one to two bilayers at 257 K. Xing Wei and Yuen-Ron Shen concluded that the QLL starts appearing around 200 K. Figure 7.2 summarizes our findings.

Figure 7.2: Cartoon that summarizes the surface melting of ice: at $\sim$ 200 K a transition from non QLL to a bilayer of QLL was assumed from literature, then at $\sim$ 257 K a transition from one to two QLLs was observed both theoretically and experimentally.

Moreover, a comparison of the SFG response of ice at 270 K with super cooled water at the same temperature indicated that the QLL is more similar to ice than to liquid water. The QLL seems to have stronger hydrogen bonds than liquid water.

We also studied the relaxation dynamics of the ice-QLL-air interface at 230 K with time resolved SFG (Fig. 7.3). The data followed a four-energy level model, where the excited molecules relaxed through an intermediate level. The vibrational relaxation time (T_1) of water molecules at the ice surface was $\sim$ 70 fs, similar to bulk. Furthermore, the relaxation time of ice was shorter than that of liquid water (200 fs).

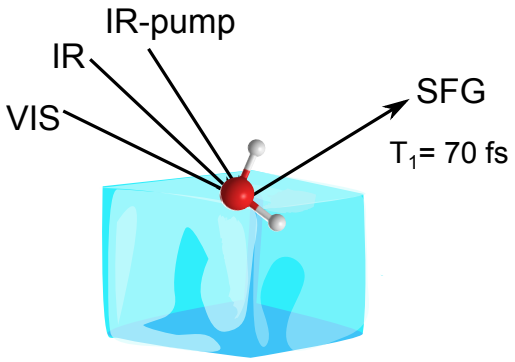

Figure 7.3: Vibrational relaxation dynamics of the ice interface at 230 K.

7.2 Outlook: Proton transfer in crystalline ice

In liquid water, protons are involved in acid-base reactions. The solvated ion, as shown in Fig. 7.4, can form a covalent bond with a water molecule, forming a hydronium ion H_3O^+, and also forming a hydrogen bond with water molecules. Protons in water have an anomalously high conductivity. The high mobility has been assigned to the movement of the charge, rather than the mass, of the proton, which is transferred from one water molecule to the others [188]. The proton charge is delocalized in an extended hydration structures, forming the so-called Eigen ($H_9O_4^+$) and Zundel [$H_2O \cdots H \cdots H_2O$] complexes [189–191].

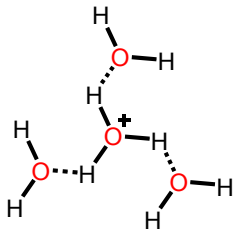

Figure 7.4: A proton (H_3O^+) that is hydrogen-bonded to three water molecules.

In frozen water (hexagonal ice), even though it has a solid crystalline structure, proton transfer is also present. This has been studied since the 1950s by Bjerrum [192]. Moreover, Eigen and co-workers conducted electric conductivity measurements in the 1960s that reported proton mobilities in ice 10-100 times faster than in water [193]. Thus ice is referred to sometimes as a "protonic semiconductor", but the protons do no follow the band theory of electrons in solids [24]. However, the proton transfer mechanism is expected to be quite different from liquid water, and is still under debate [194].

Some impurities that generate protons in ice play an important role in our environment, for example in cloud charging and stratospheric chemistry (Fig. 7.5). HCl forms part of the stratospheric ice clouds and is involved in the depletion of the ozone layer [195, 196]. Some of the reactions that are catalysed on ice are the following:

$$ClONO_2 + HCl \longleftrightarrow Cl_2 + HNO_3$$

$$HOCl + HCl \longleftrightarrow Cl_2 + H_2O$$

Those reactions produce a photolabile dihalogen, Cl_2, which can initiate O_3 destruction.

In this chapter the state of the art of proton transport in crystalline hexagonal ice is described. Moreover, an experimental approach is suggested for studying the proton transfer in ice. The mechanism and the number of ice water molecules that are affected per proton is still unknown. HCl impurities in ice are chosen as the sample because they may form H_3O^+ ions in ice and because of their environmental implications.

7.2.1 State of the Art

Similar to liquid water, it is known that protons can move in ice. The main difference between liquid and solid water is that the water molecules cannot reorient as easily as in the liquid phase, because the water molecules are organized in a lattice structure [193, 194]. This implies that the

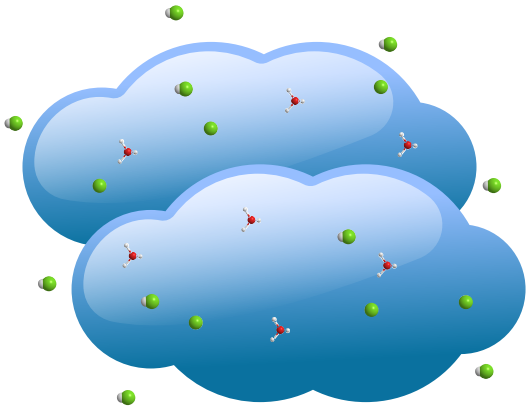

Figure 7.5: Scheme of clouds made from ice particles, H_3O^+ (protons, with the oxygen in red and hydrogen in white), chloride (in green).

water molecules are more easily polarized in liquid water than in ice. Indeed, the Debye relaxation time τ_D, which is inversely proportional to the change of polarization of a system that is exposed to an alternating current (AC), is $\tau_D \approx 1.5 \times 10^{-4}$ s for ice at 263 K, and $\tau_D \approx 5 \times 10^{-11}$ s for water at 283 K. [197]. Ice defects that locally violated the third ice rule (chapter 1), explain this relaxation times.

Figure 7.6 shows four types of protonic point defects, where the rotation of the water molecules can create empty bonds (*L-defects*) or bonds with two protons (*D-defects*), known as Bjerrum defects. The other two defects are the ionic defects, H_3O^+ and OH^-.

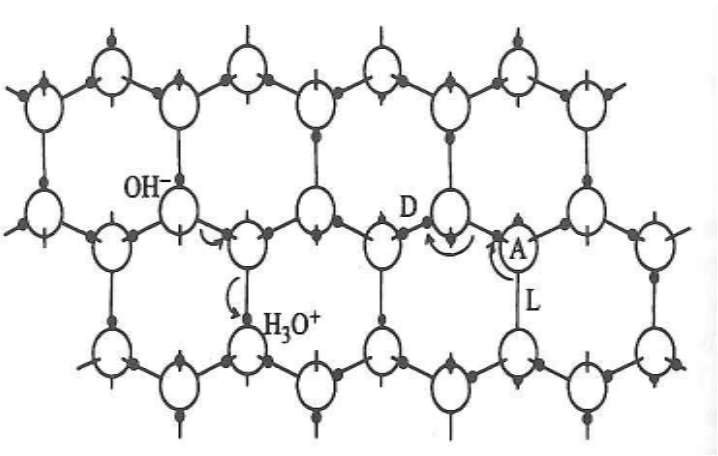

Figure 7.6: Ionic and Bjerrum defects introduced in an ice crystalline structure, from [24].

Little is known about the actual positions of the protonic defects in the ice lattice, or how many water molecules they affect. Considerable relaxation is expected to happen constantly in order to minimize the energy of the crystal. Most of the literature seems to agree that these ionic defects are formed by the transfer of a proton from one molecule to the neighbouring molecule. For proton transfer to occur, it has been proposed that both *D-defects* and H_3O^+ are needed. Figure 7.7 shows a model of a zig-zag path of the water molecules. In (a) a proton is introduced which

forms the H_3O^+ ion, then in (b) the proton jumps to the end of the water chain. As a result of the proton jumping, the polarization of the chain has been reversed so that a second ion cannot pass. But, by rotating the first water molecule (c) we have a *D-defect* which will also travel from left to right in the chain, leaving a chain similar to (a). Then, another H_3O^+ ion can be introduced, and the process can be repeated. Notice that the *D-defects* produce reorientation of the molecules whereas H_3O^+ produces a reorientation of the bonds in the direction of motion, and would leave molecules oriented against an AC field.

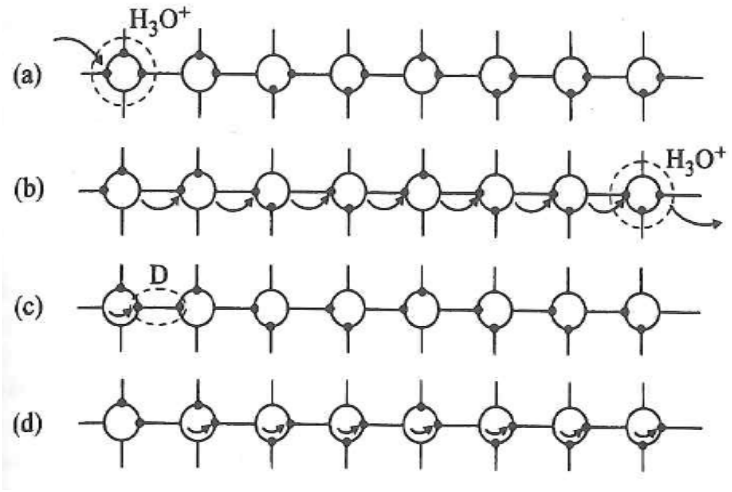

Figure 7.7: The propagation of an H_3O^+ ion followed by a *D-defect* along a straight chain of water molecules, from [24].

Similar to the effect of doping in semiconductors where a donor or an acceptor releases electrons or holes, the defect concentration has a direct effect on the electrical properties of ice. Polar ice cores usually contain a mixture of ions; it has been reported that its conductivity primarily depends on the acidity.

Even though liquid water is known as a universal solvent, many substances are virtually insoluble in ice. For example, NaCl is almost insoluble in ice. This means that ice which freezes from sea water is almost pure. However, HF, HCl, KOH, NH_3 and NH_4F are soluble and can be frozen with the water to form doped ice [24].

HF and HCl are substitutes for an H_2O molecule in ice, creating a bond which lacks a proton and realizing H_3O^+ [198] (Fig. 7.8). Interestingly, it has been reported that at high temperatures the L-defects are fully dissociated, and the HCl ionizes as a weak acid, even though it is considered to be a strong acid in liquid water [199, 200].

The conductivity of HCl-doped ice vs temperature has a change in slope at ~ 220 K. Below this temperature, the conductivity decreases as the temperature decreases [200–202]. Furthermore, the proton jumping time of polycrystalline HCl-doped ice has a strong temperature dependence from 140-195 K. This time increases as the temperature decreases. [203–205]. Thus, it seems that the conductivity increases as function of temperature because the proton movement is temperature dependent.

In polycrystalline ice samples it has been estimated that the protons move across lengths of about 6 to 16 water molecules [206]. Using femtosecond vibrational spectroscopy, Timmer *et al.* studied proton transfer in polycrystalline ice by releasing protons from a photo-acid that was electronically excited [207]. During the experiment the protons move until they recombine with a

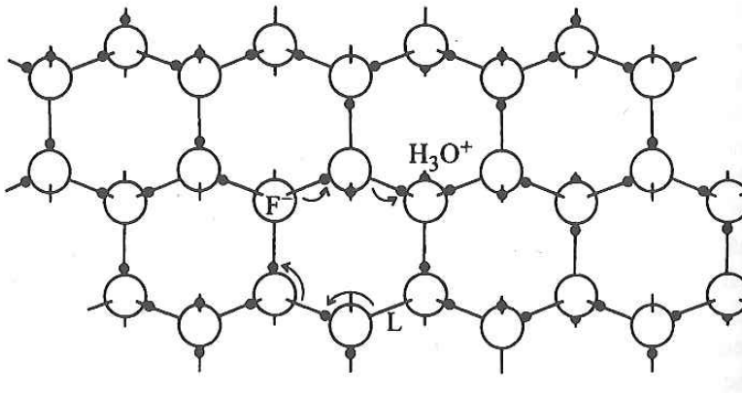

Figure 7.8: Introduction of an HF molecule in place of one H_2O molecule, followed by a release of an $L-defect$ and an H_3O^+ ion, from [24].

sodium formate base. The authors concluded that protons transfer across lengths of about four water molecules, which is higher than in liquid water (up to two) [207].

The surface of HCl-doped ice is a highly dynamic place were important chemical atmospheric reactions take place [208]. Molecular dynamics simulations have suggested that Cl^- forms part of the ice lattice. Some reports concluded that the Cl^- resides in the bulk [209], but others also observed it concentrated at the surface [210, 211]. Recently, it has been calculated that the mobility of the protons at the surface is suppressed at temperatures below 200 K, whereas in bulk a fast proton transport through the hydrogen bonding network takes place even below 200 K. These findings indicate that the quasi-liquid layer that is formed above 200 K plays an important role in proton mobility [212, 213]. It has been suggested that the QLL slows down the ion self-diffusion [213].

Also, experimental studies contradict each other: some have concluded that protons have no surface affinity [214–216], whereas others have concluded that the protons reside at the surface rather than in the bulk [203, 217–220]. Adsorption isotherms between 190 and 220 K show no systematic temperature dependence, which may indicate that HCl ionizes at the surface [218].

Thus, it has been a topic of interest for many researchers. However, important questions such as: "How does proton transfer occur in and on ice? What is the molecular view of the protons at the ice-air interface? And what is the influence of the quasi-liquid layer?" have been unanswered or only partially answered.

7.2.2 Implementation

This project focuses on understanding at a molecular level the proton transfer in ice and on its surface. We would like to answer how proton transfer occurs in and on ice, and to understand the proton transfer at the ice-air interface. For doing this, we need to prepare well-defined ice samples, and to use experimental techniques that allows us to probe the proton transfer in and on ice.

The following subsections summarize the implementation of the project, divided in sample preparation and proton transfer characterization.

Sample preparation

In order to reproduce and understand proton transfer in ice samples, we must produce such samples in a well-defined way. Polycrystalline ice will have many grain boundaries which are known to affect

the proton mobility [221]. Therefore, we will prepare single crystalline ice doped with HCl.

As we learned in this chapter and in chapter 1, hexagonal ice has an open structure that has protonic defects. Doping the ice with HCl will increase the amount of these protonic defects. Single crystalline ice doped with ions can be produced in two ways: (i) by freezing a mixture of water and HCl or (ii) by absorbing HCl in the gas phase into single crystalline ice (Fig. 7.9).

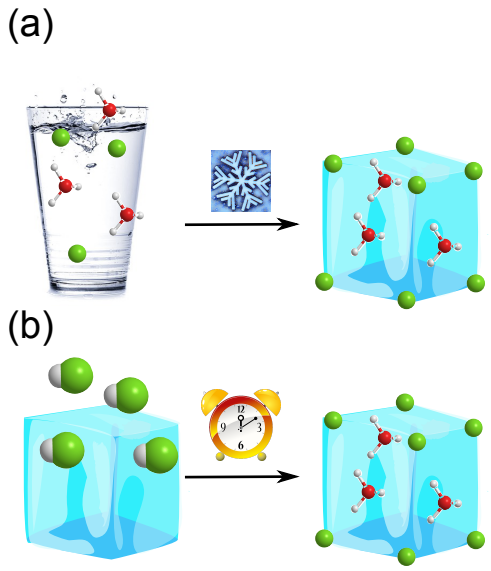

Figure 7.9: Cartoon of two HCl-doped ice synthesis methods. (a) From freezing a liquid water+HCl mixture and (b) by HCl gas adsorption into ice.

As we have shown, it is possible to produce highly reproducible ice single crystals from the seed extraction from the melt technique, see chapter 4. We propose to use the same procedure for HCl-doped ice. Moreover, HCl-doped ice from a HCl (1 x 10^{-4} mol/l) solution has been produced by the Bridgeman method [202]. The HCl can also be introduced in ice by first producing single crystalline ice, and secondly introducing HCl in the gas phase similar to Zimmermann and co-workers [218].

Sample characterization

After producing the HCl-doped ice, the first question that arises is whether the acid is inside the ice samples. For that, we can characterize the bulk of the sample by the following methods. The pH of a molten sample could be measured. Furthermore, a comparison of the linear Infrared and Raman responses of an undoped and doped ice sample contains information of the bulk ice [222, 223].

We can further study how the proton transfer phenomena happens in ice by probing the changes of the dielectric relaxation $\hat{\epsilon}(\omega)$ at different temperatures, which is possible with THz-time domain spectroscopy (THz-TDS), Fig. 7.10(a). $\hat{\epsilon}(\omega)$ of water has information on how its permanent dipoles can keep up with oscillating fields at the frequency ω. The dielectric response changes when ions are added to the ice samples because the dielectric response now includes the conductivity of the charged ions. Further, the relaxation processes of the water molecules are affected by the surrounding ions [188, 224].

The electric field of ions affects the reorientation dynamics of the surrounding water molecules, causing a depolarization effect. The addition of protons in aqueous solutions strongly decreases the dielectric response [188]. In pure ice, the complex dielectric constants ($\hat{n}^2 = \hat{\epsilon}$) has been previously

reported [225, 226]. Takeya and co-workers concluded that the real dielectric constant increases with temperature between 20 and 140 K in the frequency range of 0.2 to 1.4 THz, and that the imaginary part is influenced by infrared phonon absorption [226].

To understand the molecular view of the protons at the ice-air interface and the influence of the ice-QLL-air interface, we need a surface-specific technique, in this case we will use sum frequency generation (Fig. 7.10(b)). We have studied the formation of the QLL with this method, see chapters 2 and 5. If the H_3O^+ resides at the interface, it will affect the interfacial hydrogen-bonding network. At the liquid water-air interface it is still under debate if the protons are in excess at the surface. Evidence of the excess of protons as the interface has been observed experimentally by an increase of the intensity of the OH-stretching bond and with a hydrogen bonded OH stretch that shifts to lower frequencies [222, 227]. We will compare doped ice samples with liquid water ones.

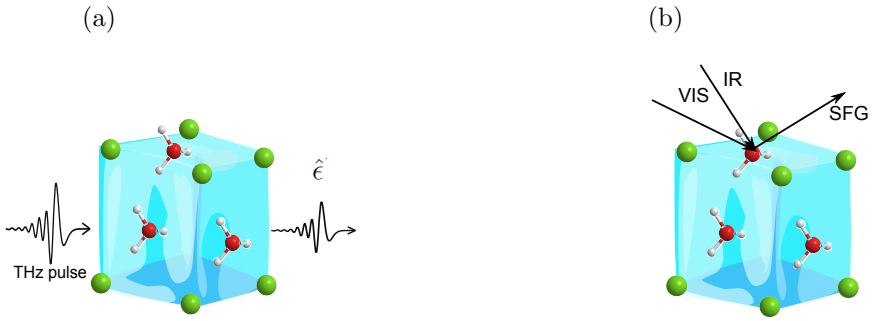

Figure 7.10: Protonic defect transfer: (a) in ice by studying the dielectric complex constant with THz-time domain spectroscopy, and (b) at the ice-air interface by analysing the molecular vibrations of the frozen water molecules. Green atoms represent Cl^-.

We have learnt in this chapter that HCl-doped ice is an atmospherically relevant sample. Besides that important fact, the hydrochloride acid induces protonic defects in the ice crystalline structure. Those defects change the characteristics of the ice (e.g. conductivity). Moreover, the average molecular structure of the HCl-doped ice is highly debated. Therefore, in the future we aim to understand its molecular picture by studying: (1) the dielectric relaxation of the HCl-doped ice and (2) IR resonant vibrations of the water molecules at the HCl-doped ice/air interface.

Bibliography

[1] P. Ball, "Water: Water — an enduring mystery," *Nature*, vol. 452, no. 7185, pp. 291–292, 2008.

[2] Y. Levy and J. N. Onuchic, "Water and proteins: A love- hate relationship," *PNAS*, vol. 101, no. 10, pp. 3325–3326, 2004.

[3] WAIS Divide Project Members, "Precise interpolar phasing of abrupt climate change during the last ice age," *Nature*, vol. 520, pp. 661–665, 2015.

[4] S. A. Marcott, T. K. Bauska, C. Buizert, E. J. Steig, J. L. Rosen, K. M. Cuffey, T. J. Fudge, J. P. Severinghaus, J. Ahn, M. L. Kalk, J. R. Mcconnell, T. Sowers, K. C. Taylor, J. W. C. White, and E. J. Brook, "Centennial-scale changes in the global carbon cycle during the last deglaciation," *Nature*, vol. 514, no. 7524, pp. 616–619, 2014.

[5] J. G. Dash, A. W. Rempel, and J. Wettlauter, "The physics of premelted ice and its geophysical consequences," *Rev. Mod. Phys.*, vol. 78, no. 3, pp. 695–741, 2006.

[6] K. M. Cuffey, H. Conway, B. Hallet, A. M. Gades, and C. F. Raymond, "Interfacial water in polar glaciers and glacier sliding at 256K," *Geophys. Res. Lett.*, vol. 26, no. 6, pp. 751–754, 1999.

[7] J. P. D. Abbatt, "Interactions of Atmospheric Trace Gases with Ice Surfaces : Adsorption and Reaction," *Chem. Rev.*, vol. 103, pp. 4783–4800, 2003.

[8] N. Pouvesle, M. Kippenberger, G. Schuster, and J. N. Crowley, "The interaction of H_2O_2 with ice surfaces between 203 and 233 K," *Phys. Chem. Chem. Phys.*, vol. 12, pp. 15544–15550, 2010.

[9] A. K. Winkler and J. N. Crowley, "Interaction of formic and acetic acid with ice surfaces between 187 and 227 K . Investigation of single species- and competitive adsorption," *Phys. Chem. Chemi*, vol. 10, pp. 2345–2355, 2008.

[10] A. K. Winkler, N. S. Holmes, and J. N. Crowley, "Interaction of methanol, acetone and formaldehyde with ice surfaces between 198 and 223 K," *Phys. Chem. Chem. Phys.*, vol. 4, pp. 5270–5275, 2002.

[11] T. Huthwelker, M. Ammann, and T. Peter, "The Uptake of Acidic Gases on Ice," *Chem. Rev.*, vol. 106, pp. 1375–1444, 2006.

[12] B. Alberts, A. Johnson, J. Lewis, D. Morgan, M. Raff, K. Roberts, and P. Walter, *Molecular Biology of the Cell*. New York: Garland Science, sixth ed., 2014.

[13] A. Nilsson and L. G. M. Pettersson, "The structural origin of anomalous properties of liquid water," *Nat. Commun.*, vol. 6, p. 8998, 2015.

[14] D. C. Elton and M. Fernández-Serra, "The hydrogen-bond network of water supports propagating optical phonon-like modes," *Nat. Commun.*, vol. 7, p. 10193, 2016.

[15] E. A. Zheligovskaya and G. G. Malenkov, "Crystalline water ices," *Russ. Chem. Rev.*, vol. 75, no. 1, pp. 57–76, 2006.

[16] T. Loerting, W. Schustereder, K. Winkel, C. G. Salzmann, I. Kohl, and E. Mayer, "Amorphous ice: Stepwise formation of very-high-density amorphous ice from low-density amorphous ice at 125 K," *Phys. Rev. Lett.*, vol. 96, no. 2, pp. 5–8, 2006.

[17] P. Hobbs, *Ice Physics*. New York: Oxford University Press, 1974.

[18] W. H. Barnes, "The Crystal Structure of Ice between 0 Celsius and - 183 Celsius," *Proc. R. Soc. London*, vol. 125, no. 799, pp. 670–693, 1929.

[19] C. Kittel, *Introduction to Soild State Physics*. United States of America: John Wiley and Sons, 8th ed., 2005.

[20] V. F. Petrenko and W. Whitworth, "Introduction," in *Physics of Ice*, United States: Oxford University Press, 1999.

[21] J. F. Nagle, "Lattice Statistics of Hydrogen Bonded Crystals. The Residual Entropy of Ice," *J. Math. Phys.*, vol. 7, no. 21, pp. 1484–1492, 1966.

[22] A. Goto, T. Hondoh, and S. Mae, "The electron density distribution in ice Ih determined by single-crystal x-ray diffractometry," *J. Chem. Phys.*, vol. 93, no. 2, pp. 1412–1417, 1990.

[23] O. Haida, "Calorimetric X . Enthalpy study of the glassy state relaxation at the glass-transition of hexagonal ice a," *J. Chem. Thermodyn.*, vol. 6, pp. 815–825, 1974.

[24] V. F. Petrenko and R. W. Whitworth, "Electrical properties-theory," in *Ice Phys.*, pp. 1–30, 2010.

[25] Wikiwand, "Space group http://www.wikiwand.com/en/Space_group," 2016.

[26] M. A. Sánchez, T. Kling, T. Ishiyama, M.-J. van Zadel, P. J. Bisson, and M. Mezger, "Experimental and theoretical evidence for bilayer-by- bilayer surface melting of crystalline ice," *PNAS*, vol. 114, pp. 227–232, 2017.

[27] V. F. Petrenko and R. W. Whitworth, *Physics of Ice*. New York: Oxford University Press, 1999.

[28] S. G. Warren, "Optical constants of ice from the ultraviolet to the microwave," *Appl. Opt.*, vol. 23, no. 8, pp. 1206–1225, 1984.

[29] J. Schaefer, E. H. G. Backus, Y. Nagata, and M. Bonn, "Both Inter- and Intramolecular Coupling of O-H Groups Determine the Vibrational Response of the Water/Air Interface," *J. Phys. Chem. Lett.*, vol. 7, no. 22, pp. 4591–4595, 2016.

[30] V. Buch, T. Tarbuck, G. L. Richmond, H. Groenzin, and I. Li, "Sum frequency generation surface spectra of ice, water, and acid solution investigated by an exciton model," *J. Chem. Phys.*, vol. 127, p. 204710, 2007.

[31] H. Groenzin, I. Li, V. Buch, and M. J. Shultz, "The single-crystal , basal face of ice Ih investigated with sum frequency generation," *J. Chem. Phys.*, vol. 127, no. 21, p. 214502, 2007.

[32] I. L. Barnett, H. Groenzin, and M. J. Shultz, "Hydrogen Bonding in the Hexagonal Ice Surface," *J. Phys. Chem. A*, vol. 115, no. 23, pp. 6039–6045, 2011.

[33] Y. Nagata, "Private communication," 2016.

[34] J. G. Dash, "History of the search for continuous melting," *Rev. Mod. Phys.*, vol. 71, no. 5, pp. 1737–1743, 1999.

[35] G.-J. Kroes, "Surface melting of the (0001) face of TIP4P ice," *Surf. Sci.*, vol. 275, no. 3, pp. 365–382, 1992.

[36] H.-F. Wang, L. Velarde, W. Gan, and L. Fu, "Quantitative Sum-Frequency Generation Vibrational Spectroscopy of Molecular Surfaces and Interfaces: Lineshape, Polarization, and Orientation SFG-VS: sum-frequency generation vibrational spectroscopy," *Annu. Rev. Phys. Chem.*, vol. 66, pp. 189–216, 2015.

[37] A. G. Lambert, P. B. Davies, and D. J. Neivandt, "Implementing the Theory of Sum Frequency Generation Vibrational Spectroscopy: A Tutorial Review," *Appl. Spectrosc. Rev.*, vol. 40, no. 2, pp. 103–145, 2005.

[38] Y. R. Shen, *The Principles of Nonlinear Optics*. United States of America: John Wiley & Sons, Inc, 1984.

[39] R. Boyd, *Nonlinear Optics*. San Diego: Academic Press, 3rd editio ed., 2008.

[40] R. E. Pool, J. Versluis, E. H. Backus, and M. Bonn, "Comparative study of direct and phase-specific vibrational sum-frequency generation spectroscopy: advantages and limitations," *J. Phys. Chem. B*, vol. 115, no. 51, pp. 15362–15369, 2011.

[41] M. Sovago, E. Vartiainen, and M. Bonn, "Determining Absolute Molecular Orientation at Interfaces: A Phase Retrieval Approach for Sum Frequency Generation Spectroscopy," *J. Phys. Chem. C*, vol. 113, pp. 6100–6106, apr 2009.

[42] M. Sovago, E. Vartiainen, and M. Bonn, "Observation of buried water molecules in phospholipid membranes by surface sum-frequency generation spectroscopy," *J. Chem. Phys.*, vol. 131, no. 16, p. 229901, 2009.

[43] K. Shiratori and A. Morita, "Theory of quadrupole contributions from interface and bulk in second-order optical processes," *Bull. Chem. Soc. Jpn.*, vol. 85, no. 10, pp. 1061–1076, 2012.

[44] Q. Wan and G. Galli, "First-Principles Framework to Compute Sum-Frequency Generation Vibrational Spectra of Semiconductors and Insulators," *Phys. Rev. Lett.*, vol. 115, no. 24, pp. 1–5, 2015.

[45] A. Kundu, S. Tanaka, T. Ishiyama, M. Ahmed, K. I. Inoue, S. Nihonyanagi, H. Sawai, S. Yamaguchi, A. Morita, and T. Tahara, "Bend Vibration of Surface Water Investigated by Heterodyne-Detected Sum Frequency Generation and Theoretical Study: Dominant Role of Quadrupole," *J. Phys. Chem. Lett.*, vol. 7, no. 13, pp. 2597–2601, 2016.

[46] J. A. McGuire and Y. R. Shen, "Ultrafast Vibrational Dynamics at Water interfaces," *Science*, vol. 313, pp. 1945–1948, 2006.

[47] M. Smits, A. Ghosh, M. Mueller, and M. Bonn, "Ultrafast Vibrational Energy Transfer between Surface and Bulk Water at the Air-Water Interface," *Phys. Rev. Lett.*, vol. 98, p. 098302, 2007.

[48] S. T. van der Post, C.-S. Hsieh, M. Okuno, Y. Nagata, H. J. Bakker, M. Bonn, and J. Hunger, "Strong frequency dependence of vibrational relaxation in bulk and surface water reveals sub-picosecond structural heterogeneity.," *Nat. Commun.*, vol. 6, no. May, p. 8384, 2015.

[49] R. A. Livingstone, Z. Zhang, L. Piatkowski, H. J. Bakker, J. Hunger, M. Bonn, and E. H. G. Backus, "Water in Contact with a Cationic Lipid Exhibits Bulk-Like Vibrational Dynamics," *J. Phys. Chem. B*, vol. 120, pp. 10069–10078, 2016.

[50] J. R. Schmidt, S. A. Corcelli, and J. L. Skinner, "Pronounced non-Condon effects in the ultrafast infrared spectroscopy of water," *J. Chem. Phys.*, vol. 123, no. 4, 2005.

[51] H. S. Varol, M. A. Sánchez, H. Lu, J. E. Baio, C. Malm, N. Encinas, M. R. B. Mermet-Guyennet, N. Martzel, D. Bonn, M. Bonn, T. Weidner, E. H. G. Backus, and S. H. Parekh, "Multiscale Effects of Interfacial Polymer Confinement in Silica Nanocomposites," *Macromolecules*, vol. 48, p. 7929, 2015.

[52] J. Wang, C. Chen, S. M. Buck, and Z. Chen, "Molecular Chemical Structure on Poly(methyl methacrylate) (PMMA) Surface Studied by Sum Frequency Generation (SFG) Vibrational Spectroscopy," *J. Phys. Chem. B*, vol. 105, pp. 12118–12125, 2001.

[53] Z. Chen, Y. R. Shen, and G. A. Somorjai, "Studies of polymer surfaces by sum frequency generation vibrational spectroscopy.," *Annu. Rev. Phys. Chem.*, vol. 53, pp. 437–65, 2002.

[54] A. G. Kannan, N. R. Choudhury, and N. K. Dutta, "Synthesis and characterization of methacrylate phospho-silicate hybrid for thin film applications," *Polymer*, vol. 48, no. 24, pp. 7078–7086, 2007.

[55] C. Zhang and Z. Chen, "Probing Molecular Structures of Poly (dimethylsiloxane) at Buried Interfaces in Situ," *J. Phys. Chem. C*, vol. 117, pp. 3903–3914, 2013.

[56] G. R. Newkome, C. N. Moorefield, and F. Vögtle, *Dendrimers and Dendrons: Concepts, Syntheses, Applications*. Darmstadt: The Royal Society of Chemistry, 2001.

[57] S. Svenson, "Dendrimers as versatile platform in drug delivery applications," *Eur. J. Pharm. Biopharm.*, vol. 71, no. 3, pp. 445–462, 2009.

[58] B. A. G. Hammer, R. Moritz, R. Stangenberg, M. Baumgarten, and K. Müllen, "Chem Soc Rev The polar side of polyphenylene dendrimers," *Chem Soc Rev*, vol. 44, pp. 4072–4090, 2015.

[59] T. Weil, E. Reuther, and M. Klaus, "Dyads and a Triad for Efficient Vectorial Transduction of Excitation Energy," *Angew. Chem. Int. Ed.*, vol. 41, no. 11, pp. 1900–1904, 2002.

[60] R. Esfand and D. A. Tomalia, "Poly amidoamine (PAMAM) dendrimers: from biomimicry to drug delivery and biomedical applications," *Drug Discov. Today*, vol. 6, no. 8, pp. 427–436, 2001.

[61] G. Mihov, D. Grebel-Koehler, A. Lubbert, G. W. M. Vandermeulen, A. Herrmann, H.-A. Klok, and K. Mullen, "Polyphenylene Dendrimers as Scaffolds for Shape-Persistent Multiple Peptide Conjugates," *Bioconjug. Chem.*, vol. 16, pp. 283–293, 2005.

[62] M. Yin, K. Ding, R. A. Gropeanu, J. Shen, and K. Mu, "Dendritic Star Polymers for Efficient DNA Binding and Stimulus-Dependent DNA Release," *Biomacromolecules*, vol. 9, pp. 3231–3238, 2008.

[63] M. Yin, C. R. W. Kuhlmann, K. Sorokina, C. Li, G. Mihov, E. Pietrowski, K. Koynov, M. Klapper, H. J. Luhmann, and K. Müllen, "Novel Fluorescent Core – Shell Nanocontainers for Cell Membrane Transport," *Biomacromolecules*, vol. 9, pp. 1381–1389, 2008.

[64] A. Herrmann, G. Mihov, G. W. M. Vandermeulen, H.-A. Klok, and K. Müllen, "Peptide-functionalized polyphenylene dendrimers," *Tetrahedron*, vol. 59, pp. 3925–3935, 2003.

[65] R. M. Crooks, M. Zhao, L. I. Sun, V. Chechik, and L. K. Yeung, "Dendrimer-Encapsulated Metal Nanoparticles : Synthesis , Characterization , and Applications to Catalysis," *Acc. Chem. Res.*, vol. 34, no. 3, pp. 181–190, 2001.

[66] P. Kesharwani, K. Jain, and N. K. Jain, "Progress in Polymer Science Dendrimer as nanocarrier for drug delivery," *Prog. Polym. Sci.*, vol. 39, no. 2, pp. 268–307, 2014.

[67] B. He, Y. Chu, M. Yin, K. Müllen, C. An, and J. Shen, "Fluorescent Nanoparticle Delivered dsRNA Toward Genetic Control of Insect Pests," *Adv. Mater.*, vol. 25, pp. 4580–4584, 2013.

[68] P. Kolhe, E. Misra, R. M. Kannan, S. Kannan, and M. Lieh-Lai, "Drug complexation , in vitro release and cellular entry of dendrimers and hyperbranched polymers," *Int. J. Pharm.*, vol. 259, pp. 143–160, 2003.

[69] R. Stangenberg, Y. Wu, J. Hedrich, D. Kurzbach, D. Wehner, G. Weidinger, S. L. Kuan, M. I. Jansen, F. Jelezko, H. J. Luhmann, D. Hinderberger, T. Weil, and K. Müllen, "A Polyphenylene Dendrimer Drug Transporter with Precisely Positioned Amphiphilic Surface Patches," *Adv. Healthc. Mater.*, vol. 4, pp. 377–384, 2015.

[70] C. Z. Chen and S. L. Cooper, "Interactions between dendrimer biocides and bacterial membranes," *Biomaterials*, vol. 23, pp. 3359–3368, 2002.

[71] T. Yu, X. Liu, A.-L. Bolcado-Bellemin, Y. Wang, C. Liu, P. Erbacher, F. Qu, P. Rocchi, J.-P. Behr, and L. Peng, "An Amphiphilic Dendrimer for Effective Delivery of Small Interfering RNA and Gene Silencing In Vitro and In Vivo," *Angew. Chemie Int. Ed.*, vol. 51, pp. 8478–8484, 2012.

[72] V. Márquez-Miranda, I. Araya-Durán, M. B. Camarada, J. Comer, J. A. Valencia-Gallegos, and F. D. González-Nilo, "Self-Assembly of Amphiphilic Dendrimers : The Role of Generation and Alkyl Chain Length in siRNA Interaction," *Sci. Rep.*, vol. 6, no. 29436, pp. 1–15, 2016.

[73] B. A. G. Hammer and K. Müllen, "Dimensional Evolution of Polyphenylenes : Expanding in All Directions," *Chem. Rev.*, vol. 116, pp. 2103–2140, 2016.

[74] S. Bernhardt, M. Kastler, V. Enkelmann, M. Baumgarten, and K. Müllen, "Pyrene as Chromophore and Electrophore : Encapsulation in a Rigid," *Chem. Eur. J.*, vol. 12, pp. 6117–6128, 2006.

[75] R. Stangenberg, I. Saeed, S. L. Kuan, M. Baumgarten, T. Weil, M. Klapper, and K. Müllen, "Tuning Polarity of Polyphenylene Dendrimers by Patched Surface Amphiphilicity - Precise Control over Size, Shape, and Polarity," *Macromol. Rapid Commun.*, vol. 35, pp. 152–160, 2014.

[76] G. Ma and H. C. Allen, "DPPC Langmuir Monolayer at the Air - Water Interface : Probing the Tail and Head Groups by Vibrational Sum Frequency Generation Spectroscopy," *Langmuir*, no. 26, pp. 5341–5349, 2006.

[77] M. Okuno, M. Mezger, R. Stangenberg, M. Baumgarten, K. Mu, M. Bonn, and E. H. G. Backus, "Interaction of a Patterned Amphiphilic Polyphenylene Dendrimer with a Lipid Monolayer: Electrostatic Interactions Dominate," *Langmuir*, vol. 31, pp. 1980–1987, 2015.

[78] T. Keszthelyi, G. Hollo, G. Nyitrai, J. Kardos, and L. Heja, "Bilayer Charge Reversal and Modi fi cation of Lipid Organization by Dendrimers as Observed by Sum-Frequency Vibrational Spectroscopy," *Langmuir*, vol. 31, pp. 7815–7825, 2015.

[79] D. E. Gragson, B. M. Mccarty, and G. L. Richmond, "Ordering of Interfacial Water Molecules at the Charged Air / Water Interface Observed by Vibrational Sum Frequency Generation," *J. Am. Chem. Soc.*, vol. 119, pp. 6144–6152, 1997.

[80] M. Schleeger, Y. Nagata, and M. Bonn, "Quantifying Surfactant Alkyl Chain Orientation and Conformational Order from Sum Frequency Generation Spectra of CH Modes at the Surfactant Water Interface," *J. Phys. Chem. Lett.*, vol. 5, pp. 3737–3741, 2014.

[81] B. A. G. Hammer, "Controlling Cellular Uptake and Toxicity of Polyphenylene Dendrimers by Chemical Functionalization," *ChemBioChem*, vol. submitted, 2017.

[82] X. Chen, W. Hua, Z. Huang, and H. C. Allen, "Interfacial Water Structure Associated with Phospholipid Membranes Studied by Phase-Sensitive Vibrational Sum Frequency Generation Spectroscopy," *J. Am. Chem. Soc.*, vol. 132, no. 17, pp. 11336–11342, 2010.

[83] M. Sovago, G. W. H. Wurpel, M. Smits, and M. Mu, "Calcium-Induced Phospholipid Ordering Depends on Surface Pressure," *J. Am. Chem. Soc.*, vol. 5856, no. 4, pp. 11079–11084, 2007.

[84] S. Nihonyanagi, S. Yamaguchi, T. Tahara, S. Nihonyanagi, and S. Yamaguchi, "Direct evidence for orientational flip-flop of water molecules at charged interfaces : A heterodyne-detected vibrational sum frequency generation study," *J. Chem. Phys.*, vol. 130, p. 204704, 2008.

[85] J. D. Andrade, "Principles of Protein Adsorption," in *Surf. Interfacial Asp. Biomed. Polym. Vol. 2 . Protein Adsorpt.* (J. D. Andrade, ed.), pp. 1–75, New York: Plenum Press, 1985.

[86] C. Wang, H. Groenzin, and M. J. Shultz, "Comparative study of acetic acid, methanol, and water adsorbed on anatase TiO_2 probed by sum frequency generation spectroscopy," *J. Am. Chem. Soc.*, vol. 127, no. 12, pp. 9736–9744, 2005.

[87] R. Perozzo, G. Folkers, and L. Scapozza, "Thermodynamics of Protein–Ligand Interactions: History, Presence, and Future Aspects," *J. Recept. Signal Transduct.*, vol. 24, no. 1-2, pp. 1–52, 2004.

[88] A. Mecke, I. J. Majoros, A. K. Patri, J. R. Baker, M. M. B. Holl, and B. G. Orr, "Lipid Bilayer Disruption by Polycationic Polymers : The Roles of Size and Chemical Functional Group," *Langmuir*, vol. 21, pp. 10348–10354, 2005.

[89] W. Weeks and J. Wettlaufer, "Crystal Orientation in Floating ice sheets," in *Johannes Weertman Symp. Miner. Met. Mater. Soc.*, pp. 337–349, 1996.

[90] G. J. Turner, C. D. Stow, and R. Keatinge, "The manufacture of large samples of monocrystalline ice under microcomputer control," *J. Cryst. Growth*, vol. 80, pp. 463–464, 1987.

[91] N. N. Khusnatdinow and V. F. Petrenko, "Fast-growth technique for ice single crystals," *J. Cryst. Growth*, vol. 163, pp. 420–425, 1996.

[92] M. Ohtomoto, S. Ahmad, and R. Whitwoeth, "A technique for the growth of high quality single crystals of ice," *J. Phys.*, vol. 48, p. 595, 1987.

[93] H. Groenzin, *Sum-frequency studies of single crystalline ice Ih.* PhD thesis, Tufts University, 2007.

[94] P. J. Bisson, *Hydrogen Bonding in the Prism Face of Ice Ih A Study via Sum Frequency Generation Vibrational Spectroscopy.* PhD thesis, Tufts Unversity, 2013.

[95] P. Bisson, H. Groenzin, I. L. Barnett, and M. J. Shultz, "High yield, single crystal ice via the Bridgman method," *Rev. Sci. Instrum.*, vol. 87, p. 034103, 2016.

[96] M. J. Shultz, A. Brumberg, P. J. Bisson, and R. Shultz, "Producing desired ice faces," *PNAS*, vol. 112, no. 45, pp. E6096–E6100, 2015.

[97] D. v. d. S. Roos, "Rapid production of single crystals of ice," *J. Glaciol.*, vol. 14, no. 71, pp. 325–328, 1975.

[98] A. Higashi, M. Oguro, and A. Fukuda, "Growth of ice single crystals from the melt, with special reference to dislocation structure," *J. Cryst. Growth*, vol. 3, no. 4, pp. 728–732, 1968.

[99] W. M. Ketcham and P. V. Hobbs, "The prefered orientation in the growth of ice from the melt," *J. Cryst. Growth*, vol. 1, no. 5, pp. 263–270, 1967.

[100] C. J. Langway, "Ice Fabrics and the Universal Stage," *Army Snow Ice Permafr. Res. Establ.*, vol. Techical R, pp. 1–17, 1958.

[101] A. Miyamoto, I. Weikusat, and T. Hondoh, "Instruments and Methods Complete determination of ice crystal orientation using Laue X-ray diffraction method," *J. Glaciol.*, vol. 57, no. 201, pp. 103–110, 2011.

[102] J.-P. Colinge, "SOI Materials Characterization," in *Silicon-on-insulator Technol. Mater. to VLSI*, pp. 69–116, Kluwer Academic Publishers, third ed., 2004.

[103] I. Li, *Sum Frequency Studies of Single Crystal Ice (Ih) as Related to its Lattice Orientation.* PhD thesis, University of Tufts University, 2008.

[104] K. Higuchi, "The etching of ice crystals," *Acta Metall.*, vol. 6, no. 10, pp. 636–642, 1958.

[105] D. v. d. S. Roos, "Two - dimensional grain growth in ice," *J. Glaciol.*, vol. 6, no. 45, pp. 411–420, 1966.

[106] N. A. Von Armin, R. List, W. C. Mayes, and M. R. De Quervain, "Kristallachsenlagen in Hagelkörnern," *Zeitschrift für Angew. Math. und Phys.*, vol. 14, no. 5, pp. 574–589, 1963.

[107] H. Bluhm and M. Salmeron, "Growth of nanometer thin ice films from water vapor studied using scanning polarization force microscopy," *J. Chem. Phys.*, vol. 111, no. 15, pp. 6947–6954, 1999.

[108] H. Bluhm, D. F. Ogletree, C. S. Fadley, Z. Hussain, and M. Salmeron, "The premelting of ice studied with photoelectron spectroscopy," *J. Phys. Condens. Matter*, vol. 14, no. 8, pp. L227– L233, 2002.

[109] M. Lohmeier and E. Vlieg, "Angle Calculations for a Six-Circle Surface X-ray Diffractometer," *J. Appl. Crystallogr.*, vol. 26, no. 5, pp. 706–716, 1993.

[110] A. D. Fortes, I. G. Wood, D. Grigoriev, M. Alfredsson, S. Kipfstuhl, K. S. Knight, and R. I. Smith, "No evidence for large-scale proton ordering in Antarctic ice from powder neutron diffraction," *J. Chem. Phys.*, vol. 120, no. 24, pp. 11376–11379, 2004.

[111] M. Faraday, "On Regelation, and on the Conservation of Force," *Philos. Mag.*, pp. 162–169, 1859.

[112] R. Rosenberg, "Why Is Ice Slippery?," *Phys. Today*, vol. 58, no. 12, pp. 50–55, 2005.

[113] R. Lipowsky, "Critical Surface Phenomena at First-Order Bulk Transitions," *Physcial Rev. Lett.*, vol. 49, no. 21, pp. 1575–1578, 1982.

[114] B. F. Henson, L. F. Voss, K. R. Wilson, and J. M. Robinson, "Thermodynamic model of quasiliquid formation on H_2O ice : Comparison with experiment," *J. Chem. Phys.*, vol. 123, no. 14, p. 144707, 2005.

[115] C. Bishop, D. Pan, L. Liu, G. Tribello, A. Michaelides, E. Wang, and B. Slater, "On thin ice: surface order and disorder during pre-melting," *Faraday Discuss.*, vol. 141, no. 0, pp. 277–292, 2009.

[116] M. Conde, C. Vega, and A. Patrykiejew, "The thickness of a liquid layer on the free surface of ice as obtained from computer simulation," *J. Chem. Phys.*, vol. 129, no. 1, p. 014702, 2008.

[117] H. Asakawa, G. Sazaki, K. Nagashima, S. Nakatsubo, and Y. Furukawa, "Prism and Other High-Index Faces of Ice Crystals Exhibit Two Types of Quasi-Liquid Layers," *Cryst. Growth Des.*, vol. 15, no. 7, pp. 3339–3344, 2015.

[118] H. Bluhm, T. Inoue, and M. Salmeron, "Friction of ice measured using lateral force microscopy," *Phys. Rev. B*, vol. 61, no. 11, pp. 7760–7765, 2000.

[119] H.-J. Butt, A. Döppenschmidt, G. Hüttl, E. Müller, and O. I. Vinogradova, "Analysis of plastic deformation in atomic force microscopy : Application to ice," *J. Chem. Phys.*, vol. 113, no. 3, pp. 1194–1203, 2000.

[120] A. Döppenschmidt and H.-J. Butt, "Measuring the Thickness of the Liquid-like Layer on Ice Surfaces with Atomic Force Microscopy," *Langmuir*, vol. 16, no. 16, pp. 6709–6714, 2000.

[121] H. Dosch, A. Lied, and J. Bilgram, "Glancing-angle X-ray scattering studies of the premelting of ice surfaces," *Surf. Sci.*, vol. 327, no. 1-2, pp. 145–164, 1995.

[122] Y. Furukawa, M. Yamamoto, and T. Kuroda, "Ellipsometric study of the transition layer on the surface of an ice crystal," *J. Cryst. Growth*, vol. 82, no. 4, pp. 665–677, 1987.

[123] M. P. Goertz, X.-Y. Zhu, and J. E. Houston, "Exploring the liquid-like layer on the ice surface," *Langmuir*, vol. 25, pp. 6905–6908, jun 2009.

[124] A. Lied, H. Dosch, and J. Bilgram, "Surface melting of ice Ih single crystals revealed by glancing angle x-ray scattering," *Phys. Rev. Lett.*, vol. 72, no. 22, pp. 3554–3557, 1994.

[125] G. Sazaki, S. Zepeda, S. Nakatsubo, M. Yokomine, and Y. Furukawa, "Quasi-liquid layers on ice crystal surfaces are made up of two different phases," *Proc. Natl. Acad. Sci.*, vol. 109, no. 4, pp. 1052–1055, 2012.

[126] Y. Li and G. A. Somorjai, "Surface Premelting of Ice," *J. Phys. Chem. C*, vol. 111, no. 27, pp. 9631–9637, 2007.

[127] X. Wei, P. B. Miranda, C. Zhang, and Y. R. Shen, "Sum-frequency spectroscopic studies of ice interfaces," *Phys. Rev. B*, vol. 66, no. 8, p. 085401, 2002.

[128] X. Wei, P. B. Miranda, and Y. R. Shen, "Surface Vibrational Spectroscopic Study of Surface Melting of Ice," *Phys. Rev. Lett.*, vol. 86, no. 8, pp. 1554–1557, 2001.

[129] P. J. Bisson and M. J. Shultz, "Hydrogen Bonding in the Prism Face of Ice Ih," *J. Phys. Chem. A*, vol. 117, pp. 6116–6125, 2013.

[130] H. Groenzin, I. Li, and M. J. Shultz, "Sum-frequency generation : Polarization surface spectroscopy analysis of the vibrational surface modes on the basal face of ice Ih," *J. Chem. Phys.*, vol. 128, no. 21, p. 214510, 2008.

[131] R. Rossend, K. B. Møller, and J. T. Hynes, "Hydrogen Bond Dynamics in Water and Ultrafast Infrared Spectroscopy," *J. Phys. Chem. A*, vol. 106, no. 50, pp. 11993–1196, 2002.

[132] C. P. Lawrence and J. L. Skinner, "Vibrational spectroscopy of HOD in liquid D_2O . III . Spectral diffusion , and hydrogen- bonding and rotational dynamics," *J. Chem. Phys.*, vol. 118, no. 264, pp. 264–272, 2003.

[133] E. R. Batista, S. S. Xantheas, and H. Jónsson, "Molecular multipole moments of water molecules in ice Ih," *J. Chem. Phys.*, vol. 109, no. 11, pp. 4546–4551, 1998.

[134] M. J. Shultz, P. Bisson, H. Groenzin, and I. Li, "Multiplexed polarization spectroscopy : Measuring surface hyperpolarizability orientation," *J. Chem. Phys.*, vol. 133, no. 5, p. 54702, 2010.

[135] T. Ishiyama, H. Takahashi, and A. Morita, "Origin of Vibrational Spectroscopic Response at Ice Surface," *J. Phys. Chem. Lett.*, vol. 3, pp. 3001–3006, oct 2012.

[136] T. Ishiyama and A. Morita, "A direct evidence of vibrationally delocalized response at ice surface," *J. Chem. Phys.*, vol. 503, p. 18C503, 2014.

[137] I. V. Stiopkin, C. Weeraman, P. A. Pieniazek, F. Y. Shalhout, J. L. Skinner, and A. V. Benderskii, "Hydrogen bonding at the water surface revealed by isotopic dilution spectroscopy," *Nature*, vol. 474, no. 7350, pp. 192–195, 2011.

[138] Y. Nagata, T. Hasegawa, E. H. G. Backus, K. Usui, S. Yoshimune, T. Ohto, and M. Bonn, "The surface roughness, but not the water molecular orientation varies with temperature at the water–air interface," *Phys. Chem. Chem. Phys.*, vol. 17, no. 17, pp. 23559–23564, 2015.

[139] J. F. van der Veen, "Melting and freezing at surfaces," *Surf. Sci.*, vol. 433-435, pp. 1–11, 1999.

[140] Q. S. Mei and K. Lu, "Melting and superheating of crystalline solids: From bulk to nanocrystals," *Prog. Mater. Sci.*, vol. 52, no. 8, pp. 1175–1262, 2007.

[141] A. W. D. van der Gon, J. M. Gay, J. W. M. Frenken, and J. F. van der Veen, "Order-disorder transitions at the Ge (111) surface," *Surf. Sci.*, vol. 241, no. 3, pp. 335–345, 1991.

[142] X. Wei and Y. R. Shen, "Motional effect in surface sum-frequency vibrational spectroscopy," *Phys. Rev. Lett.*, vol. 86, no. 21, pp. 4799–4802, 2001.

[143] J. P. D. Abbatt, "Interactions of Atmospheric Trace Gases with Ice Surfaces : Adsorption and Reaction," *Chem. Rev.*, vol. 103, pp. 4783–4800, 2003.

[144] T. Bartels-Rausch, H. W. Jacobi, T. F. Kahan, J. L. Thomas, E. S. Thomson, J. P. D. Abbatt, M. Ammann, J. R. Blackford, H. Bluhm, and C. Boxe, "A review of air – ice chemical and physical interactions (AICI): liquids , quasi-liquids , and solids in snow," *Atmos. Chem.Phys*, vol. 14, pp. 1587–1633, 2014.

[145] T. D. Shepherd, M. A. Koc, and V. Molinero, "The Quasi-Liquid Layer of Ice under Conditions of Methane Clathrate Formation," *J. Phys. Chem. C*, vol. 116, no. 22, pp. 12172–12180, 2012.

[146] J. L. F. Abascal, E. Sanz, R. García Fernández, and C. Vega, "A potential model for the study of ices and amorphous water: TIP4P/Ice," *J. Chem. Phys.*, vol. 122, no. 23, p. 234511, 2005.

[147] T. Ishiyama and A. Morita, "Analysis of anisotropic local field in sum frequency generation," *J. Chem. Phys.*, vol. 131, no. 24, p. 244714, 2009.

[148] M. Polcik, L. Wilde, and J. Hasse, "Partial Order of the Quasiliquid During Surface Melting of Al (110)," *Phys. Rev. Lett.*, vol. 78, p. 491, 1997.

[149] J. F. van der Veen, B. Pluis, and A. W. D. van der Gon, "Ion Scattering Studies of Surface Melting," in *Kinet. Ordering Growth surfaces* (M. G. Lagally, ed.), pp. 343–354, Springer Link, 1900.

[150] M. Ross, "Generalized Lindemann Melting Law," *Phys. Rev*, vol. 184, p. 233, 1969.

[151] P. N. Pusey, "Freezing and melting: Action at Grain Bounderies," *Science*, vol. 309, pp. 1198–1199, 2005.

[152] A. Alsayed, M. Islam, J. Zhang, P. Collings, and A. Yodh, "Premelting at Defects Within Bulk Colloidal Crystals," *Science*, vol. 309, pp. 1207–1210, 2005.

[153] S. C. Engemann, *Premelting at the ice – SiO_2 interface A high-energy x-ray microbeam diffraction study.* PhD thesis, University of Stuttgart, 2005.

[154] A. Trayanov and E. Tosatti, "Lattice theory of crystal surface melting," *Phys. Rev. Lett.*, vol. 59, no. 19, pp. 2207–2210, 1987.

[155] L. Pietronero and E. Tosatti, "Surface Theory of Melting," *Solid State Commun.*, vol. 32, no. 4, pp. 255–259, 1979.

[156] A. A. Chernov and L. V. Mikheev, "Wetting and surface melting:capillary fluctuations vs layerwise short-range order," *Phys. A Stat. Mech. its Appl.*, vol. 157, no. 2, pp. 1042–1058, 1989.

[157] A. Tokmakoff, "Structural Rearrangements in Water Viewed Spectroscopy," *Acc. Chem. Res.*, vol. 42, no. 9, pp. 1239–1249, 2009.

[158] H. K. Nienhuys, S. Woutersen, R. a. van Santen, and H. J. Bakker, "Mechanism for vibrational relaxation in water investigated by femtosecond infrared spectroscopy," *J. Chem. Phys.*, vol. 111, no. 4, pp. 1494–1500, 1999.

[159] A. J. Lock and H. J. Bakker, "Temperature dependence of vibrational relaxation in liquid H2O," *J. Chem. Phys.*, vol. 117, no. 4, pp. 1708–1713, 2002.

[160] S. Woutersen, U. Emmerichs, H.-K. Nienhuys, and H. J. Bakker, "Anomalous Temperature Dependence of Vibrational Lifetimes in Water and Ice," *Phys. Rev. Lett.*, vol. 81, no. 5, pp. 1106–1109, 1998.

[161] K. J. Tielrooij, C. Petersen, Y. L. A. Rezus, and H. J. Bakker, "Reorientation of HDO in liquid H_2O at different temperatures: Comparison of first and second order correlation functions," *Chem. Phys. Lett.*, vol. 471, pp. 71–74, 2009.

[162] Z. Zhang, L. Piatkowski, H. J. Bakker, and M. Bonn, "Ultrafast vibrational energy transfer at the water/air interface revealed by two-dimensional surface vibrational spectroscopy," *Nat. Chem.*, vol. 3, no. 11, pp. 888–893, 2011.

[163] C.-S. Hsieh, R. K. Campen, A. C. Vila Verde, P. Bolhuis, H.-K. Nienhuys, and M. Bonn, "Ultrafast Reorientation of Dangling OH Groups at the Air-Water Interface Using Femtosecond Vibrational Spectroscopy," *Phys. Rev. Lett.*, vol. 107, p. 116102, 2011.

[164] C.-S. Hsieh, R. K. Campen, M. Okuno, E. H. G. Backus, Y. Nagata, and M. Bonn, "Mechanism of vibrational energy dissipation of free OH groups at the air-water interface.," *Proc. Natl. Acad. Sci. U. S. A.*, vol. 110, no. 47, pp. 18780–5, 2013.

[165] C.-S. Hsieh, M. Okuno, J. Hunger, E. H. G. Backus, Y. Nagata, and M. Bonn, "Aqueous heterogeneity at the air/water interface revealed by 2D-HD-SFG spectroscopy," *Angew. Chemie - Int. Ed.*, vol. 53, no. 31, pp. 8146–8149, 2014.

[166] M. Bonn, Y. Nagata, and E. H. G. Backus, "Molecular structure and dynamics of water at the water-air interface studied with surface-specific vibrational spectroscopy," *Angew. Chemie - Int. Ed.*, vol. 54, no. 19, pp. 5560–5576, 2015.

[167] S. T. van der Post, C.-S. Hsieh, M. Okuno, Y. Nagata, H. J. Bakker, M. Bonn, and J. Hunger, "Strong frequency dependence of vibrational relaxation in bulk and surface water reveals sub-picosecond structural heterogeneity.," *Nat. Commun.*, vol. 6, p. 8384, 2015.

[168] Liang Shi, J. L. Skinner, and T. L. C. Jansen, "Two-dimensional infrared spectroscopy of neat ice Ih," *Phys. Chem. Chem. Phys.*, vol. 18, pp. 3772–3779, 2016.

[169] H. Jacobi, T. F. Kahan, J. L. Thomas, E. S. Thomson, J. P. D. Abbatt, and M. Ammann, "A review of air – ice chemical and physical interactions (AICI): liquids , quasi-liquids , and solids in snow," *Atoms.Chem.Phys*, vol. 14, pp. 1587–1633, 2014.

[170] A. A. Stathis, A. K. Hendrickson-Stives, and T. F. Kahan, "Photolysis Kinetics of Toluene, Ethylbenzene, and Xylenes at Ice Surfaces," *J. Phys. Chem. A*, vol. 120, pp. 6693–6697, 2016.

[171] G. Seifert, K. Weidlich, and H. Graener, "Picosecond ir hole-burning spectroscopy on HDO ice Ih," *Phys. Rev. B*, vol. 56, no. 22, pp. R14231–R14234, 1997.

[172] A. M. Dokter, C. Petersen, S. Woutersen, and H. J. Bakker, "Vibrational dynamics of ice in reverse micelles," *J. Chem. Phys.*, vol. 128, no. 4, p. 044509, 2008.

[173] A. M. Dokter and H. J. Bakker, "Transient absorption of vibrationally excited ice Ih," *J. Chem. Phys.*, vol. 128, no. 2, p. 024502, 2008.

[174] R. L. A. Timmer and H. J. Bakker, "Vibrational Foerster Transfer in Ice Ih," *J. Phys. Chem. A*, vol. 114, pp. 4148–4155, 2010.

[175] W. J. Smit and H. J. Bakker, "Anomalous temperature dependence of the vibrational lifetime of the OD stretch vibration in ice and liquid water," *J. Chem. Phys.*, vol. 139, no. 20, p. 204504, 2013.

[176] F. Perakis, S. Widmer, and P. Hamm, "Two-dimensional infrared spectroscopy of isotope-diluted ice Ih," *J. Chem. Phys.*, vol. 134, no. 20, 2011.

[177] F. Perakis and P. Hamm, "Two-dimensional infrared spectroscopy of neat ice Ih," *Physic Chem Chem Phys*, vol. 14, pp. 6250–6256, 2012.

[178] F. Perakis, J. A. Borek, and P. Hamm, "Three-dimensional infrared spectroscopy of isotope-diluted ice Ih," *J. Chem. Phys.*, vol. 139, no. 1, 2013.

[179] S. Ashihara, N. Huse, A. Espagne, E. T. J. Nibbering, and T. Elsaesser, "Vibrational couplings and ultrafast relaxation of the O-H bending mode in liquid H_2O," *Chem. Phys. Lett.*, vol. 424, no. 1-3, pp. 66–70, 2006.

[180] T. Yagasaki and S. Saito, "Fluctuations and relaxation dynamics of liquid water revealed by linear and nonlinear spectroscopy.," *Annu. Rev. Phys. Chem.*, vol. 64, pp. 55–75, 2013.

[181] H. Liu, Y. Wang, and J. M. Bowman, "Quantum calculations of intramolecular IR spectra of ice models using ab initio potential and dipole moment surfaces," *J. Phys. Chem. Lett.*, vol. 3, no. 24, pp. 3671–3676, 2012.

[182] H. Fukazawa and S. Mae, "The vibrational spectra of ice Ih and polar ice," in *Phys. Ice Core Rec.*, pp. 25–42, 2000.

[183] M. A. Donovan, Y. Y. Yimer, J. Pfaendtner, E. H. G. Backus, and M. Bonn, "Ultrafast reorientational dynamics of leucine at the air- water interface," *J. Am. Chem. Soc.*, vol. 138, no. 16, pp. 5226–5229, 2016.

[184] M. Bonn, H. J. Bakker, A. Ghosh, S. Yamamoto, M. Sovago, and R. K. Campen, "Structural inhomogeneity of interfacial water at lipid monolayers revealed by surface-specific vibrational pump-probe spectroscopy," *J. Am. Chem. Soc.*, vol. 132, no. 42, pp. 14971–14978, 2010.

[185] Y. L. A. Rezus and H. J. Bakker, "On the orientational relaxation of HDO in liquid water," *J. Chem. Phys.*, vol. 123, p. 114502, 2005.

[186] R. A. Livingstone, Y. Nagata, M. Bonn, and E. H. G. Backus, "Two Types of Water at the Water-Surfactant Interface Revealed by Time-Resolved Vibrational Spectroscopy," *J. Am. Chem. Soc.*, vol. 137, no. 47, pp. 14912–14919, 2015.

[187] H. J. Bakker and J. L. Skinner, "Vibrational Spectroscopy as a Probe of Structure and Dynamics in Liquid Water," *Chem. Rev.*, vol. 110, pp. 1498–1517, 2010.

[188] K. J. Tielrooij, R. L. A. Timmer, H. J. Bakker, and M. Bonn, "Structure dynamics of the proton in liquid water probed with terahertz time-domain spectroscopy," *Phys. Rev. Lett.*, vol. 102, no. 19, pp. 1–4, 2009.

[189] J.-W. Shin, N. I. Hammer, E. G. Diken, M. A. Johnson, R. S. Walters, T. D. Jaeger, M. A. Duncan, A. Christie, and K. D. Jordan, "Infrared Signature of Structures Associated with the $H^2(H_2O)_n$ (n=6 to 27) Clusters," *Science*, vol. 304, no. April, pp. 1137–1141, 2004.

[190] H. J. Bakker and M. Bonn, "Femtosecond Vibrational Spectroscopy of Aqueous Systems," in *Ultrafast Infrared Vib. Spectrosc.* (M. D. Fayer, ed.), pp. 100–141, Florida: CRC Press, 2013.

[191] N. Agmon, H. J. Bakker, R. K. Campen, R. H. Henchman, P. Pohl, S. Roke, M. Thaemer, and A. Hassanali, "Protons and Hydroxide Ions in Aqueous Systems," *Chem. Rev.*, vol. 116, no. 13, pp. 7642–7672, 2016.

[192] N. Bjerrum, "Structure and Properties of Ice," *Science*, vol. 115, pp. 385–390, 1952.

[193] M. Eigen, "Proton Transfer, Acid-Base Catalysis, and Enzymatic Hydrolysis," *Angew. Chem. Int. Ed.*, vol. 3, no. 1, pp. 1–72, 1964.

[194] C. Kobayashi, S. Saito, and I. Ohmine, "Mechanism of fast proton transfer in ice: Potential energy surface and reaction coordinate analyses," *J. Chem. Phys.*, vol. 113, no. 20, pp. 9090–9100, 2000.

[195] M. J. Molina, "Polar Ozone Depletion (Nobel Lecture)," *Angew. Chemie Int. Ed. English*, vol. 35, no. 16, pp. 1778–1785, 1996.

[196] C. J. Mundy and I. F. W. Kuo, "First-principles approaches to the structure and reactivity of atmospherically relevant aqueous interfaces," *Chem. Rev.*, vol. 106, no. 4, pp. 1282–1304, 2006.

[197] S. Kawada, "Dielectric Anisotropy in Ice Ih," *J. Phys. Soc. Japan*, vol. 44, no. 6, pp. 1881–1886, 1978.

[198] G. W. Gross, I. C. Hayslip, and R. N. Hoy, "Electical conductivity and relaxation in ice crystals with known impurity content," *J. Glaciol.*, vol. 2, no. 85, pp. 143–160, 1978.

[199] J. Devlin, "An alternate interpretation of the conductivity of HCl-doped ice," *J. Chem. Phys.*, vol. 89, no. 9, pp. 5967–5968, 1988.

[200] I. Takei and N. Maeno, "Dielectric Low-Frequency Dispersion and Crossover Phenomena of HCl-Doped Ice," *Measurement*, vol. 5647, no. 96, pp. 6234–6236, 1997.

[201] I. Takei and N. Maneo, "Electric Characteristics of point Defects in HCl-Doped Ice," *J. Phys.*, vol. 48, pp. 121–126, 1987.

[202] I. Takei and N. Maeno, "Dielectric properties of single crystals of HCl-doped ice," *J. Chem. Phys.*, vol. 81, no. 12, pp. 6186–6190, 1984.

[203] I. Presiado, J. Lal, E. Mamontov, A. I. Kolesnikov, and D. Huppert, "Fast proton hopping detection in ice Ih by quasi-elastic neutron scattering," *J. Phys. Chem. C*, vol. 115, no. 20, pp. 10245–10251, 2011.

[204] A. Uritski, I. Presiado, Y. Erez, R. Gepshtein, and D. Huppert, "Temperature dependence of proton diffusion in Ih ice," *J. Phys. Chem. C*, vol. 113, no. 23, pp. 10285–10296, 2009.

[205] A. Uritski, I. Presiado, and D. Huppert, "Indication of a very large proton diffusion in ice ih. III. Fluorescence quenching of 1-naphthol derivatives," *J. Phys. Chem. A*, vol. 113, no. 6, pp. 959–974, 2009.

[206] B. Geil, T. M. Kirschgen, and F. Fujara, "Mechanism of proton transport in hexagonal ice," *Phys. Rev. B*, vol. 72, no. 1, pp. 1–10, 2005.

[207] R. L. A. Timmer, M. J. Cox, and H. J. Bakker, "Direct observation of proton transfer in ice Ih using femtosecond spectroscopy," *J. Phys. Chem. A*, vol. 114, pp. 2091–2101, 2010.

[208] C. Girardet and C. Toubin, "Molecular atmospheric pollutant adsorption on ice: A theoretical survey," *Surf. Sci. Rep.*, vol. 44, no. 7-8, pp. 159–238, 2001.

[209] R. Bianco, B. J. Gertner, and J. T. Hynes, "Proton Transfer Reactions at the Surface of ice. Heterogeneous Reactions Involved in Stratospheric Ozone Depletion," *Berichte der Bunsengesellschaft für Phys. Chemie*, vol. 102, no. 3, pp. 518–526, 1998.

[210] K. Bolton and J. B. C. Pettersson, "Ice-catalyzed ionization of hydrochloric acid," *J. Am. Chem. Soc.*, vol. 123, no. 30, pp. 7360–7363, 2001.

[211] P. Parent and C. Laffon, "Adsorption of HCl on the water ice surface studied by X-ray absorption spectroscopy," *J Phys Chem B*, vol. 109, no. 4, pp. 1547–1553, 2005.

[212] K. Park, W. Lin, and F. Paesani, "Fast and slow proton transfer in ice: The role of the Quasi-liquid layer and hydrogen-bond network," *J. Phys. Chem. B*, vol. 118, no. 28, pp. 8081–8089, 2014.

[213] S. Riikonen, P. Parkkinen, L. Halonen, and R. B. Gerber, "Ionization of acids on the quasi-liquid layer of ice," *J. Phys. Chem. A*, vol. 118, no. 27, pp. 5029–5037, 2014.

[214] L. E. Bove, S. Klotz, A. Paciaroni, and F. Sacchetti, "Anomalous proton dynamics in ice at low temperatures," *Phys. Rev. Lett.*, vol. 103, no. 16, pp. 1–4, 2009.

[215] E. S. Moon, Y. Kim, S. Shin, and H. Kang, "Asymmetric transport efficiencies of positive and negative ion defects in amorphous ice," *Phys. Rev. Lett.*, vol. 108, no. 22, pp. 1–5, 2012.

[216] J. P. Devlin, "Relating the current science of ion-defect behavior in ice to a plausible mechanism for directional charge transfer during ice particle collisions.," *Phys. Chem. Chem. Phys.*, vol. 13, no. 44, pp. 19707–13, 2011.

[217] H. Kang, "Chemistry of ice surfaces. Elementary reaction steps on ice studied by reactive ion scattering," *Acc. Chem. Res.*, vol. 38, no. 12, pp. 893–900, 2005.

[218] S. Zimmermann, M. Kippenberger, G. Schuster, and J. N. Crowley, "Adsorption isotherms for hydrogen chloride (HCl) on ice surfaces between 190 and 220 K," *Phys. Chem. Chem. Phys.*, vol. 18, no. 20, pp. 13799–13810, 2016.

[219] D. H. Lee, J. Bang, and H. Kang, "Surface Charge Layer of Amorphous Solid Water with Adsorbed Acid or Base: Asymmetric Depth Distributions of H^+ and OH^- Ions," *J. Phys. Chem. C*, vol. 120, no. 22, pp. 12051–12058, 2016.

[220] S. N. Wren and D. J. Donaldson, "Laboratory Study of pH at the Air Ice Interface," *J. Phys. Chem. C*, vol. 116, pp. 10171–10180, 2012.

[221] K. Sasaki, R. Kita, N. Shinyashiki, and S. Yagihara, "Dielectric Relaxation Time of Ice-Ih with Different Preparation," *J. Phys. Chem. B*, vol. 120, no. 16, pp. 3950–3953, 2016.

[222] L. M. Levering, M. R. Sierra-Hernandez, and H. C. Allen, "Observation of hydronium ions at the air - Aqueous acid interface: Vibrational spectroscopic studies of aqueous HCI, HBr, and HI," *J. Phys. Chem. C*, vol. 111, no. 25, pp. 8814–8826, 2007.

[223] N. Agmon, "Infrared spectroscopy: The acid test for water structure," *Nat. Chem.*, vol. 8, no. 3, pp. 206–207, 2016.

[224] K. J. Tielrooij, *Molecular Motions of Water The effect of charged and hydrophobic solutes.* PhD thesis, Universiteit van Amsterdam, 2010.

[225] C. Zhang, K. S. Lee, X. C. Zhang, X. Wei, and Y. R. Shen, "Optical constants of ice Ih crystal at terahertz frequencies," *Appl. Phys. Lett.*, vol. 79, no. 4, pp. 491–493, 2001.

[226] K. Takeya, T. Fukui, R. Takahashi, and K. Kawase, "Dielectric constants of H_2O and D_2O ice in the terahertz frequency regime over a wide temperature range," *J. Opt.*, vol. 16, no. 9, p. 094005, 2014.

[227] C. Tian, N. Ji, G. A. Waychunas, and Y. R. Shen, "Interfacial structures of acidic and basic aqueous solutions," *J. Am. Chem. Soc.*, vol. 130, no. 39, pp. 13033–13039, 2008.

Acknowledgements

This section is not included in this version.

List of publications

Publications covered in this thesis

- **Sánchez, M. A.**[1], Cyran, J. D [1]., van Zadel, M.-J., Smit, W, J., Bakker, H. J., Bonn, M., and Backus, E.H.G "Ice surface has sub-picosecond structural heterogeneity", in preparation -*Chapter 6*

- **Sánchez, M. A.**, Liu, W., Fischer, S., Bücher, K., Müllen, K., Weil, T., Bonn, M., Hammer, B.A.G., Wu, Y., and Backus, E.H.G "Hydrophobic interactions influence uptake efficiency of cell penetrating dendrimers", in preparation -*Chapter 3*

- **Sánchez, M. A.**, Kling, T., Ishiyama, T., van Zadel, M.-J., Bisson, P. J., Mezger, M., Jochum, M. N., Cyran, J. D., Smit, W, J., Bakker, H. J., Shultz, M. J., Morita, A., Donadio, D., Nagata, Y., Bonn, M., and Backus, E. H. G. "Experimental and theoretical evidence for bilayer-by-bilayer surface melting of crystalline ice". *PNAS*, 114, 227-232, 2017. -*Chapter 4 and 5*

- Varol, H. S., **Sánchez, M. A.**, Lu, H., Baio, J. E., Malm, C., Encinas, N., Mermet-Guyennet, M. R. B., Martzel, N., Bonn, D., Bonn, M., Weidner, T., Backus, E. H. G., Parekh, S. H. "Multiscale Effects of Interfacial Polymer Confinement in Silica Nanocomposites". *Macromolecules*, 48, 7929-7937, 2015. -*Chapter 2*

Other publications by the same author

- Abdelmonem, A., Backus, E. H. G., Hoffmann, N., **Sánchez, M. A.**, Cyran, J. D., Kiselev, A., Bonn, M. "Surface charge-induced orientation of interfacial water suppresses heterogeneous ice nucleation on α -alumina (0001)", *Atmos. Chem. Phys. Discuss.*, 2017.

- Bellido, E., González-Monje, P., Guardingo, M., Novio, F., **Sánchez, M. A.**, Montero, M. L., Molnar, G., Bousseksou, A and Ruiz-Molina, D. "Nanoscale coordination polymers obtained in ultrasmall liquid droplets on solid surfaces and its comparison to different synthetic volume scales". *RSC Adv.*, 6, 76666-76672, 2016.

- **Sánchez, M. A.**, Paniagua, S. A., Borge, I., Viales, C., Montero, M.L. "Lewis basicity, adhesion thermodynamic work and coordinating ability on aminated silicon surfaces" . *Appl. Surf. Sci.*, 317, 1060-1067, 2014.

- **Sánchez, A.**, Urcuyo, R., González-Flores, D., Montalberth-Smith, R., León-Rojas, C., Pineda, L. W., Montero, M.L. " Electroactive copper(II) bimetallic self-assembled multilayers on Si(100)". *Surf. Sci.*, 606, 527-535, 2012.

[1]Both authors contributed equally to this work.

- **Sánchez, A.**, González, J., García-Piñeres, A., Montero, M. L. "Nano-hydroxyapatite colloid suspension coated on chemically modified porous silicon by cathodic bias: a suitable surface for cell culture". *Phys. Status Solidi*, 8, 1898-1902, 2011.

Conference Contributions

- **Sánchez, M. A.**, Kling, T., Ishiyama, T., van Zadel, M.-J., Bisson, P. J., Mezger, M., Jochum, M. N., Cyran, J. D., Smit, W, J., Bakker, H. J., Shultz, M. J., Morita, A., Donadio, D., Nagata, Y., Bonn, M., and Backus, E. H. G. "A spectroscopic investigation of surface melting of ice" Vibrational Spectroscopy Gordon Research Conference, U.S.A, 2016.
- **Sánchez, M. A.**, Bonn, M., and Backus, E. H. G. "A spectroscopic investigation of surface melting of ice" DPG Spring Meeting, Regensburg, Germany, 2016.
- **Sánchez, M. A.**, Bücher, K., Müllen, K ., Bonn, M., and Backus, E. H. G. "The interaction of patterned amphiphilic dendritic nanomaterial with a lipid-monolayer" DPG Spring Meeting, Berlin, Germany, 2015.
- **Sánchez, M. A.**, van Zadel, M.-J., Bisson, P. J., Shultz, M. J., Bonn, M., and Backus, E. H. G. "Surface melting of ice" Vibrational Spectroscopy Gordon Research Conference, U.S.A, 2014.
- **Sánchez, M. A.**, van Zadel, M.-J., Bisson, P. J., Shultz, M. J., Bonn, M., and Backus, E. H. G. "Nature of the liquid layer in surface melting" DPG Spring Meeting, Dresden, Germany, 2014.